

POLITECNICO
MILANO 1863

Department of Electronics, Information and Bioengineering
Doctoral Programme In Information Technology

Robust and Automatically-Driven Optical Networks

Doctoral Dissertation of:
Xin Yang

Student ID: 10916653
Advisor: Prof. Massimo Tornatore
Tutor: Prof. Parolari Paola
Year 2025/2026 - XXXVIII Cycle

Abstract

Optical networks form the backbone of today's digital infrastructure, transporting the majority of global data traffic across long-haul, metro, and data center domains. As they evolve to accommodate exponential traffic growth and support latency-critical services such as 5G, 6G, and distributed AI, future optical networks face unprecedented demands for capacity, resilience, and automation. At the same time, physical impairments—including amplifier noise, Kerr nonlinearities, stimulated Raman scattering (SRS), filtering penalties, and transponder back-to-back limitations—accumulate along transmission paths and constrain the signal reach through its Quality of Transmission (QoT). While analytical models can capture these effects, their predictive accuracy in live networks is hindered by uncertain parameters and limited observability, forcing operators to adopt conservative margins that reduce the utilization efficiency of network resources such as capacity and power.

This thesis aims to advance the design of *Robust and Automatically-Driven Optical Networks*, and the main contributions can be summarized in three parts as follows.

1. **Experimental Quantification and Mitigation of QoT Degradation through Power Re-optimization:** A key challenge in optical networks is that the practical "set-and-forget" power setting strategy, widely adopted in today's operations, ignores cumulative load-dependent effects arising from incremental traffic loading and the absence of power re-optimization for already established channels. As a consequence, the QoT of existing services progressively degrades as additional services are loaded into the network. To address this, I experimentally quantify such QoT degradation in multi-node mesh testbeds and show its impact on network performance. I further propose both static and dynamic power re-optimization strategies integrated into a software-defined networking (SDN) control plane called "AI-Light". Experimental demonstrations confirm that these strategies can substantially recover SNR degradation and pave the way for automated and resilient network operation.

2. **Development of Input Refinement (IR) Techniques for Digital Twins:** The accuracy of analytical QoT models depends critically on physical parameters

such as insertion losses, amplifier gains, and fiber characteristics. However, these parameters are often uncertain or hidden from operators in live networks. To overcome this limitation, I design and validate four complementary Input Refinement (IR) techniques that leverage in-service monitoring data to calibrate digital twins. Specifically: (i) Passive IR (PIR) achieves OMS-level accuracy from a single snapshot and extends to C+L systems; (ii) Active IR (AIR) perturbs amplifier gains to exploit SRS signatures, enabling span-level anomaly detection and localization; (iii) Incremental IR (IIR) leverages multiple snapshots for progressive refinement and supports closed-loop autonomous optimization; and (iv) a Hybrid IR+PPE method integrates power profile estimation with IR, achieving absolute calibration of insertion losses and longitudinal power evolution. Together, these methods establish accurate, robust, and operationally viable digital twins for QoT prediction and optimization.

3. **Benchmarking of Transponders for Data Center Interconnect (DCI):** Beyond backbone and metro networks, the rapid expansion of cloud and AI workloads has made data center interconnects (DCIs) a critical domain for optical networking. Hyperscale operators must balance cost, reach, and capacity when choosing among different coherent transponder families. To provide design guidelines, I conduct a systematic benchmarking of 800G ZR, ZR+, and high-performance transponders using simulations that incorporate experimentally measured amplifier dynamics in short-reach DCI networks. The study analyzes capacity scaling under varying span losses, multiplexing schemes, and spectrum expansion scenarios, identifying the trade-offs among different solutions. The results highlight effective design and loading strategies for cost-efficient and high-capacity DCI deployments.

In summary, this thesis demonstrates that integrating analytical QoT models with refined monitoring, SDN control, and digital twins enables scalable automation, margin-efficient operation, and actionable design guidelines for next-generation optical networks.

Keywords: Optical networks; Physical impairments; Quality of transmission; Digital twin; Input refinement; Power optimization; SDN automation; Data center interconnect.

Abstract

Le reti ottiche costituiscono la spina dorsale dell'infrastruttura digitale odierna, trasportando la maggior parte del traffico dati globale attraverso domini long-haul, metropolitani e dei data center. Con la loro evoluzione per accogliere una crescita esponenziale del traffico e supportare servizi a bassa latenza come il 5G, il 6G e l'intelligenza artificiale distribuita, le future reti ottiche affrontano richieste senza precedenti in termini di capacità, resilienza e automazione. Allo stesso tempo, gli effetti fisici degradanti — tra cui il rumore degli amplificatori, le non linearità di Kerr, la diffusione Raman stimolata (SRS), le penalità di filtraggio e le limitazioni back-to-back dei transponder — si accumulano lungo i percorsi di trasmissione e limitano la portata del segnale attraverso la sua Qualità di Trasmissione (QoT). Sebbene i modelli analitici possano descrivere tali effetti, la loro accuratezza predittiva nelle reti operative è ostacolata da parametri incerti e limitata osservabilità, costringendo gli operatori ad adottare margini conservativi che riducono l'efficienza di utilizzo delle risorse di rete, come capacità e potenza.

Questa tesi mira ad avanzare la progettazione di *reti ottiche robuste e a guida automatica*, e i principali contributi possono essere riassunti in tre parti come segue.

1. **Quantificazione sperimentale e mitigazione del degrado di QoT tramite riottimizzazione della potenza:** Una sfida fondamentale nelle reti ottiche è che la pratica strategia di impostazione della potenza "set-and-forget", ampiamente adottata nelle operazioni odierne, ignora gli effetti cumulativi del caricamento incrementale del traffico. Di conseguenza, i nuovi canali provisionati possono degradare significativamente la QoT dei servizi già esistenti. Per affrontare questo problema, quantifico sperimentalmente tale degrado di QoT in banchi di prova (testbed) a maglia multi-nodo e mostro il suo impatto sulle prestazioni di rete. Propongo inoltre strategie di riottimizzazione della potenza, sia statiche sia dinamiche, integrate in un piano di controllo SDN (Software-Defined Networking) denominato "AI-Light". Le dimostrazioni sperimentali confermano che tali strategie possono recuperare sostanzialmente la degradazione di SNR e aprire la strada a un funzionamento di rete automatizzato e resiliente.

2. **Sviluppo di tecniche di Input Refinement (IR) per gemelli digitali:** L'accuratezza dei modelli analitici di QoT dipende in modo critico da parametri fisici come le perdite di inserzione, i guadagni degli amplificatori e le caratteristiche della fibra. Tuttavia, tali parametri sono spesso incerti o non accessibili agli operatori nelle reti operative. Per superare questa limitazione, progetto e valido quattro tecniche complementari di Input Refinement (IR) che sfruttano dati di monitoraggio in servizio per calibrare i gemelli digitali. In particolare: (i) il Passive IR (PIR) raggiunge un'accuratezza a livello di OMS a partire da un singolo snapshot e si estende ai sistemi C+L; (ii) l'Active IR (AIR) perturba i guadagni degli amplificatori per sfruttare le firme SRS, consentendo il rilevamento e la localizzazione di anomalie a livello di tratta; (iii) l'Incremental IR (IIR) utilizza snapshot multipli per un raffinamento progressivo e supporta l'ottimizzazione autonoma in ciclo chiuso; e (iv) un metodo ibrido IR+PPE integra la stima del profilo di potenza con IR, ottenendo una calibrazione assoluta delle perdite di inserzione e dell'evoluzione longitudinale della potenza. Insieme, questi metodi stabiliscono gemelli digitali accurati, robusti e operativamente validi per la previsione e l'ottimizzazione della QoT.
3. **Benchmarking dei transponder per l'interconnessione dei data center (DCI):** Oltre alle reti backbone e metropolitane, la rapida espansione dei carichi di lavoro legati al cloud e all'intelligenza artificiale ha reso le interconnessioni tra data center (DCI) un dominio cruciale per le reti ottiche. Gli operatori hyperscale devono bilanciare costo, portata e capacità nella scelta tra diverse famiglie di transponder coerenti. Per fornire linee guida di progettazione, conduco un benchmarking sistematico di transponder a 800G ZR, ZR+ e ad alte prestazioni utilizzando simulazioni che incorporano dinamiche di amplificatori misurate sperimentalmente in reti DCI a corta portata. Lo studio analizza la scalabilità della capacità in condizioni variabili di perdita di tratta, schemi di multiplazione e scenari di espansione dello spettro, identificando i compromessi tra le diverse soluzioni. I risultati evidenziano strategie efficaci di progettazione e caricamento per implementazioni DCI ad alta capacità ed economicamente efficienti.

In sintesi, questa tesi dimostra che l'integrazione di modelli analitici di QoT con monitoraggio raffinato, controllo SDN e gemelli digitali consente automazione su larga scala, funzionamento con margini efficienti e linee guida progettuali concrete per le reti ottiche di nuova generazione.

Parole chiave: Reti ottiche; Degradazioni fisiche; Qualità di trasmissione; Gemello digitale; Input refinement; Ottimizzazione della potenza; Automazione SDN; Interconnessione dei data center.

List of Publications

The following publications highlight **my primary research contributions.** They include two published first-authored journal articles and five published or accepted first-authored conference papers. In addition, one further first-authored journal article is currently under review.

P1 **Xin Yang**, Alessio Ferrari, Dylan Le Gac, Gabriel Charlet, Massimo Tornatore, Yvan Pointurier, *"Experimental impact of power re-optimization in a mesh network"*, IEEE/Optica Journal of Optical Communications and Networking, 2023. **[Q1]**

The material of this publication contributes to Chapter 2.

P2 **Xin Yang**, Alessio Ferrari, Nathalie Morette, Yvan Pointurier, *"QoT Estimation Improvement with Inputs Refinement Tool for C+L Networks"*, Optical Fiber Communication Conference (OFC), 2023.

The material of this publication contributes to Chapter 3.

P3 **Xin Yang**, Chenyu Sun, Gabriel Charlet, Massimo Tornatore, Yvan Pointurier, *"Digital Twin-based Insertion Loss Estimator for Anomalous Loss Localization and Network Equalization Enhancement"*, Optical Fiber Communication Conference (OFC), 2024.

The material of this publication contributes to Chapter 4.

P4 **Xin Yang**, Chenyu Sun, Gabriel Charlet, Massimo Tornatore, Yvan Pointurier, *"Digital-Twin-Based Active Inputs Refinement for Insertion Loss Estimation and QoT optimization in C and C+L Networks"*, IEEE/Optica Journal of Optical Communications and Networking, 2024. **[Q1]**

The material of this publication contributes to Chapter 4.

P5 **Xin Yang**, Chenyu Sun, Reda Ayassi, Gabriel Charlet, Massimo Tornatore, Yvan Pointurier, *"Inputs Refinement with Incremental Learning for Accurate Digital Twin of Optical Networks"*, Optical Fiber Communication Conference (OFC), 2025.

The material of this publication contributes to Chapter 5.

P6 **Xin Yang**, Chenyu Sun, Reda Ayassi, Louis Aknin, Gabriel Charlet, Massimo Tornatore, Yvan Pointurier, *"Input Refinement with Incremental Learning for Accurate Digital Twin-Enabled Self-Driven QoT Optimization in Optical Networks"*, IEEE/Optica Journal of Optical Communications and Networking. [Under Review, **Q1**]

The material of this publication contributes to Chapter 5.

P7 **Xin Yang**, Tarek Eldahrawy, Chenyu Sun, Abel Lorences-Riesgo, Massimo Tornatore, Gabriel Charlet(1), Yvan Pointurier, *"Integrating PPE and Inputs Refinement for Enhanced QoT Estimation and Optimization in an Optical Mesh Network"*, European Conference on Optical Communication (ECOC), 2024.

The material of this publication contributes to Chapter 6.

P8 **Xin Yang**, Abel Lorences-Riesgo, Salma Escobar-Landero, Massimo Tornatore, Gabriel Charlet, Yvan Pointurier, *"Capacity Scaling Limits of DCI Networks: A Comparative Study of ZR, ZR+, and High-Performance Transponders"*, European Conference on Optical Communication (ECOC), 2025. [**Accepted**]

The material of this publication contributes to Chapter 7.

The following publications represent additional contributions not included in this Doctoral Dissertation. They comprise three published co-authored journal papers and ten published co-authored conference papers.

P1 Chenyu Sun, **Xin Yang**, Nicola Di Cicco, Reda Ayassi, Venkata Virajit Garbhapu, Photios A. Stavrou, Massimo Tornatore, Gabriel Charlet, Yvan Pointurier, *"Experimental demonstration of local AI-Agents for lifecycle management and control automation of optical networks"*, IEEE/Optica Journal of Optical Communications and Networking, 2025. [**Q1**]

P2 Chenyu Sun, **Xin Yang**, Gabriel Charlet, Photios A. Stavrou, Yvan Pointurier, *"Digital twin-enabled multi-step strategies for autonomous power equalization in optical networks"*, IEEE/Optica Journal of Optical Communications and Networking, 2025. [**Q1**]

P3 Tarek Eldahrawy, Abel Lorences-Riesgo, **Xin Yang**, Flavio Sampaio, Hartmut Hafermann, Yann Frignac, Christophe Finot, Gabriel Charlet, *"SOA Nonlinearity Aware Longitudinal Power Profile Estimation"*, IEEE/Optica Journal of Lightwave Technology, 2025. [**Q1**]

P4 Chenyu Sun, **Xin Yang**, Gabriel Charlet, Photios A Stavrou, Yvan Pointurier, *"Digital Twin-Enabled Optical Network Channel Power Management by WSS and Booster Auto-Adjustment"*, Optical Fiber Communication Conference (OFC), 2025.

P5 Reda Ayassi, **Xin Yang**, Chenyu Sun, Yvan Pointurier, Gabriel Charlet, *"Filtering Impairments-Aware Digital Twin for SNR Prediction over Network Life-Cycle"*, Optical Fiber Communication Conference (OFC), 2025.

P6 Chenyu Sun, Reda Ayassi, **Xin Yang**, Gabriel Charlet, Photios A Stavrou, Yvan Pointurier, *"Demonstration of LLM-based AI-Agent for Optical Network Management and Automation"*, European Conference on Optical Communication (ECOC), 2024.

P7 Tarek Eldahrawy, Abel Lorences-Riesgo, **Xin Yang**, Flavio Sampaio, Hartmut Hafermann, Yann Frignac, Gabriel Charlet, *"Fiber Longitudinal Power Profile Estimation Accounting for SOA Nonlinearities"*, European Conference on Optical Communication (ECOC), 2024.

P8 Chenyu Sun, **Xin Yang**, Gabriel Charlet, Photios A Stavrou, Yvan Pointurier, *"Digital twin enabled automatic power adjustment with multi-step lookahead prediction"*, European Conference on Optical Communication (ECOC), 2024.

P9 Chenyu Sun, **Xin Yang**, Nicola Di Cicco, Reda Ayassi, V Virajit Garbhapu, Photios A Stavrou, Massimo Tornatore, Gabriel Charlet, Yvan Pointurier, *"First experimental demonstration of full lifecycle automation of optical network through fine-tuned LLM and digital twin"*, European Conference on Optical Communication (ECOC), 2024.

P10 Reda Ayassi, **Xin Yang**, Yvan Pointurier, Gabriel Charlet, Quoc Thai Nguyen, Yassine El Harraz, *"Field Trial Demonstration of Digital Twin Assisted Network Optimization on a Production Network"*, European Conference on Optical Communication (ECOC), 2024.

P11 Chenyu Sun, **Xin Yang**, Gabriel Charlet, Photios A Stavrou, Yvan Pointurier, *"Digital twin-enabled optical network automation: power re-optimization"*, Optical Fiber Communication Conference (OFC), 2024.

P12 Chenyu Sun, **Xin Yang**, Gabriel Charlet, Photios A Stavrou, Yvan Pointurier, *"Digital twin-enabled service optimization sequence of actions for power equalization"*, Asia Communications and Photonics Conference (ACP), 2023.

P13 Chenyu Sun, **Xin Yang**, Gabriel Charlet, Yvan Pointurier, *"Experimental assess-*

ment of joint impact of equalization and link failure in meshed networks", European Conference on Optical Communication (ECOC), 2023.

I have also published three PCT international patent applications:

P1 X. Yang, M. Tornatore, Y. Pointurier, G. Charlet, "An optical communication system for monitoring losses," PCT Patent Application 92043366PCT01, 2023.

P2 X. Yang, M. Tornatore, Y. Pointurier, G. Charlet, "An optical communication system for monitoring losses," PCT Patent Application 92043366PCT02, 2024.

P3 X. Yang, Y. Pointurier, G. Charlet, "An Amplication System and Method for Inter-Band Power Monitoring," PCT Patent Application 92030822PCT01, 2023.

Contents

Abstract **i**

Abstract **iii**

List of Publications **v**

Contents **ix**

1 Introduction **1**
1.1 Motivation and Objectives 1
1.2 State of the Art and Key Challenges 4
1.2.1 Topology of Physical-Layer Optical Networks 5
1.2.2 Digital Twin of Optical Networks 6
1.2.2.1 Quality of Transmission 7
1.2.2.2 Monitoring in Optical Networks 19
1.2.2.3 Network Automation 26
1.2.3 Data Center Interconnects 28
1.3 Contributions and Thesis Outline 29
1.3.1 Contributions 29
1.3.2 Thesis Outline 34

2 Experimental Impact of Power Re-Optimization in a Mesh Network **37**
2.1 Abstract 37
2.2 Introduction 37
2.3 Power Optimization Strategies 39
2.3.1 Static End-of-life (EoL) Design Strategy 39
2.3.2 Dynamic Real-time Strategy 40
2.4 Network Loading Scenario 41
2.5 Experimental Testbed 42

2.6 Results . . . 47
2.6.1 SNR Degradation by Loading New Services . . . 49
2.6.2 SNR Improvement by Power Re-optimization Strategies . . . 53
2.6.3 Predicted SNR vs. Monitored SNR with Power Re-optimization . . . 56
2.7 Conclusions . . . 57

3 QoT Estimation Improvement with Inputs Refinement Tool for C+L Networks 59
3.1 Abstract . . . 59
3.2 Introduction . . . 59
3.3 Setup and Assumptions . . . 60
3.4 Method Description . . . 61
3.5 Simulation Results . . . 62
3.6 Conclusions . . . 64

4 Digital-Twin-Based Active Inputs Refinement for Insertion Loss Estimation and QoT optimization in C and C+L Networks 65
4.1 Abstract . . . 65
4.2 Introduction . . . 66
4.2.1 Motivation . . . 66
4.2.2 State of the Art . . . 68
4.2.3 Contributions . . . 70
4.3 AIR Method Description . . . 71
4.4 QoT Optimization Leveraging Inputs Refinement . . . 74
4.5 Simulation Validation for AIR . . . 75
4.5.1 C-band Network . . . 77
4.5.1.1 Insertion Loss Estimation . . . 77
4.5.1.2 GSNR Margin Optimization . . . 78
4.5.1.3 GSNR Prediction . . . 79
4.5.1.4 GSNR Variation During AIR . . . 81
4.5.2 C+L Multi-Band Network . . . 82
4.5.2.1 Insertion Loss Estimation . . . 83
4.5.2.2 GSNR Margin Optimization . . . 84
4.5.2.3 GSNR Prediction . . . 85
4.5.2.4 GSNR Variation During AIR . . . 86
4.5.3 Robustness of Uncertainty of Power Monitoring and Fiber Attenuation Coefficient . . . 87
4.5.4 Power Monitoring Noise . . . 87

4.6 Experimental Validation in a C-Band Network . . . 88
4.6.1 Experimental Testbed . . . 89
4.6.2 Insertion Loss Estimation . . . 90
4.6.3 Impact of Insertion Loss Estimation on QoT Estimation, Prediction, and Optimization . . . 91
4.6.4 SNR Variation During AIR . . . 93
4.7 Discussion on AIR Application Conditions and Limitations . . . 94
4.7.1 Challenges . . . 94
4.7.2 Application Scenarios . . . 95
4.8 Conclusions . . . 96

5 Input Refinement with Incremental Learning for Accurate Digital Twin-Enabled Self-Driven QoT Optimization in Optical Networks 97
5.1 Abstract . . . 97
5.2 Introduction . . . 98
5.2.1 Motivation . . . 98
5.2.2 State of the Art . . . 100
5.2.3 Contributions . . . 102
5.3 IIR Method Description . . . 103
5.4 Simulation Validation for IIR . . . 106
5.4.1 Simulation Testbed . . . 106
5.4.2 Simulation Results . . . 110
5.4.2.1 Insertion Loss Estimation . . . 110
5.4.2.2 QoT Estimation and Prediction . . . 111
5.4.2.3 One-shot QoT Optimization . . . 112
5.5 Experimental Validation for IIR . . . 113
5.5.1 Experimental Testbed . . . 113
5.5.2 Experimental Results . . . 115
5.5.2.1 Insertion Loss Estimation . . . 116
5.5.2.2 QoT Estimation and Prediction . . . 118
5.5.2.3 IIR-enabled Multi-step QoT Optimization . . . 120
5.6 Conclusions . . . 121

6 Integrating PPE and Inputs Refinement for Enhanced QoT Estimation and Optimization in an Optical Mesh Network 123
6.1 Abstract . . . 123
6.2 Introduction . . . 123
6.3 Method Description . . . 124

6.4 Experimental Testbed . . . 126
6.5 Results . . . 126
6.5.1 Power Profile Estimation Enhancement . . . 127
6.5.2 Connector Insertion Loss Estimation and Anomaly Detection . . . 128
6.5.3 QoT Estimation Optimization . . . 129
6.6 Conclusions . . . 129

7 Capacity Scaling Limits of DCI Networks: A Comparative Study of ZR, ZR+, and High-Performance Transponders 131
7.1 Abstract . . . 131
7.2 Introduction . . . 131
7.3 Assumptions . . . 132
7.4 Experimental Testbed . . . 133
7.5 Modelling . . . 134
7.6 Results . . . 135
7.6.1 Impact of Channel Loading Order with Mux . . . 136
7.6.2 Capacity Analysis . . . 137
7.7 Conclusions . . . 138

8 Conclusion 139
8.1 Conclusions and Future Work . . . 139
8.1.1 Conclusions . . . 139
8.1.2 Future Work . . . 140

Copyright Statement 143

Bibliography 145

List of Figures 163

List of Tables 167

Acknowledgements 169

1 | Introduction

1.1. Motivation and Objectives

Optical networks form the backbone of wide-area digital infrastructures, transporting the vast majority of global data traffic and enabling the services that define today's information society. They support a wide spectrum of applications, ranging from bandwidth-intensive video streaming [37, 38, 55] and cloud computing [49, 64, 136] to Distributed Artificial intelligence (AI) training [54, 66, 73, 159] and high-performance computing [80, 81, 129]. In parallel, the proliferation of the Internet of Things (IoT) [61, 74, 83] and the rapid deployment of latency-sensitive mobile services in 5G and forthcoming 6G systems [23, 75, 121] impose unprecedented requirements on communication networks. These services demand extremely high throughput, deterministic latency, strict synchronization, and high availability, thereby tightening constraints on latency, jitter, and reliability while simultaneously accelerating the need for multi-terabit transport links.

While higher network layers manage orchestration, traffic grooming, and logical connectivity, the foundation of communication systems is dictated by the physical layer. In physical-layer optical networks, services carried by optical signals across long-haul and metro domains inevitably accumulate impairments arising from transmission distance and the traversal of network elements such as fibers, amplifiers, and filters. The evolution of these networks has been shaped by successive technological breakthroughs designed to mitigate such impairments to improve the service Quality of Transmission (QoT). Early milestones included the development of low-loss silica fibers, followed by Pure-Silica-Core Fibers (PSCF) [1, 62, 147] and, more recently, Hollow-Core Fibers (HCF) [30, 53, 158], which reduce power attenuation during transmission. Advances in semiconductor laser sources with narrow linewidths [21, 57, 131] provided stable, efficient light generation with reduced phase noise. A pivotal leap came with the advent of Erbium-Doped Fiber Amplifiers (EDFAs) [9, 31, 51] and Raman Amplifiers (RAs) [59, 65, 90], which eliminated the need for frequent Optical–Electrical–Optical (O–E–O) regeneration and enabled cost-effective long-haul transmission with reduced Amplified Spontaneous Emission (ASE) noise. The adoption of Wavelength-Division Multiplexing (WDM) multiplied ca-

pacity by allowing multiple wavelength channels to co-propagate within a single fiber. In parallel, Reconfigurable Optical Add–Drop Multiplexers (ROADMs) [72, 130] equipped with Wavelength-Selective Switches (WSSes) [46, 67, 139] introduced flexibility, scalability, and reduced filtering penalties, while coherent detection combined with advanced Digital Signal Processing (DSP) enabled digital compensation of Chromatic Dispersion (CD) [116, 146] and carrier phase noise [36, 92], and, together with nonlinear equalization techniques [2, 76], supported high-order and Probabilistic modulation formats and polarization multiplexing, thereby achieving significantly higher spectral efficiency, closing the gap to the Shannon limit. To further accommodate traffic growth, expanding the usable optical spectrum beyond the conventional C-band to include the L-band and potentially even the S-band. Such multi-band operation, however, brings stronger Inter-channel Stimulated Raman Scattering (ISRS) effects that must be carefully managed to fully realize the potential capacity gains [91, 111, 115].

Despite these advances, scalability remains a critical challenge in the face of the exponential traffic growth anticipated in the coming decades [16, 106]. This sustained increase not only amplifies the demand for raw transport capacity but also raises requirements for performance, resilience, and automation in optical infrastructure. Consequently, tremendous pressure is placed on the physical-layer optical networks [5, 102], which must be supported not only through continued hardware innovation but also through intelligent network management strategies. In recent years, advanced hardware monitoring devices such as Optical Channel Monitors (OCMs) [143], PhotoDiodes (PDs) [128], and Optical Time-Domain Reflectometers (OTDRs) [8] have significantly improved the observability of large-scale optical systems. When combined with real-time monitoring, digital twins, which are the virtualized replicas of physical networks, have emerged as powerful tools to simulate and predict "what-if" scenarios and to guide proactive decision-making [77, 125, 134, 137], enabling impairment-aware and automated resource optimization by modeling and predicting diverse physical impairments [156, 161]. Moreover, the integration of Software-Defined Networking (SDN) and AI into the control and management planes has further strengthened network robustness and automation [42, 120]. Such advances are indispensable as networks scale in size and dynamism, ensuring service continuity, enabling large-capacity transport, and supporting low-latency, highly automated operation. Ultimately, these approaches are essential to overcome the fundamental limitations of throughput, reach, resilience, and automation that originate at the physical layer.

The motivation of this thesis arises from the fundamental challenges faced by modern physical-layer optical networks in sustaining performance under persistent exponential traffic growth considering the robustness and automation of optical networks, where im-

pairments (e.g., fiber nonlinearities, amplifier noise, filtering penalties, transponder end-to-end limitations) accumulate over long transmission paths and ultimately constrain service QoT. Although these impairments have been extensively characterized and modeled in controlled experimental environments, their impact under realistic commercial monitoring conditions remains insufficiently understood. This is largely due to the lack of observability of key parameters in deployed systems, while practical monitoring solutions are constrained by cost, sensitivity, and accessibility. Consequently, operators face a widening gap between the theoretical understanding of transmission physics and the actionable network visibility required to ensure reliable and scalable operation.

Against this backdrop, this thesis aims to bridge the gap between theoretical impairment modeling and operational practice through a systematic analysis of the interplay among physical-layer impairments, monitoring strategies, and optimization frameworks. The key contributions are summarized as follows:

- **Mitigating QoT degradation with power re-optimization:** I study the impact of the widely adopted "set-and-forget" power setting strategy [24, 71, 99] on the Quality of Transmission (QoT) in optical networks and propose methods to mitigate its drawbacks. In this strategy, newly established services are assigned fixed launch powers while the powers of existing services are allowd to drift freely, which gradually leads to power imbalances as the network evolves due to amplifier dynamics, the SRS effect, and network aging (i.e., slow parameter drift caused by long-term fiber and amplifier degradation). These imbalances exacerbate the accumulation of linear and nonlinear impairments along the transmission path, causing QoT variation and degradation for already active services. To address this issue, I classify and apply two power re-optimization strategies: a static approach based on end-of-life parameters (low operational complexity but limited adaptability to evolving network conditions) and a dynamic approach informed by real-time network monitoring (adaptive to network evolution but with increased monitoring and control overhead). Experimental validation on a mesh optical testbed shows that both strategies effectively restore the QoT of degraded services, thereby improving the robustness and capacity of evolving optical networks without relying on intrusive real-time feedback.
- **Advanced monitoring methodologies:** I propose multiple advanced monitoring strategies that exploit diverse sources of data collected in operational networks to refine unknown or poorly observed parameters critical for accurate QoT modeling. By systematically integrating information from transceiver telemetry, amplifier monitoring elements, optical channel monitors, and coherent receiver DSPs, these

strategies enhance visibility into otherwise hidden network states. The refined parameter estimation improves the fidelity of QoT models, enabling precise anomaly detection and localization, accurate QoT prediction, and efficient power optimization, thereby narrowing the gap between theoretical models and practical network operations. This enhanced visibility further supports reliable and intelligent automation control of optical networks, which is essential for scaling network capacity, maintaining high service availability, and meeting the stringent requirements of emerging applications.

- **Design features for Data Center Interconnect (DCI) networks:** I investigate the design trade-offs for DCI networks, which represent one of the fastest-growing segments of optical networking due to the explosive rise of cloud computing, content delivery, and AI-driven workloads. Unlike wide-area backbone networks, DCIs are characterized by highly predictable, high-capacity, and latency-sensitive flows between geographically distributed data centers. They demand extreme scalability in per-wavelength capacity, spectral efficiency, and energy performance, while requiring operational simplicity and rapid deployability. In this thesis, I benchmark the impact of different types of transponders, multiplexer architectures, and channel allocation strategies on capacity and efficiency in DCI environments, offering guidelines for the design and operation of next-generation systems.

By integrating these elements into a coherent framework, the overarching objective of this work is to enhance the capacity, robustness, and operational efficiency (automation) at the physical layer, thereby advancing the state-of-the-art in the maintenance of the performance and scalability of optical networks in the face of continuously increasing traffic demand.

1.2. State of the Art and Key Challenges

1.2.1. Topology of Physical-Layer Optical Networks

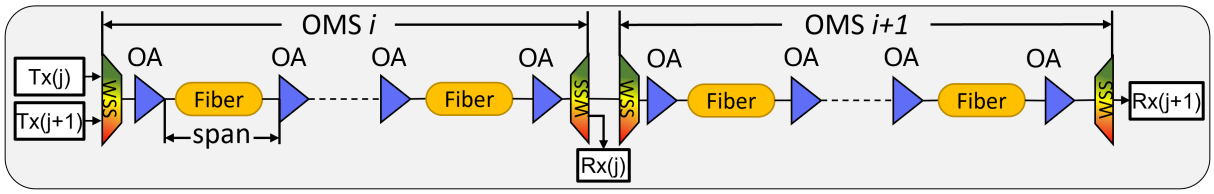


Figure 1.1: Example of service j transmitted from the transceiver to the receiver, traversing one optical multiplex section (OMS) i, and service $j+1$ propagating across OMS i and OMS $i+1$, passing through multiple optical amplifiers, fiber spans, and reconfigurable WSSes.

Physical-layer optical networks constitute the photonic transport substrate that carries optical signals to transmit end-to-end services. They comprise fibers, booster Optical Amplifiers (OAs), in-line and pre-OAs, ROADMs equipped with WSSes, filters, Variable Optical Attenuators (VOAs), connectors between optical components, and optical monitors (described in later sections). Their primary functions are to multiplex, switch, route, and amplify WDM signals under spectrum and power constraints, while managing physical impairments such as attenuation, Amplified Spontaneous Emission (ASE) noise, Chromatic Dispersion (CD), Polarization-Mode Dispersion (PMD), Kerr nonlinearities, and Stimulated Raman Scattering (SRS). Ultimately, they provide transparent optical connections to higher network layers.

End-to-End (E2E) services refer to logical client-layer transport entities, such as OTN connections, that carry user traffic from a source node to a destination node. In the optical transport layer defined by ITU-T G.872, each service is mapped onto one or more Optical Channels (OChs), which represent end-to-end optical connections between optical channel termination points (typically transponders or muxponders). Each OCh may correspond to a single wavelength, a set of subcarriers, or a superchannel occupying contiguous frequency slots. Along its path, the OCh traverses multiple Optical Multiplex Sections (OMSes) and Optical Transmission Sections (OTSs), and may undergo O-E-O regeneration at intermediate nodes when required. Provisioning involves coordinated decisions on routing, modulation format, baud rate, Forward Error Correction (FEC), and spectrum assignment while satisfying continuity and contiguity constraints, as well as guard-band and multi-band (i.e., S, C, L) considerations. Network operation is typically orchestrated by a control plane, such as an SDN controller, which supervises latency, availability, and protection/restoration objectives.

Optical Multiplex Section (OMS) refers to the portion of the optical line system where a set of WDM channels co-propagate over the same fiber and in the same direction between two multiplexing points (e.g., passive multiplexers or WSS-based ROADMs). Within an OMS, all channels traverse the same sequence of in-line elements responsible for amplification and filtering. Per-channel power is typically equalized at the beginning of the OMS by configuring the attenuation of WSS. OMS boundaries arise at points where channels are added or dropped, or where the entire WDM group is demultiplexed and subsequently remultiplexed. A multi-hop service generally traverses multiple OMSes in succession, each consisting of a cascade of optical spans.

Optical span (or simply span) is the fundamental physical fiber segment between two active amplification points along an Optical Multiplex Section (OMS). In ITU-T G.872 terminology, one or more consecutive spans together form an Optical Transmission Section (OTS). In practice, each span extends from the output of one amplifier to the input of the next downstream amplifier, with the first span beginning at the transmitter-side booster and ending at the first in-line amplifier. The total optical power can be equalized at the span level by adjusting the per-span amplifier gain and tilt to manage the total power and spectral tilt entering the fiber. Key characteristics include span length, wavelength-dependent attenuation, connector insertion and splice losses, dispersion parameters, nonlinear and Raman coefficients, and the total input and output power at amplifiers, as well as the launch power entering the fiber. Many dominant physical-layer impairments and their accumulation, including ASE, Kerr effects, and SRS effect, are managed at the span level.

1.2.2. Digital Twin of Optical Networks

Digital twin (DT) technology has recently emerged as a key enabler for optical network automation, providing a virtual replica of the physical infrastructure to support planning, prediction, optimization, and troubleshooting [134, 137]. A DT is commonly structured around three pillars: modeling, real-time monitoring, and automatic control [35]. Modeling combines analytical and machine-learning methods to predict network behavior while real-time monitoring leverages hardware-based and software-absed solutions for in-situ measurements. Automatic control then closes the loop by enabling DT-assisted configuration of amplifiers, WSSes, and transponders for power optimization and restoration. Despite promising demonstrations, practical deployment faces challenges such as limited observability, vendor heterogeneity, and traffic-preserving constraints [140].

In this thesis, we adopt a hybrid strategy that integrates hardware-based monitoring,

ML-driven input parameter refinement, and analytical models, to establish accurate and scalable DTs shown in 1.2 for QoT prediction and optimization in single-band and multi C+L-band systems.

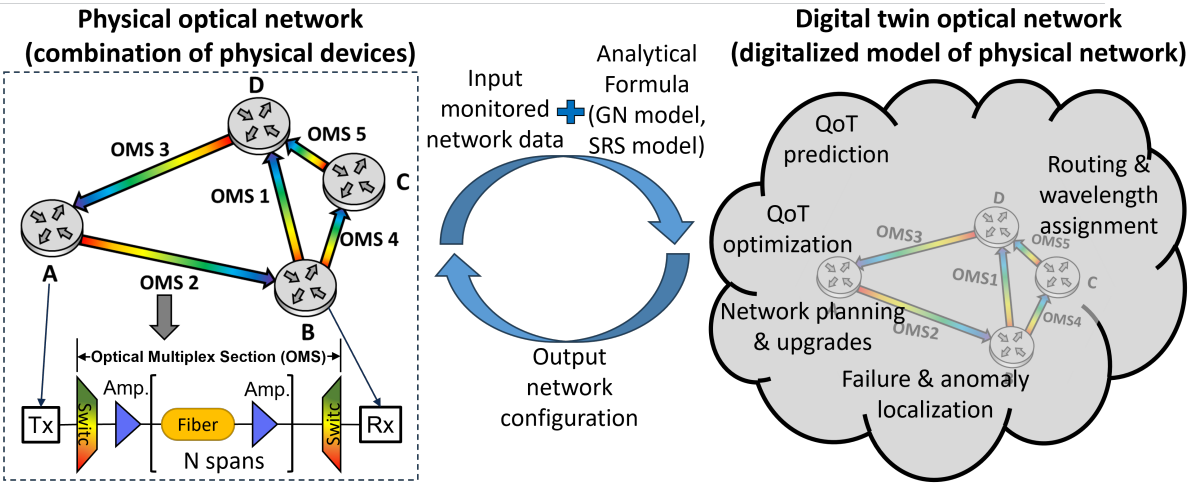


Figure 1.2: Proposed DT framework.

Building upon this foundation, we next introduce the concept of Quality of Transmission (QoT), which serves as the central performance metric that DTs aim to predict and optimize in optical networks.

1.2.2.1. Quality of Transmission

Definition **Quality of Transmission (QoT)**, commonly referred to as signal integrity in optical networks, is quantified by physical-layer performance metrics such as bit error rate (BER), Q-factor, and signal-to-noise ratio (SNR). QoT is determined by the cumulative impact of physical-layer impairments accumulated along an end-to-end transmission path. Major contributors include:

- **Amplified Spontaneous Emission (ASE) noise:** Generated by optical amplifiers, ASE noise accumulates incoherently across spans and sets a fundamental limit on the optical signal-to-noise ratio (OSNR).
- **Fiber Kerr Nonlinear Interference (NLI):** Arising from the interaction between optical fields and the fiber medium, intensity-dependent refractive index variations induce nonlinear phase distortions that degrade SNR. In coherent optical systems, chromatic dispersion (CD) does not directly impair transmission performance due to effective digital compensation; however, it plays a critical role in shaping nonlinear interactions by altering the temporal and spectral overlap among channels. The

dominant Kerr nonlinear effects include:

  - *Self-Phase Modulation (SPM):* Phase modulation of a channel by its own intensity, leading to spectral broadening in combination with chromatic dispersion.
  - *Cross-Phase Modulation (XPM):* Phase shifts induced on a channel by co-propagating neighboring channels, causing inter-channel crosstalk.
  - *Four-Wave Mixing (FWM):* Nonlinear mixing of three channels that generates new frequency components. In modern systems with nonzero dispersion fibers and irregular channel spacing, FWM efficiency is strongly suppressed and is typically negligible compared to SPM and XPM.

- **Stimulated Raman Scattering (SRS):** A nonlinear inter-channel power transfer process where shorter-wavelength channels transfer energy to longer-wavelength channels. Especially in wideband (i.e., C+L, S+C+L) transmission systems, SRS induces spectral tilt and unequal OSNR among channels, necessitating active power equalization.
- **Transponder back-to-back (B2B) impairments:** Imperfections in transmitter and receiver subsystems, including finite laser linewidth, IQ (received) power imbalance, digital-to-analog/analog-to-digital conversion limitations, and Digital Signal Processing (DSP) penalties.
- **Filtering penalty:** Cascaded filtering by Wavelength-Selective Switches (WSSes), multiplexers/demultiplexers, and optical filters induces inter-symbol interference, passband narrowing, and crosstalk, particularly in flex-grid networks with tightly packed channels.
- **Polarization-related impairments (PMD and PDL):** Polarization Mode Dispersion (PMD) arises from random birefringence in optical fibers, introducing differential group delay between polarization modes that leads to pulse broadening and inter-symbol interference. Polarization Dependent Loss (PDL) originates from polarization-sensitive components such as WSSes, VOAs, and connectors, causing unequal attenuation of different polarizations and fluctuations in received SNR. Both effects are inherently random and time-varying, which makes them difficult to monitor and manage in practical systems. In this thesis, PMD and PDL are not studied, hence neglected; in real deployments, their impact is typically accounted for through additional system margin [102].

In this thesis, the signal-to-noise ratio (SNR) is adopted as the main representative QoT metric. Unless otherwise stated, SNR-related quantities are expressed in *linear scale*. For

a given modulation format, SNR can be directly inferred from the bit error rate (BER). A convenient decomposition of the end-to-end SNR in linear scale can be expressed as:

$$\mathrm{SNR}^{-1} \approx \mathrm{SNR}_{\mathrm{ASE}}^{-1} + \mathrm{SNR}_{\mathrm{NLI}}^{-1} + \mathrm{SNR}_{\mathrm{B2B}}^{-1},$$

where $\mathrm{SNR}_{\mathrm{ASE}}$ quantifies the degradation due to amplified spontaneous emission (ASE) noise, $\mathrm{SNR}_{\mathrm{NLI}}$ captures the impact of fiber Kerr nonlinear interference (NLI), and $\mathrm{SNR}_{\mathrm{B2B}}$ accounts for transponder back-to-back (B2B) penalties. These terms represent independent noise contributions and are therefore summed in inverse SNR form in linear scale.

Additional filtering penalties arising from cascaded multiplexer/demultiplexer elements are treated separately and incorporated in the logarithmic domain. Specifically, the overall SNR including filtering effects is expressed in decibel (dB) scale as:

$$\mathrm{SNR}_{\mathrm{dB}} = 10 \log_{10}(\mathrm{SNR}) - \mathrm{FP},$$

where FP denotes the cumulative filtering penalty expressed in dB. This formulation ensures consistency with the physical nature of filtering distortions, which manifest as multiplicative power losses.

This decomposition distinguishes line noise, nonlinear interference, transponder implementation limits, and filtering distortions, and establishes the structured framework adopted throughout this thesis for QoT modeling and prediction. In particular, it forms the basis for the digital-twin approaches developed in later chapters, where refined parameter estimation and closed-loop optimization are applied to accurately model and mitigate these dominant sources of signal degradation.

The operating margin of a service is defined in dB scale as:

$$\mathrm{SNR}_{\mathrm{margin,dB}} = \mathrm{SNR}_{\mathrm{dB}} - \mathrm{SNR}_{\mathrm{FEC,dB}},$$

where $\mathrm{SNR}_{\mathrm{FEC,dB}}$ denotes the minimum SNR threshold required to achieve "error-free" operation after forward error correction (FEC) decoding. The SNR margin thus quantifies the robustness of a service against additional impairments induced by network reconfiguration, such as channel add/drop operations.

While SNR aggregates all sources of degradation, the generalized signal-to-noise ratio (GSNR) isolates the contribution of the optical transmission line, including ASE noise

from optical amplifiers and nonlinear interference from the fiber, without conflating these effects with transponder back-to-back penalties. This separation makes GSNR a robust and transponder-agnostic figure of merit, enabling fair evaluation of line impairments independent of vendor-specific implementations. Consequently, GSNR has become the de facto metric for benchmarking transmission reach, capacity scaling, and line system performance.

In this thesis, GSNR is computed independently for each Optical Multiplex Section (OMS). All GSNR-related quantities are expressed in linear scale. The total ASE and nonlinear interference contributions along a lightpath are obtained by incoherently summing the inverse SNR components of all OMSes. Formally, GSNR is expressed as:

$$\mathrm{GSNR}^{-1} = \mathrm{SNR}_{\mathrm{ASE}}^{-1} + \mathrm{SNR}_{\mathrm{NLI}}^{-1} = \sum_{\mathrm{OMS}} \left(\mathrm{SNR}_{\mathrm{ASE,OMS}}^{-1} + \mathrm{SNR}_{\mathrm{NLI,OMS}}^{-1} \right).$$

Modeling QoT prediction plays a central role in the design and provisioning of optical networks. Alongside traditional analytical models, machine-learning (ML)–based techniques have recently gained attention as data-driven alternatives. Existing work in this area can be broadly grouped into four categories:

- First, classification models evaluate the feasibility of candidate lightpaths by exploiting features such as path length, modulation format, and amplifier settings [17, 84, 95]. While computationally efficient, these models only provide binary feasibility decisions and lack the granularity to quantify QoT margins, making them less informative for fine-grained optimization.
- Second, regression models predict quantitative QoT metrics—including OSNR, SNR, and BER—with sub-dB precision, in some cases outperforming analytical baselines, though often with reduced accuracy and generalizability across different link configurations [34, 58, 88, 132, 142].
- Third, generalization-oriented strategies, such as transfer learning and active learning, aim to reduce the burden of training data collection by reusing knowledge across heterogeneous networks and selectively acquiring new samples. Transfer learning for QoT estimation is, however, limited by domain mismatch, sparse and noisy target data, feature inconsistencies across networks, and the risk of negative transfer under aging or reconfigurations [7, 100, 109, 144, 157].
- Finally, hybrid and composable architectures combine component-level modeling with end-to-end learning to improve scalability and accuracy. Examples include cas-

caded learning frameworks that integrate pre-trained EDFA models with lightweight trainable layers refined by minimal end-to-end measurements [141], as well as modular approaches such as CompQoTE, which employs reusable Launch, Propagation, and Readout modules to generalize across arbitrary and unseen lightpaths [47].

Despite these advances, ML-based approaches face intrinsic limitations: they depend on extensive and high-quality datasets (i.e., OSNR measurement, amplifier characteristics, etc.) that are seldom available in commercial systems due to vendor lock-in, lack of standardized monitoring interfaces, and restricted data sharing. Moreover, their performance is sensitive to network reconfiguration, topology evolution, and device aging, which raises concerns about long-term robustness in real deployments.

In contrast, analytical physical-layer models are grounded in well-established transmission physics. They provide not only accuracy but also interpretability and inherent generality, without requiring training datasets. Such models account for dominant impairments including attenuation, CD, ASE noise, Kerr nonlinearities, and SRS [69, 101]. Among them, the Split-Step Fourier Method (SSFM) [69] is often regarded as the accuracy benchmark, although its computational demands make it impractical for real-time applications. To reduce complexity, approximate formulations have been proposed. The Gaussian Noise (GN) model [40, 101] assumes that nonlinear interference (NLI) behaves as additive Gaussian noise, enabling closed-form estimates of QoT. Its refinements, such as the Enhanced GN (EGN) model [20], improve accuracy by accounting for signal–NLI correlations and modulation-format dependence, while the Incoherent GN (IGN) model [101] offers simplified yet computationally efficient approximations. Furthermore, closed-form GN variants incorporating SRS effects extend applicability to wideband systems [117]. Recent studies combine analytical models with bias-fitting techniques to absorb unmodeled effects such as location-specific spectral deviations, amplifier gain inaccuracies, and filtering penalties, thereby improving QoT prediction [4, 56], however, effective QoT optimization remains challenging due to lack of estimation of key parameters. To address this, an efficient approach is to update the input of analytical formula with continuous real-time monitoring or refined data to keep it effective (introduced in 1.2.2.2), for instance by updating fiber insertion losses, amplifier spectra, noise figures, or transponder/filter characteristics. This capability ensures robustness and scalability in operational environments where features are considerably harder to guarantee with ML-based approaches. Accurate knowledge of input parameters is therefore one of the main challenges and critical to ensure accurate QoT prediction and effective optimization [41, 63].

Therefore, a hybrid approach that leverages analytical models (e.g., closed-form GN [117]) in combination with ML-based parameter refinement techniques, called *Input Refinement*

(IR), constitutes the main methodology adopted in this thesis for QoT prediction.

In the following, we provide an overview of analytical QoT modeling approaches, highlighting their assumptions, approximations, and applicability in operational networks:

Fiber nonlinear noise is estimated by one of the most widely adopted analytical frameworks called the *Gaussian Noise (GN) model*. It is based on the observation that, in coherent WDM systems with many channels and significant chromatic dispersion, the nonlinear distortions generated by Kerr effects (SPM, XPM, and FWM) accumulate in a noise-like fashion and can therefore be approximated as additive Gaussian noise. Under this assumption, the Nonlinear Interference (NLI) can be modeled as an equivalent noise source that adds incoherently to ASE noise and other impairments in the end-to-end SNR decomposition. It relies on the following assumptions:

- *Perturbative regime:* Nonlinear effects are treated as small perturbations to the linear signal propagation.
- *Signal Gaussianity:* After propagation through highly dispersive fiber, the transmitted waveform can be approximated statistically as a Gaussian process.
- *Additive Gaussian noise:* Nonlinear distortions accumulate as incoherent, noise-like contributions whose optical field amplitude (both in-phase and quadrature components) follows a zero-mean Gaussian distribution, independent of the transmitted symbols.

These assumptions are valid in dispersion-uncompensated links, where accumulated chromatic dispersion decorrelates symbols and renders nonlinear distortions approximately Gaussian, as in most modern coherent systems.

The nonlinear interference Power Spectral Density (PSD) at frequency f can be expressed as the incoherent sum of all non-degenerate FWM processes among the WDM channels [101]:

$$GNLI(f) = \frac{16}{27}\gamma^2 L_{\text{eff}}^2 \iint G_{\text{WDM}}(f_1)\, G_{\text{WDM}}(f_2)\, G_{\text{WDM}}(f_1+f_2-f) \times \rho(f_1,f_2,f)\, \chi(f_1,f_2,f)\, df_1\, df_2,$$

where γ is the fiber nonlinear coefficient, L_{eff} the effective fiber length, $G_{\text{WDM}}(f)$ the transmitted signal PSD, $\rho(f_1,f_2,f)$ the mixing efficiency, and $\chi(f_1,f_2,f)$ the phased-array factor describing coherent accumulation across spans.

Although the GN model provides tractable closed-form approximations, it does not ac-

count for modulation-dependent statistics or finite symbol coherence. The Enhanced GN (EGN) model [101] improves accuracy by including these effects. For ultra-wideband transmission (C+L band and beyond), Inter-channel Stimulated Raman Scattering (ISRS) is more evident than single C-band systems. ISRS redistributes power from shorter to longer wavelengths, modifying the nonlinear interference. The ISRS GN model [117] incorporates the Raman slope C_r into the effective attenuation profile and extends the closed-form SPM/XPM formulas to capture spectral tilt and channel-dependent OSNR.

The GN model expresses the NLI power on channel i as a function of fiber parameters (nonlinear coefficient γ, dispersion β_2, attenuation α), the channel spacing and modulation format, and the per-channel launch power. It enables closed-form approximations of $\mathrm{SNR}_{\mathrm{NLI}}$ that are sufficiently accurate for network planning and optimization, while being computationally efficient compared to split-step Fourier simulations. Extensions such as the Enhanced GN (EGN) model further improve accuracy by accounting for modulation-dependent effects, signal coherence, and inter-channel stimulated Raman scattering (ISRS).

The closed-form EGN model approximates the NLI coefficient $\eta(f_i)$ as the combination of SPM and XPM terms:

- **SPM contribution**:

$$\eta_{\mathrm{SPM}}(f_i) \approx \frac{4}{9}\frac{\gamma^2}{B_i^2}\frac{\pi}{\varphi_i\,\bar{\alpha}\,(2\alpha+\bar{\alpha})}\left[T_i - \alpha\,\operatorname{asinh}\!\left(\frac{\varphi_i B_i^2}{\pi\alpha}\right) + \frac{A^2-T_i}{A}\,\operatorname{asinh}\!\left(\frac{\varphi_i B_i^2}{\pi A}\right)\right],$$

  where γ is the fiber nonlinear coefficient, B_i the bandwidth of channel i, α the fiber attenuation, $\bar{\alpha}$ the effective attenuation, $A = \alpha + \bar{\alpha}$, $\varphi_i = \frac{3}{2}\pi^2(\beta_2 + 2\pi\beta_3 f_i)$ with β_2 and β_3 the dispersion coefficients, f_i the center frequency of channel i, P_{tot} the total launch power, C_r the Raman gain slope, and $T_i = (\alpha + \bar{\alpha} - P_{\mathrm{tot}}C_r f_i)^2$.

- **XPM contribution**:

$$\eta_{\mathrm{XPM}}(f_i) \approx \frac{32}{27}\sum_{\substack{k=1\\k\neq i}}^{N_{\mathrm{ch}}}\left(\frac{P_k}{P_i}\right)^2\frac{\gamma^2}{B_k\,\varphi_{i,k}\,\bar{\alpha}\,(2\alpha+\bar{\alpha})} \times\left[T_k - \alpha\,\arctan\!\left(\frac{\varphi_{i,k}B_i}{\alpha}\right) + \frac{A^2-T_k}{A}\,\arctan\!\left(\frac{\varphi_{i,k}B_i}{A}\right)\right],$$

  where P_i and P_k are the launch powers of channel i and interferer k, B_k is the bandwidth of channel k, N_{ch} the number of WDM channels, $\varphi_{i,k} = 2\pi^2(f_k - f_i)(\beta_2 + \pi\beta_3(f_i + f_k))$ the phase-mismatch factor, f_k the center frequency of channel k, and $T_k = (\alpha + \bar{\alpha} - P_{\mathrm{tot}}C_r f_k)^2$.

By combining SPM and XPM, the span-wise accumulation of Kerr nonlinear interference is expressed as:

$$\eta_n(f_i) \approx \sum_{j=1}^{n} \left(\frac{P_{i,j}}{P_i} \right)^2 \left[\eta_{\mathrm{SPM},j}(f_i)\, n\epsilon + \eta_{\mathrm{XPM},j}(f_i) \right],$$

where n is the number of fiber spans, $P_{i,j}$ the launch power of channel i at span j, and ϵ the coherence factor that accounts for partial accumulation of NLI across spans.

Finally, with $P_{\mathrm{NLI}} = \eta_n(f_i)\, P_i^3$, the nonlinear SNR becomes:

$$\mathrm{SNR}_{\mathrm{NLI}} = \frac{P_i}{P_{\mathrm{NLI}}} = \frac{1}{\eta_n(f_i)\, P_i^2}.$$

In this thesis, the EGN model (and its closed-form ISRS-aware extensions) is employed as the analytical foundation for estimating $\mathrm{SNR}_{\mathrm{NLI}}$, enabling efficient and accurate integration of nonlinear noise prediction into the QoT prediction and optimization framework.

ASE noise is generated by optical amplifiers and is determined by their gain and noise figure. The $\mathrm{SNR}_{\mathrm{ASE}}$ can be expressed as:

$$\mathrm{SNR}_{\mathrm{ASE}}^{-1} = \frac{P_{\mathrm{ASE}}}{P_{\mathrm{Signal}}} = \frac{h\,\nu\,G\,NF\,B}{P_{\mathrm{Signal}}},$$

where P_{ASE} is the accumulated ASE noise power, $h\nu$ the photon energy, G the amplifier gain, NF the noise figure, and B the bandwidth of the optical signal.

Transponder back-to-back (B2B) impairments represent the intrinsic implementation penalties of coherent transceivers, even in the absence of fiber propagation. They define the baseline performance limit due to imperfections in the transmitter, receiver, and associated digital signal processing (DSP).

The main sources of B2B penalties include:

- **Laser phase noise and finite linewidth:** Causes residual phase fluctuations, particularly critical for high-order modulation formats.
- **IQ modulator non-idealities:** Bias drift, quadrature imbalance, and finite extinction ratio distort the transmitted constellation.
- **DAC/ADC limitations:** Quantization noise, limited sampling resolution, and bandwidth constraints introduce errors in the conversion process.

- **Receiver front-end noise:** Thermal noise, shot noise, and transimpedance amplifier (TIA) noise reduce effective sensitivity.
- **DSP implementation penalties:** Imperfect equalization, carrier and phase recovery, and finite-precision arithmetic degrade overall performance.

To quantify these effects, B2B performance is typically measured experimentally by directly connecting the transmitter output to the receiver input without fiber propagation. The resulting maximum achievable SNR is then measured and defined as the $\mathrm{SNR}_{\mathrm{B2B}}$ term in the QoT model.

WSS filtering penalty can be estimated using Minimum Mean-Square Error (MMSE) models to capture the impact of cascaded filtering stages such as multiplexers and demultiplexers [29]. In-line optical filtering cannot be treated as a simple Additive White Gaussian Noise (AWGN) source, because it simultaneously introduces Inter-Symbol Interference (ISI) and colors the noise spectrum. Therefore, its effect must be modeled using digital communications theory of band-limited channels with linear equalization.

In this framework, the equivalent channel transfer function can be expressed as:

$$H_{\mathrm{eq}}(f) = C(f)W(f),$$

where $C(f)$ represents the cascade of the transmitter pulse-shaping filter $g(f)$ and all traversed WSS filtering functions $H_i(f)$, while $W(f)$ is a whitening filter derived from the colored ASE noise power spectral density (PSD). By applying an MMSE equalizer at the receiver, the noise at the DSP input is rendered approximately white, enabling analytical SNR computation.

In this model, the post-equalization SNR is analytically derived from the equivalent channel response $H_{\mathrm{eq}}(f)$ and the total noise power spectral density $N_0 = N_0^{(L)} + N_0^{(NL)}$, where $N_0^{(L)}$ accounts for transmitter, receiver, and ASE noise contributions, and $N_0^{(NL)}$ represents nonlinear distortions approximated as AWGN. The resulting SNR can then be mapped to Q^2 or BER using standard relationships for the considered modulation format.

The MMSE approach inherently accounts for different ASE noise-loading distributions (e.g., noise injected before the filter cascade, between WSS stages, or only at the receiver), all of which significantly influence performance. Consequently, the filtering penalty represents the residual OSNR degradation induced by cascaded WSS filtering and is evaluated within the MMSE framework, providing a tractable and accurate model for QoT degradation in flexible-grid WDM networks.

Together, the above models provide the analytical foundation for the QoT prediction and optimization framework adopted in this thesis. By decomposing end-to-end SNR into the dominant contributions of ASE noise, fiber nonlinear interference, transponder implementation penalties, and filtering effects, the framework captures the essential physical-layer mechanisms that constrain service quality. This unified formulation enables both tractable analysis and accurate integration into digital-twin modeling, monitoring, and optimization strategies discussed in the subsequent chapters.

Optimization QoT optimization plays a central role in ensuring reliable service delivery and efficient spectrum utilization in optical networks. In physical-layer optical networks, QoT optimization is typically achieved by: (1) optimizing the output power spectrum of booster amplifiers at OMSes through per-channel WSS attenuation control, and (2) optimizing the total output power and spectral tilt at spans by configuring amplifier gain and tilt. Existing approaches can be broadly categorized into three classes: (i) analytical/convex formulations, (ii) Local-Optimum-Global-Optimum (LOGO) style heuristics, and (iii) data-driven strategies. Most of these techniques operate on per-channel launch powers or amplifier working points. Most of these techniques operate on per-channel launch powers or amplifier operating points to balance signal quality and nonlinear interference across the network.

First, convex optimization approaches exploit the convexity of GSNR in the logarithmic power domain, enabling mathematically optimal solutions with guaranteed convergence [50, 107]. While they provide provable optimality, their practicality is limited by the need for accurate analytical models and scalability concerns in large and dynamic networks.

Second, LOGO-style heuristics apply a span-by-span local optimization followed by a global smoothing phase [101]. Starting from the additive SNR decomposition:

$$\mathrm{SNR}^{-1} \approx \mathrm{SNR}_{\mathrm{ASE}}^{-1} + \mathrm{SNR}_{\mathrm{NLI}}^{-1} + \mathrm{SNR}_{\mathrm{B2B}}^{-1} + \mathrm{FP},$$

with

$$\mathrm{SNR}_{\mathrm{NLI}} = \frac{P_{\mathrm{signal}}}{P_{\mathrm{NLI}}} = \frac{1}{\eta\, P_{\mathrm{signal}}^2}, \qquad \mathrm{SNR}_{\mathrm{ASE}}^{-1} = \frac{P_{\mathrm{ASE}}}{P_{\mathrm{Signal}}}$$

the optimum operating point is obtained from the stationarity condition

$$\frac{d\,\mathrm{SNR}}{d\,P_{\mathrm{Signal}}} = 0,$$

which yields the well-known balance

$$\frac{P_{\mathrm{ASE}}}{P_{\mathrm{NLI}}} = 2.$$

Accordingly, the optimum per-channel power is expressed as

$$P_{\mathrm{LOGO}} = \sqrt[3]{\frac{P_{\mathrm{ASE}}}{2\eta}}.$$

where η denotes the fiber nonlinear coefficient.

These methods are computationally efficient but lack global optimality guarantees, and their convergence can be sensitive to network conditions, as they rely on simplifying assumptions such as flat amplifier gain, uniform fiber attenuation, and the neglect of Stimulated Raman Scattering (SRS). Consequently, LOGO yields a flat power allocation across channels. LOGO has been extended in multi-band regimes, where inter-channel stimulated Raman scattering (ISRS) induces strong spectral tilt [28, 115], and recent extensions combine it with gradient-based refinements to accelerate convergence in dynamic scenarios, such as three-step amplifier configuration algorithms that sequentially balance ASE, Kerr nonlinearity, and SRS across C+L links [122]. Another network-wide SNR-based optimization approach generalizes the LOGO-style heuristics concept, reallocating channel powers across multiple OMSes to maximize the worst-channel margin [48]. Similarly, frequency-dependent power control strategies in C+L systems extend the LOGO paradigm to multiband operation, where GN-based rules such as pre-tilting of the L-band while keeping the C-band flat equalize QoT across bands [39].

Third, cognitive and autonomous optical line controllers extend GN-based optimization by integrating telemetry (e.g., optical channel monitors, photodiodes, BER probes) with stochastic search strategies to dynamically adapt amplifier tilt and gain under reconfigurations [12, 104].

Despite these advances, both convex and heuristic QoT optimization methods remain tied to GN/EGN assumptions and require accurate input parameters. Their performance may degrade under reconfigurations, topology changes, or equipment aging, raising concerns about robustness in long-term deployment.

To address these limitations, data-driven approaches exploit machine learning either to complement or replace analytical models. Surrogate models trained on GN-generated datasets reproduce QoT evaluations with high accuracy and significantly reduced complexity [50]. Iterative supervised learning with BER feedback has been experimentally shown

to stabilize GSNR and mitigate ripple effects [13]. More advanced digital twin–assisted schemes employ symmetric neural-network optimizers that combine forward and inverse models to support customizable GSNR targets (flat, step, square-wave) and adapt to dynamic partial loading in C+L systems, maintaining accurate power control even across cascaded spans with WSS adjustments [96]. Beyond these, Large Language Models (LLMs) have recently been demonstrated as powerful AI agents for optical network optimization. The first field trial of an LLM-powered agent for Autonomous Driving Optical Networks (ADON) showed that LLMs can autonomously handle service provisioning, failure recovery, and directly optimize amplifier gains, achieving near-optimal QoT in real-time operation [78].

In summary, QoT optimization methods have evolved from static flat allocations to dynamic closed-loop strategies, progressing from analytical convex formulations to LOGO-style heuristics (including network-wide and multiband extensions), and, most recently, to data-driven digital-twin and LLM-assisted approaches that enable scalable, adaptive, and flexible operation in both single- and multi-band networks. In this thesis, we adopt a hybrid optimization approach: closed-form GN-based heuristic method is applied to optimize per-channel launch power, targeting a balance of $\frac{P_{\text{ASE}}}{P_{\text{NLI}}} = 2$ in C-band networks. This method, originally proposed in [115], is extended to C+L band operation, while amplifier settings (gain and tilt) are configured following the approaches in [39, 115]. The proposed framework is further enriched with accurate input parameter estimation through advanced ML-based Input Refinement techniques (introduced in Section 1.2.2.2), thereby combining the interpretability and physical grounding of analytical models with the adaptability and robustness of machine learning to achieve reliable and efficient QoT optimization in practical commercial optical networks.

However, in realistic optical networks, QoT is inherently dynamic and evolves over time due to two main categories of effects:

- *load-dependent interactions* modify the power distribution whenever services are added, rerouted, or dropped. These changes alter the amplifier dynamics, SRS-induced spectral tilt and the NLI [77, 150].
- *gradual degradations in plant and equipment* accumulate over time, including contamination or aging of the fiber connectors and splices, and filter pass-band drift, all of which exacerbate ASE and nonlinear penalties [153].

These realities highlight that reliable, efficient, and automated QoT (re-)optimization at the physical layer is essential not only during initial network planning but also as a continuous operational process. Sustaining QoT above service thresholds in the presence

of traffic churn and equipment aging is therefore a cornerstone of scalable and resilient optical network design [13, 24, 39, 48, 78, 107, 150].

To meet this need, emerging approaches increasingly rely on **Digital Twins (DTs)** of optical networks, which combine monitoring data with analytical and machine learning models to predict QoT evolution and enable proactive optimization.

The predictive value of any DT depends critically on the fidelity of its input parameters [41, 153]. If these parameters are stale or biased, actions that appear beneficial in simulation may in fact degrade QoT when applied to the live network. This risk forces operators to adopt larger safety margins, which in turn reduces spectral efficiency and leads to suboptimal resource utilization [102]. While advances in monitoring hardware have enabled access to richer telemetry, several key quantities remain difficult to observe directly in operational environments. These include span- and section-level insertion losses that govern power evolution including SRS-induced power tilt, amplifier gain and noise-figure spectra that determine ASE accumulation and channel-to-channel OSNR tilt, and compact end-to-end offsets that capture residual penalties from filtering and transponder implementation. Errors in these parameters propagate through GN-type estimators and can bias the recommended launch powers, modulation formats, and spectrum allocations [79].

Accurate refinement of such hidden or partially monitored parameters is therefore essential to unlock the full predictive potential of analytical DTs and to ensure their safe application in live networks. We next introduce the monitoring elements in optical networks.

1.2.2.2. Monitoring in Optical Networks

In contemporary commercial optical networks, monitoring plays a fundamental role in establishing an accurate DT to ensure reliable operation and service quality. It is indispensable for root-cause analysis, fault detection and localization, and for enabling accurate QoT prediction and optimization. Effective monitoring ensures that critical components, such as transceivers, receivers, WSSes, optical amplifiers, and fibers, remain within their expected operational parameters and are free from performance anomalies.

Accurate impairment modeling and reliable operation in optical networks require continuous monitoring of key observables at multiple levels. In particular:

- **Per-channel power** refers to the optical powers for each WDM channel, which are always monitored at input/output of the amplifier to maintain spectral balance across the grid. Small deviations from the optimal power profile directly impact

OSNR and nonlinear interference, resulting in QoT degradation.

- **Fiber insertion loss** corresponds to localized losses at connectors, splices, or multiplexing elements that often deviate from nominal values due to aging, repairs, or contamination. When combined with per-channel power monitoring at the amplifier output, the per-channel launch power entering the fiber can be calculated. Tracking these losses enables accurate modeling of fiber nonlinear effects, hence accurate per-channel QoT prediction and optimization, and facilitates the localization of anomalous degradations.
- **Amplifier input/output power** denotes the total optical powers measured at amplifier ports, ensuring amplifiers operate within their designed dynamic range. These values are crucial for verifying link budgets, detecting power drifts, and identifying spectral tilt or saturation effects.
- **Longitudinal power profile evolution** captures how channel powers evolve along fiber spans under the influence of attenuation, Raman scattering, and amplifier gain. Monitoring the profile provides span-level visibility, improves nonlinear impairment modeling, and supports accurate power optimization.
- **Amplifier gain and noise figure spectra** characterize the frequency-dependent amplification and ASE noise of each amplifier. These spectra define OSNR accumulation and spectral tilt, making their monitoring vital for accurate per-channel QoT prediction and optimization.
- **Bit Error Rate (BER)** is measured at the receiver as the fraction of erroneous bits relative to transmitted bits. It provides a direct ground-truth indicator of service quality, with pre-FEC BER revealing early degradations and post-FEC BER confirming service-level reliability.
- **WSS filtering penalties** include cumulative effects such as WSS filtering, passband narrowing, and ripple from cascaded elements. These penalties must be tracked to capture degradations not visible at the component level and to quantify the overall margin reduction along reconfigurable paths.
- **Transponder back-to-back performance** defines the intrinsic quality achievable without a transmission link, isolating equipment limitations of DSP and optical front-ends. This baseline is essential to correctly distinguish link-induced degradations from transponder-induced impairments.

Together, these observables provide multi-level visibility into the physical layer, allowing accurate QoT prediction, anomaly detection, and closed-loop optimization, thereby re-

ducing design margins and enabling efficient and scalable automation of modern optical networks.

Monitoring techniques can be broadly categorized into hardware-based and software-based approaches. As illustrated in Fig. 1.3, hardware-based monitoring relies on dedicated optical or optoelectronic devices to directly measure physical-layer parameters, such as per-channel power, total input/output power, BER, etc. In contrast, software-based monitoring exploits coherent receiver DSP and machine-learning algorithms to infer or refine parameters such as fiber insertion loss, amplifier gain and NF, filtering penalty, transponder B2B limitation, longitudinal power evolution, etc. that are difficult or costly to observe directly due to limitations in hardware accessibility, sensitivity, or deployment cost.

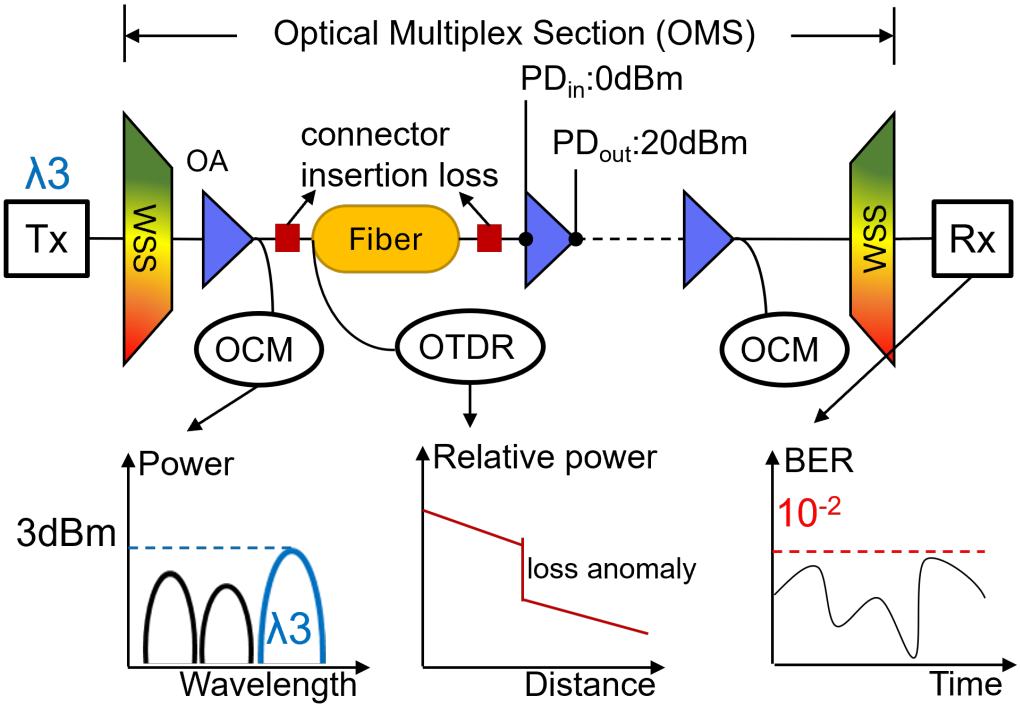


Figure 1.3: Hardware-based monitoring techniques.

Hardware-based monitoring techniques

1. **Photodiode (PD):** Converts incident light into electrical current via the photoelectric effect in a semiconductor. PDs are widely integrated into transceivers, receivers, WSSes, optical amplifiers, and stand-alone instruments. In optical amplifiers, PDs are typically positioned at both input and output ports to measure total optical power. The ratio of output to input power provides an estimate of amplifier gain, which can then be monitored and configured.

2. **Optical Spectrum Analyzer (OSA):** Separates light into its constituent wavelengths using a diffraction grating or tunable filter, with the power at each wavelength measured by a detector array. OSAs provide high-resolution, high-sensitivity measurements of signal and noise power, enabling accurate OSNR monitoring. However, due to their high cost and bulk, OSAs are primarily used in commissioning, troubleshooting, or laboratory environments rather than for real-time service monitoring.

3. **Optical Channel Monitor (OCM):** Demultiplexes WDM channels using an arrayed waveguide grating or optical filter and measures the per-channel power using PDs. OCMs are less sensitive than OSAs and cannot measure noise power directly, but they are more cost-effective and thus widely deployed for real-time channel power monitoring and equalization without disrupting live traffic. In many commercial deployments, only the output spectra of the first and last amplifiers in each optical multiplex section (OMS) are monitored, though some networks also monitor all amplifier outputs.

4. **Optical Time Domain Reflectometer (OTDR):** Launches short optical pulses (near the optical transmission band) into the fiber and measures backscattered and reflected light as a function of time. The time axis is converted into distance to localize splices, connectors, bends, breaks, and attenuation points. OTDRs are widely used for fiber installation, commissioning, and troubleshooting, offering high spatial resolution but requiring out-of-service measurements with dedicated equipment and test signals.

Software-based monitoring techniques

1. **Conventional Coherent Receiver Monitoring:** Coherent receivers leverage DSP algorithms to monitor transmission parameters in service. The pre-Forward Error Correction (pre-FEC) BER is calculated either by comparing the received sequence with a known reference or through error statistics derived from the FEC process. PDL is estimated from received power variations relative to polarization states. CD is extracted from phase shifts across subcarriers or symbols, while DSP simultaneously compensates accumulated dispersion in real time.

2. **Power Profile Estimation (PPE):** Employs receiver-side DSP to estimate the longitudinal power profile of an optical link in service [112–114]. By exploiting chromatic-dispersion-induced and nonlinear phase-rotation effects, PPE reconstructs distributed power evolution without requiring out-of-service hardware such as OTDR.

While its spatial resolution is lower than OTDR, PPE provides continuous real-time fault localization and performance monitoring without service disruption.

3. **Input Refinement (IR):** Combines hardware-monitored parameters (e.g., OCM- and PD-based data) with known fiber characteristics from databases (length, wavelength-dependent loss, Raman coefficients, etc.), and uses analytical models or machine-learning algorithms (i.e., gradient descent) to refine other unknown parameters such as fiber insertion loss, amplifier gain and NF, filtering penalty, transponder B2B limitation.

   Several input parameter refinement (IR) techniques have been proposed to enhance the accuracy of DT models in optical networks. One direction combines analytical GN modeling with gradient-descent–based machine learning to refine uncertain EDFA noise figures and output power profiles, thereby reducing the reliance on large design margins [119]. Early approaches exploited measured OSNR values from OSAs to estimate insertion losses and amplifier noise figures through Bayesian optimization [3] or joint estimation of fiber and amplifier parameters [15]. However, their dependence on OSNR measurements restricted applicability to commissioning phases only. More advanced IR methods incorporated Raman amplifiers [161] or combined neural-network–based EDFA models [87], improving accuracy but still requiring non-standard observability. Other works exploited OCMs to refine insertion losses and amplifier gain spectra at the OMS level [85], while studies assuming per-span OCMs and ripple-free gain spectra [25] demonstrated high accuracy in controlled setups but relied on extra costly hardware or calibration assumptions. To increase robustness under heterogeneous and partially loaded conditions, data-driven approaches have been proposed that refine signal power measurements and optimize amplifier and frequency-dependent biases [56]. Most recently, IR has been extended with bias fitting over multiple snapshots to absorb unmodeled impairments, such as filtering penalties, thereby improving DT accuracy throughout the network life cycle [4].

   To overcome these limitations, this thesis proposes and validates (using simulations and experiments) four novel IR techniques under different application scenarios and monitoring constraints:

   - *Passive Inputs Refinement (PIR)*: PIR refines insertion losses and amplifier gain spectra by applying gradient descent on a single network snapshot. It achieves sub-dB GSNR accuracy in both C- and C+L-band systems, while remaining robust to heterogeneous spans and even to aging-induced splice un-

certainties [151]. However, its accuracy is limited to the OMS level, providing no span-level sensitivity, which constrains its ability to detect or localize anomalous insertion losses.

- *Active Inputs Refinement (AIR)*: AIR introduces active probing by slightly perturbing amplifier gains to induce measurable SRS variations that can be monitored by OCM at the end of OMS. This enables accurate per-span loss estimation and anomaly localization, validated on a European-scale network topology and in laboratory experiments. AIR significantly enhances insertion-loss estimation accuracy and improves GSNR margins during QoT re-optimization compared to PIR techniques. Its limitation lies in the need for sufficiently strong SRS signatures, typically present under full-load conditions, and its trade-off is a temporary but predictable SNR variation during probing [153].

- *Incremental-learning Inputs Refinement (IIR)*: IIR leverages multiple network snapshots (states) collected during successive re-optimization steps and applies gradient descent to progressively refine insertion losses, amplifier gain spectra, and end-to-end penalties, including WSS filtering and transponder back-to-back noise. By exploiting snapshot diversity, IIR avoids overfitting and continuously improves DT fidelity as the network evolves. Both simulations and experimental validations on C-band mesh networks confirm that IIR achieves sub-dB accuracy of insertion loss estimation, enabling highly reliable closed-loop QoT optimization in partially loaded and dynamically reconfigured networks [156].

- *Hybrid IR + PPE*: By combining IR with Power Profile Estimation (PPE), this approach provides absolute calibration of longitudinal power profiles and insertion losses, enabling accurate detection and localization of anomalous connector losses even under sparse monitoring. This hybridization bridges relative refinement (from IR) with absolute calibration (from PPE), yielding highly accurate parameter recovery and enhancing the robustness of QoT modeling [152].

Together, these four techniques form a complementary toolkit: PIR leverages a single snapshot to provide OMS-level accuracy, AIR extends visibility to the span level, IIR exploits multiple snapshots to enable incremental refinement of insertion losses and amplifier gain spectra during network re-optimization, and the Hybrid IR+PPE integrates IR with PPE to deliver accurate absolute loss estimation and longitudinal power estimation. Collectively, they cover different layers of granularity and operational scenarios, supporting the construction of accurate and robust DTs.

Table 1.1 summarizes several existing IR techniques.

Table 1.1: Input parameter refinement techniques.

Ref. (band)	Main inputs and assumptions	Estimated Parameters
[119] (C)	Measured SNR	power spectrum, amplifier noise figure spectrum
[3] (C)	Measured OSNR at OMS output	Insertion loss, amplifier noise figure spectrum
[85] (C)	Measured output power spectrum at OMS	Insertion loss, amplifier gain spectrum
[151] (C+L) In Chapter 3	Measured output power spectrum at OMS	Insertion loss, amplifier gain spectrum
[87] (C)	Measured output power spectrum at OMS, trained EDFA model	Insertion loss, amplifier gain spectrum
[150] (C, C+L) In Chapter 4	Measured output power spectrum at OMS, fully ASE-loaded system, calibrated amplifier gain spectrum, active amplifier gain adjustment	Insertion loss
[56] (C)	Measured output power spectrum at OMS	Output power spectrum excluding ASE noise
[15] (C)	Measured OSNR at OMS output, measured OMS output power spectrum, homogeneous rippled gain spectrum	Fiber parameters, insertion loss, average amplifier noise figure
[163] (C+L)	Measured output power spectrum at each span, ripple-less gain spectrum	Insertion loss
[161] (C)	Measured input/output power spectrum at span with Raman amplifier	Output power spectrum with Raman amplifier

Continued on next page

Ref. (band)	Main inputs and assumptions	Estimated Parameters
[152] (C) In Chapter 6	Measured output power spectrum at OMS, symbols received at coherent receiver	Insertion loss, amplifier gain spectrum, absolute longitudinal power estimation
[25] (C+L)	Measured output power spectrum at each span, fully ASE-loaded system	Insertion and splice loss
[4] (C)	Multi snapshots of measured output power spectrum at each OMS and service BER	WSS penalty offset
[156] (C) In Chapter 5	Multi snapshots of measured output power spectrum at each OMS and service BER	Insertion loss, amplifier gain spectrum, E2E offset noise

1.2.2.3. Network Automation

Software-defined networking (SDN) has been widely investigated as an enabler of automation and disaggregation in optical transport. SDN controllers have traditionally relied on QoT estimators to enforce transmission parameters on transponders and ROADMs for lightpath provisioning and restoration, although further improvements are needed to cope with the complexity of optical control and data planes [6, 11, 33]. SDN must also integrate amplifier control to ensure scalability and performance. Since full multi-vendor interoperability at the optical line level is still impractical, partially disaggregated solutions have emerged in which proprietary line systems are managed by vendor-specific controllers, while open packet-optical nodes with pluggable transceivers are directly integrated into the SDN framework. To address these challenges, prior works have leveraged NETCONF/YANG and OpenConfig models to configure and monitor transponders and ROADMs [27, 110, 120, 133], demonstrated disaggregated path protection [68], sliceable transponders [89], and telemetry applications [97], with Open Network Operating System (ONOS) often serving as the SDN controller for discovery and topology management [18]. From the perspective of physical-layer modeling, the developed GNPy tool implements an AWGN-based QoT estimator and has been validated in multiple testbeds as a reliable candidate for a digital twin of the physical layer [26, 42, 135]. Its integration with ONOS has enabled the first demonstrations of SDN-driven orchestration using digital twins in both linear [68] and partially disaggregated topologies [14].

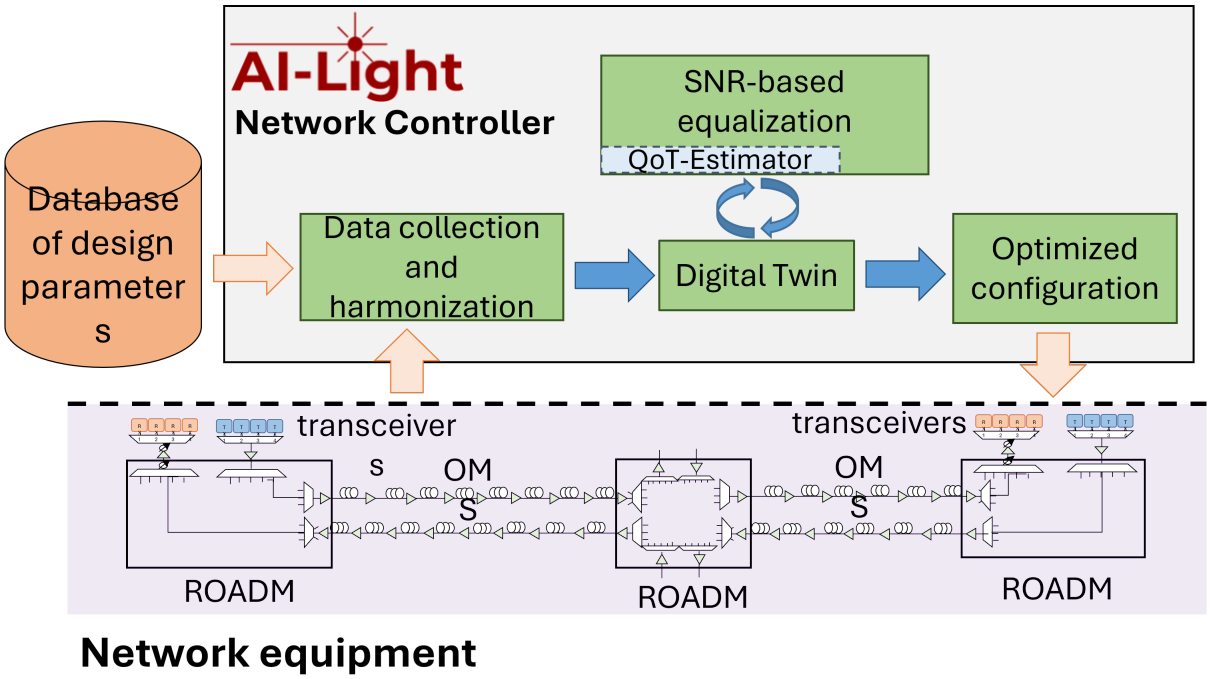


Figure 1.4: AI-Light SDN framework.

In this thesis, the AI-Light framework is adopted as an SDN-enabled automation architecture integrating a physical-layer digital twin for QoT estimation and channel-power optimization. This framework was developed by my colleagues and presented in [42]. AI-Light leverages advanced monitoring techniques to build a DT, applies QoT optimization algorithms [101, 115] to compute the optimum channel powers, and automatically pushes the configuration into the network, thereby enabling resilient and QoT-aware operation in dynamically loaded optical systems. An extended version of this line of research explores the use of LLMs as local AI-Agents, where fine-tuned LLMs collaborate with SDN controllers and digital twins to automate lifecycle management tasks such as network design, deployment, re-optimization, and troubleshooting, achieving intent interpretation, API calling, and high-accuracy decision-making [126]. These developments highlight the trajectory from SDN-based, digital twin–assisted automation toward AI-enhanced optical networks, where digital twins remain the central enabler for interpretable, physics-grounded control.

Together, these advances underline the critical role of combining analytical models with advanced monitoring technologies to construct accurate and trustworthy DTs. Such integration not only grounds automation in physical reality but also enables scalable and robust QoT-aware control. In particular, automating the ingestion of real-time monitored parameters into analytical formulations and optimization algorithms using SDN platform provides the foundation for large-capacity, resilient, and fully automated optical networks.

1.2.3. Data Center Interconnects

The shift from monolithic mega-data centers to multi-data-center regions, where multiple smaller facilities within metro distances are interconnected has introduced new design challenges for Data Center Interconnects (DCIs). This architectural evolution is motivated by siting constraints in dense urban areas and the need for improved resilience against large-scale failures [32]. Regional DCIs must balance requirements of latency, availability, and cost, but traditional hub-and-spoke topologies, while simple and cost-efficient, often limit flexibility in both site placement and inter-DC latency. To overcome these limitations, novel designs such as the *Iris* [32] optical-circuit-switched architecture have been proposed, leveraging all-optical switching and abundant metro fiber to enable more distributed topologies with manageable cost and complexity. At the same time, hyperscale operators have begun to deploy *low-margin optical networking* strategies, which rely on cost- and power-efficient pluggables operated closer to physical-layer limits but supported by open line systems and SDN automation to ensure cloud-scale availability [45].

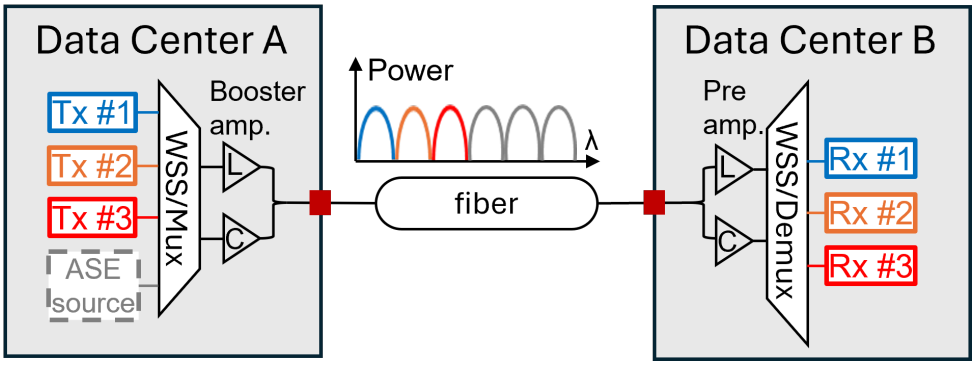


Figure 1.5: Topology of DCI networks.

Industry standardization has focused on coherent pluggable modules as a practical solution for scaling DCI capacity. The OIF's *400ZR Implementation Agreement* specifies interoperable 400 Gb/s coherent interfaces for point-to-point DWDM links up to metro reach [93], as shown in Fig. 1.5, while the more recent *800ZR specification* extends these principles to 800 Gb/s per wavelength with low power consumption and switch/router-friendly form factors [94]. Complementary experimental work has validated open-source GN-model-based QoT estimators across multi-vendor testbeds, demonstrating the feasibility of vendor-agnostic performance prediction for disaggregated DCI networks [43]. Comprehensive surveys further emphasize that DCIs differ fundamentally from carrier optical transport in terms of simplicity, protocol stack, and scale. They show that hyperscale DCIs are increasingly built on three technological pillars: embedded high-

performance coherent transponders, pluggable coherent optics such as ZR/ZR+, and direct-detection PAM4 for very short spans. Future scaling will require innovations such as multi-band transmission, hollow-core fibers, and space-division multiplexing, together with open and disaggregated control planes to achieve automation and interoperability at hyperscale [145].

In this thesis, we investigate the capacity scaling limits of short-reach DCI networks enabled by three families of coherent transponders: standardized 800G ZR pluggables, extended-reach ZR+ modules, and high-performance (HP) transponders. Using experimentally characterized load-dependent amplifier gain and noise spectra from a metro-scale testbed, we model system capacity under varying span losses, WDM configurations, and spectrum expansion scenarios. Our study considers both passive multiplexer-based systems and WSS–based architectures with ASE loading, capturing practical deployment trade-offs in terms of amplifier stability, channel loading, and operational complexity.

Overall, this thesis provides a comparative assessment of the trade-offs between cost-efficient ZR transponders and more capable yet expensive high-performance (HP) transponders, offering insights into how hyperscale operators can optimize DCI design choices as traffic demand accelerates and multi-band optical transmission emerges as a practical necessity.

1.3. Contributions and Thesis Outline

1.3.1. Contributions

This thesis addresses the challenge of achieving accurate, automated, and adaptive Quality-of-Transmission (QoT) estimation and optimization in optical networks. The research advances both the theoretical understanding and practical implementation of digital-twin-enabled frameworks for network performance management. It builds upon extensive experimental and simulation-based investigations that progressively improve the modeling accuracy, observability, and controllability of the optical layer.

The presented contributions span from experimental studies on QoT degradation and its mitigation through power re-optimization, to advanced parameter-refinement techniques that enhance digital-twin fidelity, and finally to benchmarking next-generation transponder technologies. Together, these works establish a unified methodology that connects physical-layer monitoring, parameter estimation, and QoT-aware optimization through Software-Defined Networking (SDN) automation.

Experimental investigation of QoT Degradation and Recovery through Power Re-optimization

The first contribution is an experimental investigation of the QoT degradation affecting established services when new services are provisioned under the practical "set-and-forget" service allocation strategy. This work initially demonstrates that such a service allocation strategy significantly degrades existing services upon network reconfiguration due to the induced load-dependent impairments. To mitigate these effects, we classify and validate static and dynamic power re-optimization strategies, showing that both power re-optimization strategies can substantially recover QoT. In this work, I:

- Classified state-of-the-art power optimization methods into: (i) static approaches, power setting is based on end-of-life parameter settings, and (ii) dynamic approaches, leveraging real-time monitoring data to set power with feedback.
- Implemented and optimized the algorithms within a Software-Defined Networking (SDN) control plane (Python-based), enabling automated integration with experimental procedures.
- Designed and executed automated experiments using SDN in a realistic multi-node, multi-OMS mesh testbed with commercial-grade equipment.
- Quantified the substantial QoT degradation of existing services following "set-and-forget" strategy , and the QoT recovery enabled by both static and dynamic re-optimization strategies to maintain service performance upon network reconfiguration.
- Published these studies as first author in IEEE/Optica Journal of Optical Communications and Networking [150].

Development of Passive Input Refinement (PIR) in C+L Systems

The second contribution is the extension of the Passive Input Refinement (PIR) method from C-band to C+L systems, leveraging stronger stimulated Raman scattering (SRS) effects in C+L-band systems. By refining unknown parameters such as fiber insertion losses and amplifier gain spectra as input of the digital twin, the method achieves more accurate digital twin, enabling more accurate QoT estimation, even under heterogeneous spans and aging conditions. In this work, I:

- Developed the extended PIR algorithm extended for C+L systems to leverage stronger SRS effect.

- Validated by simulations the accuracy of QoT prediction enabled by a digital twin with the refined input parameters in three representative scenarios: (i) a single C+L OMS system with homogeneous spans, showing significant improvements in accuracy of OSNR, nonlinear SNR, and GSNR estimation over baseline method; (ii) a cascade of ten OMSes with heterogeneous spans, where the method improved end-to-end SNR estimation; (iii) an aging scenario with uncertain fiber attenuation, where the method remained robust by mapping excess loss into refined insertion losses.
- Published these findings as first author in Optical Fiber Communications Conference and Exhibition (OFC) 2023 [151].

Development of Active Input Refinement (AIR)

The third contribution is the development of an advanced input refinement technique called *Active Inputs Refinement (AIR)*. This method leverages the variation of the SRS effect by actively perturbing amplifier gain, enabling span-level estimation of fiber insertion loss. Such fine-grained visibility allows anomaly detection and localization at the span level, surpassing the OMS-level sensitivity of the PIR method. By establishing a more accurate digital twin through refined parameters, AIR delivers superior estimation accuracy, which in turn supports superior estimation accuracy and enables more reliable and efficient QoT optimization. In this work, I:

- Proposed and implemented the AIR algorithm, exploiting SRS variations induced by controlled amplifier gain adjustments.
- Integrated the method into an SDN-based control plane for automated management and seamless experimental operation.
- Designed and conducted experiments in a point-to-point testbed comprising cascaded OMSes with heterogeneous spans using commercial equipment.
- Validated the approach in both simulations and experiments in both full-load C and C+L systems, achieving accurate span-level insertion loss estimation, enabling reliable detection and localization of anomalous insertion losses, and enhancing digital twin fidelity for more effective QoT optimization.
- Investigated the transient and predictive impact of QoT variations in live services induced by active amplifier gain adjustments, and applied PIR to predict these variations, demonstrating feasibility and reliability in real optical networks.
- Published at Optical Fiber Communications Conference and Exhibition (OFC)

2024 [154], with an extended journal paper accepted in IEEE/Optica Journal of Optical Communications and Networking [153], and a filed patent.

Development of Incremental Inputs Refinement (IIR) for Multi-Snapshot Parameter Refinement

The fourth contribution is the development of another advanced input refinement technique, termed *Incremental Inputs Refinement (IIR)*. Unlike previous approaches, IIR leverages multiple network snapshots to progressively refine uncertain physical parameters including service end-to-end offset noise, thereby enhancing digital twin accuracy without service interruption in partial-load networks where SRS may be not evident. When embedded into a closed-loop optimization framework, IIR enables near-ideal QoT optimization performance as knowing all information. Specifically, I:

- Proposed and developed the IIR algorithm, exploiting successive network snapshots to incrementally refine digital twin parameters.
- Integrated the method into an SDN-based control plane for automated management and seamless experimental operation.
- Designed and executed experiments in a realistic partial-load testbed with heterogeneous OMSes using commercial equipement.
- Demonstrated that IIR achieves accurate QoT prediction in both simulation and experiment.
- Integrated the IIR algorithm into a self-driven QoT optimization loop within the SDN control plane, enabling autonomous parameter refinement and power adjustment, achieving optimization performance nearly identical to the ideal case using ground-truth information.
- Published at Optical Fiber Communications Conference and Exhibition (OFC) 2024 [156], with an extended journal paper submitted in IEEE/Optica Journal of Optical Communications and Networking (under peer review), and a filed patent.

Development of Hybrid IR+PPE Framework for Joint Parameter Refinement and QoT Optimization

The fifth contribution is the integration of Input Refinement (IR) with Power Profile Estimation (PPE), termed *hybrid IR+PPE*, into a unified framework that jointly improves insertion loss estimation, longitudinal power profiling, and QoT prediction accuracy. This

combined approach surpasses the accuracy of either technique alone, enhances the accuracy of input refinement and longitudinal power profile estimation, anomaly detection, and strengthens QoT optimization. Specifically, I:

- Proposed and developed the framework of integration of IR and PPE technique, achieving accurate estimation for fiber insertion loss, amplifier gain spectrum, longitudinal power profile, and QoT.
- Implemented the method within the SDN control plane for automated network management.
- Designed and executed experiments in a realistic partial-load testbed with heterogeneous OMSes using commercial equipment.
- Demonstrated experimentally that the integrated approach achieves more accurate parameter refinement and higher-performance QoT optimization.
- Published at European Conference on Optical Communication (ECOC) 2024 [152].

Benchmarking of ZR, ZR+, and HP Transponders for Robust and Automated Design and Operation of DCI Networks

The sixth contribution is the benchmarking of 800G ZR, ZR+, and High-Performance (HP) transponders for short-reach DCI networks under varying bandwidth and span loss scenarios. We identify the key design and operation features such as the selection of transponder types, multiplexing schemes, and the service allocation strategies to enhance the robustness and automation for short-reach DCI networks. In this work, I:

- Validated, through simulations calibrated with experimentally collected amplifier gain and noise figure (NF) spectra compliant with OIF specifications, the capacity scalability under varying span losses and total bandwidths across different transponder types, multiplexing schemes, and service allocation strategies, thereby enhancing the robustness and automation of DCI network design.
- Identified optimal ZR loading strategies in terms of channel order and number, achieving robust capacity gains compared to worst-case loading scenarios that can induce significant network margin degradation.
- Published at European Conference on Optical Communication (ECOC) 2025 [155].

1.3.2. Thesis Outline

The remainder of this thesis is organized into chapters that progressively address the challenges of sustaining service quality while enabling robustness and automation in optical networks. Chapter 2 establishes the experimental foundation by investigating QoT degradation under the practical "set-and-forget" service allocation strategy and evaluating the effectiveness of power re-optimization techniques under realistic monitoring conditions. Building on this foundation, Chapters 3–6 introduce novel monitoring and refinement methods that exploit different levels of available network data—respectively PIR, AIR, IIR, and the integration of IR with PPE. These methods enhance parameter visibility, improve digital twin fidelity, and enable accurate QoT prediction and optimization in realistic mesh networks. Chapter 7 shifts the focus to short-reach DCI networks, emphasizing the benchmarking of transponder design features and service allocation strategies rather than monitoring. Finally, Chapter 8 synthesizes the contributions, discusses their broader implications for network automation and scalability, and outlines promising directions for future research.

Chapter 2 presents an experimental investigation into the QoT degradation observed in mesh optical networks operating under the practical "set-and-forget" service allocation strategy. To address this degradation, we classify power re-optimiza-tion approaches into two categories: (i) static, end-of-life strategies and (ii) real-time, dynamic strategies. Their effectiveness in recovering QoT is validated and compared in a mesh testbed using commercial equipment. The results demonstrate that incremental service loading can impair the QoT of already established connections, while the proposed re-optimization strategies efficiently mitigate these impairments. This highlights the critical role of adaptive power management in sustaining service quality in realistic network environments.

Chapter 3 introduces the extension of the previously developed *Passive Inputs Refinement (PIR)* technique from C-band to C+L-band systems, where SRS effects become more pronounced. By refining uncertain parameters such as fiber insertion losses and amplifier gain spectra, the proposed method achieves higher accuracy in QoT prediction. The approach is validated by simulations in heterogeneous and aging network scenarios, demonstrating its robustness and outperforming baseline assumptions. This work highlights the importance of accurate parameter refinement to enable reliable and accurate digital twin in multi-band optical networks.

Chapter 4 presents the development of an advanced refinement technique termed *Active Inputs Refinement (AIR)*. This method actively perturbs amplifier gain to exploit SRS variations, thereby enabling span-level estimation of fiber insertion loss. Such fine-grained

visibility allows anomaly detection and localization at the span level, surpassing the OMS-level sensitivity of PIR. By refining key parameters, AIR establishes a more accurate digital twin, which enhances QoT prediction accuracy and supports more effective and reliable QoT optimization. The proposed method is validated by (i) experiments in a point-to-point C-band testbed with multiple heterogeneous OMSes and (ii) simulations based on a realistic European network topology with C and C+L-band, demonstrating the feasibility and reliability of the approach.

Chapter 5 introduces *Incremental Inputs Refinement (IIR)*, a refinement method that leverages successive network snapshots to incrementally refine uncertain physical parameters under realistic monitoring conditions. Unlike single-shot techniques, IIR mitigates the impact of overfitting, enabling more accurate digital twin modeling thanks to progressive parameters refinement. On the one hand, the method can run offline with collected snapshots without interrupting live services, on the other hand, IIR can be embedded into a closed-loop optimization framework for self-driven operation. The IIR method is demonstrated by: (i) simulations using experimental data, and (ii) experiments in a mesh network testbed with heterogeneous spans and OMSes with partial-load channels, demonstrating that IIR enables accurate QoT prediction thanks to accurate refined parameters, while in turn enhancing QoT optimization performance, approaching the ideal case based on ground-truth information. This chapter underscores the potential of incremental refinement to enable robust, autonomous, high-fidelity digital twins for network optimization.

Chapter 6 presents the integration of Inputs Refinement (IR) with Power Profile Estimation (PPE),termed *hybrid IR+PPE*, to advance monitoring accuracy and digital twin fidelity in optical networks. While PPE provides relative longitudinal power profiles and IR refines insertion losses and amplifier gain spectra, their combination enables accurate per-span insertion loss estimation, amplifier gain spectra, power profile reconstruction, and anomaly detection without active network probing. Experimental validation in a multi-OMS mesh testbed demonstrates that IR+PPE substantially improves insertion loss estimation, enables precise localization of anomalous connector losses, and enhances QoT prediction accuracy. When these refined parameters are embedded within a digital twin, the resulting model supports more effective QoT optimization, yielding measurable gains in service SNR, network margin, and overall network robustness. This chapter underscores the importance of integrating complementary monitoring techniques to establish highly accurate and reliable digital twins for future optical networks.

Chapter 7 evaluates the design features and performance of different classes of transponders for DCI networks, including 800G ZR, ZR+, and high-performance (HP) solutions.

The study considers varying span losses, bandwidth expansion, and service loading strategies in both passive multiplexer- and wavelength-selective-switch-based systems. Results show that advanced transponders and optimized service allocation significantly improve achievable capacity, demonstrating the importance of careful design choices in DCI networks. This chapter provides actionable insights for the deployment and scaling of short-reach high-capacity and robust optical interconnects.

Chapter 8 concludes the contributions of this thesis by discussing how advanced input refinement techniques and optimized power and resource management strategies jointly enable more accurate and reliable digital twins for large-capacity, robust and automated optical networks. The chapter highlights the role of refined monitoring and modeling in bridging the gap between theoretical physical-layer understanding and practical network operation. Finally, it reflects on broader implications for automation, robustness, and scalability in future optical networks, and outlines promising directions for extending this work, including multi-band operation, AI-driven refinement, and real-time closed-loop optimization at scale.

2 | Experimental Impact of Power Re-Optimization in a Mesh Network

2.1. Abstract

We experimentally observe the SNR degradation of previously established services induced by loading new services in a network, and mitigate this degradation by periodic power re-optimization via 2 different strategies: 1) a static strategy based on end-of-life parameters, and 2) a dynamic strategy based on real-time monitoring to the current state of the network. We use a mesh network testbed of 4 nodes and 5 links with commercial equipment only. We observe up to 3.4 dB SNR degradation on the previously established services due to the loading of new services. Then we demonstrate an improvement of up to 3.2 dB in the network margin achieved by applying our proposed power re-optimization strategy.

2.2. Introduction

With the advent of the globalized information age, people's reliance on Internet services has increased dramatically. Optical fiber networks are used as Internet backbone, and have evolved vastly over the past decades through techniques such as Wavelength Division Multiplexing (WDM), advanced optical digital signal processing, improved fiber design and manufacturing, advances in optical amplifiers, etc. Recently, with the emergence of 5G (and soon 6G) services, new communication patterns driven by services in new areas as Internet of Thing (IoT), smart homes, unmanned smart driving, etc. [23] are appearing in backbone networks, and they will bring new practical challenges to current optical networks. New more robust and larger-capacity optical networks are urgently needed to meet growing needs of these new services.

High Quality of Transmission (QoT), such as low Bit Error Rate (BER) or high Signal-to-

Noise Ratio (SNR), of services in optical networks is key to ensure large capacity and robustness of services in an optical network. Services in optical networks co-propagate, over different wavelengths, with other services through one or several links or Optical Multiplex Sections (OMSes); hence, services' SNRs can be impacted by many load-dependent physical effects such as Kerr effect (i.e. Self-Phase Modulation (SPM), Cross-Phase Modulation (XPM), Four-Wave Mixing (FWM)), Stimulated Raman Scattering (SRS), Wavelength Dependent Loss (WDL), and load-dependent gain spectrum of Erbium-Doped Fiber Amplifiers' (EDFA), thus the Amplified Spontaneous Emission (ASE) noise. These load-dependent effects make SNR of established services vary upon load changes, e.g. upon new services establishment or dropping, or simply upon power variations of the established services. SNR variations induced by load change may cause the service QoT to decrease below the SNR that corresponds to the Forward Error Correction (FEC) threshold, thereby causing outages.

To avoid service disruption in the cases described above, network designers are posed with the challenge to allocate enough design margins at network design time. In fact, reducing overall design margins, while making sure that the SNR margin of the service closest to FEC limit is maximized, can translate into increasing operation margins, which makes networks more robust to aging (e.g., due to fiber attenuation increase caused by fiber splices), or increase the capacity of optical networks, longer networks' life, and less deployment cost (CAPEX) or total cost of ownership during networks' life [102].

When accomodating new services into the network, certain operators prefer using the so-called "set and forget" operation mode [24, 71, 99] to set their powers. In "set and forget" mode, powers of new services are set using a pre-defined rule (e.g., powers are optimized for a fully loaded network); while, the powers of previously established services are not touched, thereby their powers, hence their SNRs, are left to drift without being adjusted to the new network state.

To maintain services running at their optimum SNR, powers of all services, both previous and new, can be re-optimized with different strategies upon any network layer change. Power re-optimization strategy (or "power re-equalization") consists of allocating power to each service by properly actuating the per-channel attenuation of the Wavelength Selective Switch (WSS) at the beginning of each OMS [48, 107]. Through power re-optimization, the SNR of the worst service can be maintained at its optimum level, which helps to decrease design margin and increase operation margins. However, it has also to be taken into account that, providing a reliable dynamic solution is challenging as the transient of the devices has to be kept under control, also the scalability of the solution as well as the time required by the devices to converge to the new configuration. Some of these issues

are, for instance, addressed in [162].

This paper is an extended version of our ECOC 2022 paper [149]. The aim of this paper is two-fold. First, we experimentally quantify the SNR degradation of previously established services as new services are established in a realistic mesh network. Second, we experimentally quantify and compare the network margin improvement of both previously established and new services when using two existing power re-optimization strategies. In this experiment work, our mesh network testbed consists of 4 nodes and 5 OMSes with heterogeneous span type and length built with only commercial equipment that would be deployed at operators', and up to 292 services are established. Our experiment demonstate SNR variations due to load change of several dBs, which can be fully recovered through proper power re-optimization strategies. We also show good match between the predicted SNR (that we obtained using a digital twin) and the measured SNR after power re-optimization, which ensures good reliability of applying power re-optimization strategies.

The remainder of the paper is structured as follows. In Section 2, we introduce two power optimization strategies to mitigate SNR degradation due to loading new services in the network. In Section 3, we introduce the network loading scenario where procedures of services' loading and power re-optimization are described. In Section 4, we introduce our 5-OMS mesh network testbed. In Section 5, we experimentally evaluate the SNR degradation induced by loading new services, and the SNR improvement by applying power re-optimization strategies, also we show the digital twin validation at the end.

2.3. Power Optimization Strategies

In this section, we define two different power optimization strategies, 1) a static End-of-Life design strategy (static strategy) and 2) a dynamic real-time strategy (dynamic strategy), to mitigate SNR degradation of previously established services caused by loading new services in the network. These power optimization techniques are implemented by setting the per-channel launch output power at the first ("booster") amplifier of each OMS in a network.

2.3.1. Static End-of-life (EoL) Design Strategy

The first strategy is based on a "static" End-of-Life (EoL) design strategy, which consists in computing the launch power based on EoL assumptions, therefore, it never changes during network lifetime. To set the EoL launch power, only "static" parameters are used (see 2.1). These parameters can be obtained at the design stage or at the initial

commissioning of the network at Beginning of Life (BoL), namely, fiber length, fiber type, span loss, and estimated connector loss. This static EoL strategy sets the launch power based on the Local-Optimum Global-Optimum (LOGO) formula [101], that assumes Full Spectral Load (FSL). LOGO aims at optimizing SNR of the worst channel at OMS level by providing a flat power allocation (PLOGO) as input power into the fiber for each span by means of the analytical formula:

$$P_{\mathrm{LOGO}} = \sqrt[3]{\frac{P_{\mathrm{ASE}}}{2\eta}} \tag{2.1}$$

P_{LOGO} is derived under the assumptions of flat power spectrum, flat amplifier gain spectrum, flat fiber attenuation, and the SRS effect is not taken into account. P_{ASE} is the ASE noise power generated by the EDFA and η is the nonlinear efficiency evaluated under FSL assumption. Since static, BoL parameters are used for this power re-optimization throughout the network life, until EoL, this strategy is suboptimal.

2.3.2. Dynamic Real-time Strategy

The "dynamic" real-time strategy also aims at optimizing the SNR of the worst channel at each OMS, but in a dynamic fashion. The optimal launch power provided by the dynamic strategy is calculated based on Gaussian noise (GN) model [101, 117] considering wavelength-dependent gain spectrum, wavelength dependent fiber attenuation, and the SRS effect so that the power ratio of ASE noise to nonlinearity is 3 dB for each channel at OMS level [70, 107]. The dynamic strategy requires not only "static" parameters, but also real-time "dynamic" parameters obtained from the monitoring of the network (see 2.1), either directly (output power spectrum of the first and last amplifiers at each OMS, total input and output powers at each amplifier) or indirectly through parameters refinement (connector losses, gain spectra, power spectra of the in-line amplifiers) [85]. This strategy relies on real-time monitoring of the network, therefore, it can provide dynamic changes to the network state. The optimal power per channel at the booster of each OMS has been

Table 2.1: Required parameters for power re-optimization.

"Static" parameters (design and commissioning)	**"Dynamic" parameters (real-time monitoring)**
fiber type; fiber length; span loss; connector loss (estimated)	total input and output powers at each amplifier; output power spectrum at WSS sides at each OMS; gain, power profiles of the in-line amplifiers (estimated)

computed and adjusted with current network configuration to attain the heuristic rule targeting 3 dB for the ASE noise to non-linear power ratio for each channel at each OMS similarly to [70, 107]. In the following results, we observe that this dynamic power re-optimization strategy outperforms the static strategy thanks to the feedback of real-time monitoring.

2.4. Network Loading Scenario

We consider a mesh optical network where services are progressively loaded and power re-optimization is periodically applied to all existing services (both previously established and newly loaded). The source and destination nodes of each service are randomly selected among network nodes.

Without loss of generality, the service route is determined using a shortest-path routing algorithm, and wavelength assignment follows a first-fit strategy, allocating wavelengths from longer to shorter ones. If a service is blocked due to insufficient resources, a new demand is generated, until the network reaches full load.

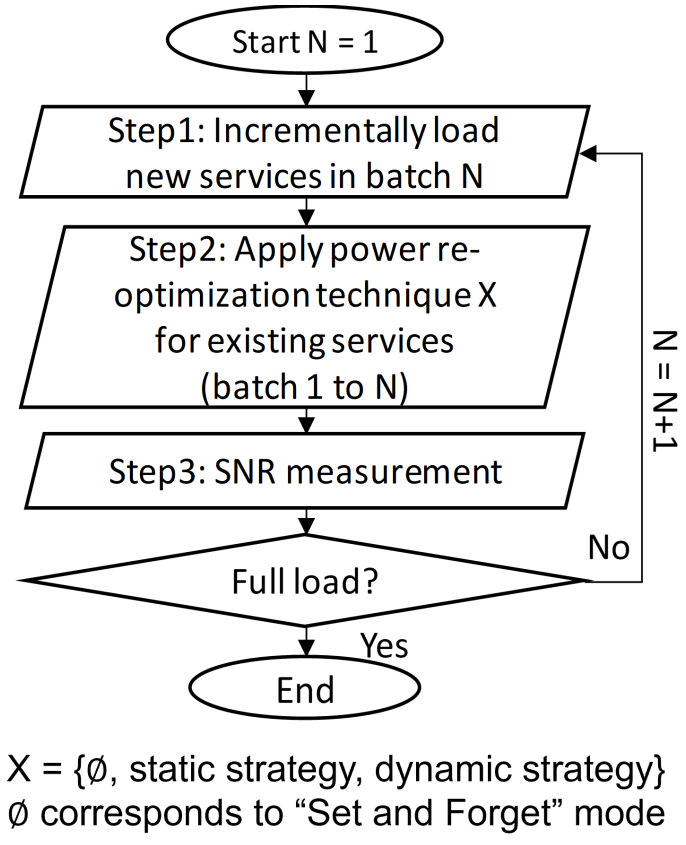


Figure 2.1: Flowchart of the experiment.

The overall procedure is summarized in the flowchart of Fig.2.1.

For each service batch N:

- Sequentially establish each new service of batch N and set its launch power at every crossed OMS according to the static end-of-life (EoL) design power P_{LOGO} (see Section 2.3.1). Previous services in the same batch are not re-optimized in this step.
- Once all services of batch N are loaded, apply power re-optimization to all existing services (both previous and new) using one of the following strategies: a) "Set and forget" (i.e., no re-optimization), or b) Static power strategy (Section 2.3.1), c) Dynamic power strategy (Section 2.3.2),
- Measure the signal-to-noise ratios (SNRs) of all services currently in the network.
- Repeat with next batch $N + 1$ until network becomes fully loaded.

Note that with "set and forget" mode, the launch power of each new service is set as P_{LOGO}, but never re-optimized regardless of power drift induced by loading new services in the network.

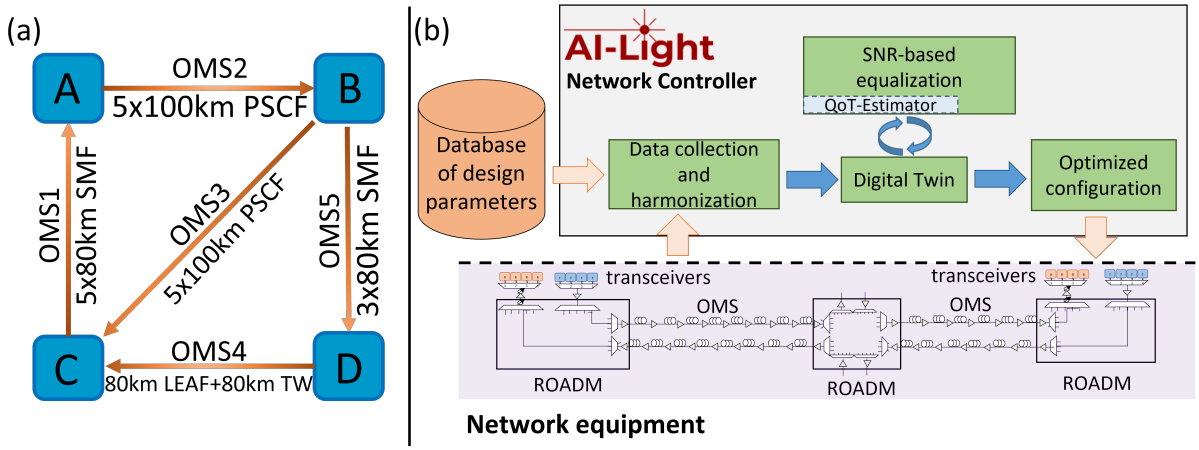


Figure 2.2: (a) Topology of the experimental mesh network; (b) AI-Light SDN framework.

2.5. Experimental Testbed

We experimentally implement in our lab a mesh network with 4 nodes (A, B, C, D), 5 (unidirectional) OMSes, whose topology is depicted in Fig. 2.2(a).

Tab. 2.2 shows the routing table of 12 paths with corresponding source node, sink node, crossed OMS, and path lengths. Span information such as span number, fiber type, fiber

Table 2.2: Routing table.

Source	Sink	Path	Length (km)
A	B	OMS2	500
A	C	OMS2–OMS3	1000
A	D	OMS2–OMS5	740
B	A	OMS3–OMS1	640
B	C	OMS3	500
B	D	OMS5	240
C	A	OMS1	400
C	B	OMS1–OMS2	900
C	D	OMS1–OMS2–OMS5	1140
D	A	OMS4–OMS1	560
D	B	OMS4–OMS1–OMS2	1060
D	C	OMS4	160

Table 2.3: OMS per span information and corresponding P_{LOGO}.

	OMS1	**OMS2**	**OMS3**	**OMS4**	**OMS5**
Spans	5×80 km SMF	5×100 km PSCF		80 km LEAF+80 km TW	3×80 km SMF
P_{LOGO} (dBm)	[2.9, 4.1, 2.2, 1.9, 3.1]	[5.1, 4.7, 6.7, 4.4, 6.0]	[4.5, 4.6, 6.1, 4.5, 5.4]	[0.8, 1.2]	[3.1, 4.4, 3.0]

length of each OMS are shown both in Fig. 2.2 and Tab. 2.3. Since the traffic demand is increasing exponentially in recent years, we emulate exponential number of arrivals of new services by progressively loading 7 batches of services having size: 5, 5, 10, 20, 40, 80 and 132. Hence, over the time, the total number of services in the network will be 5, 10, 20, 40, 80, 160 and 292 after loading each new batch. In the experiment, the network is fully loaded when 292 services are loaded and all the wavelengths (80 channels of 75GHz on the 6THz C band) on all links are occupied.

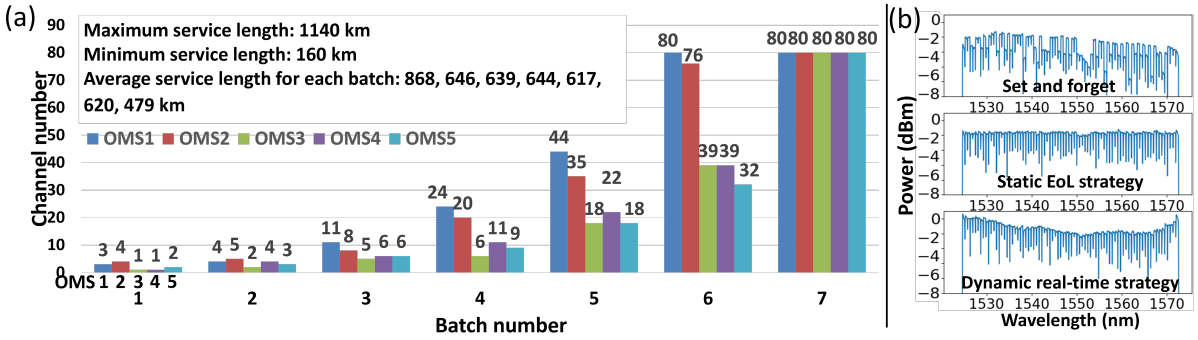


Figure 2.3: (a) Number of services transported by each OMS after loading each batch; (b) Full-load normalized power spectrum at the output of the first EDFA of OMS1 with the "set and forget" operation mode, static strategy, and dynamic strategy.

Fig. 2.3(a) shows the allocation statistics for each batch; note that the maximum service length is 1140 km and the average service lengths in each batch are similar to service lengths in real typical large metro or small core networks.

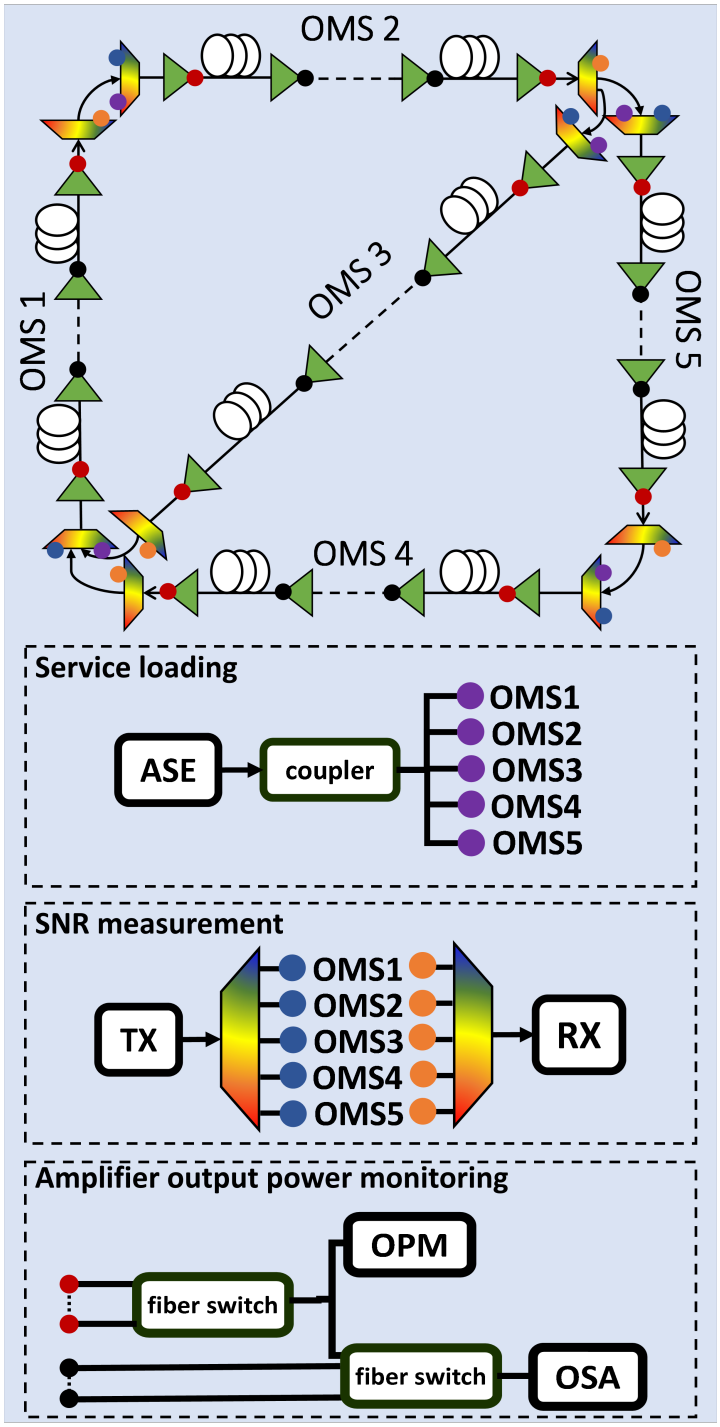


Figure 2.4: Experimental testbed with details about service loading by ASE source, SNR measurement by transponder, and output power monitoring by OPM (OSA is for results analysis).

Fig. 2.4 shows some further details of the experimental testbed. Only commercial equipment is used to implement the network. The transmitter (TX) of the transponder is

connected to a WSS whose ports are connected to each OMS (blue dots shown in Fig. 2.4). Then the egress of each OMS is connected to a port of a WSS (orange dots shown in Fig. 2.4) which is connected to the receiver (RX) of the transponder. Such architecture is used to automate the SNR measurement of different paths in the network. In the experiment, the real-time commercial transponder generates a Polarization-Division-Multiplexed QPSK signal with 68Gbaud baud rate, 200 Gb/s bit rate with 75GHz channel spacing. In addition, we rely on an ASE source when we progressively load the network to emulate all the services that are allocated in the network. ASE source is connected using a coupler to each OMS (purple dots shown in Fig. 2.4). The launch power of these dummy services is set at the targeted value computed by power optimization strategies, i.e., static or dynamic strategy. Then, we measure the SNR of each service by sequentially replacing each dummy service with the signal generated from the commercial transponder. We measure the pre-FEC BER reveived by the transponder, and we transfer the measured BER to the measured SNR depending on the modulation format as shown in [52]. ASE source is the only part in the experiment that does not rely on commercial equipment. To monitor power spectrums, we use an Optical Power Meters (OPM) and Optical Spectrum Analyzer (OSA). Power monitoring points are marked as red (by OPM or OSA) and black (by OSA). OPM is a commercial product that monitors the per-channel output power at the first and last amplifier of each OMS, as in a real network, rather than a lab-grade OSA (an OPM is a low-cost OSA with lower accuracy), while OSA monitors the output power spectrum of each amplfier, however, it is not involved in the optimization process nor in the configuration of the network. The OSA has been only used to better observe and analyze results. All monitoring points are connected with fiber switches so that the power spectrum of interest can be switched and monitored. Optical amplifiers and WSSes are also commercial products. Unless otherwise stated, we use only information available in real networks such as total input/output power monitored by photodiodes at each amplifier, output power spectrum at the first and last amplifier of each OMS (with an OPM as explained above), fiber length and fiber type of each span. In addition, to save time, we measured the SNR values of only odd-indexed services, hence half of the services. Without loss of generality, we report SNR margin which is defined as:

$$\mathrm{SNR}_{\mathrm{margin}} = \mathrm{SNR}_{\mathrm{monitored}} - \mathrm{SNR}_{\mathrm{FEC}} \tag{2.2}$$

where $SNR_{\mathrm{monitored}}$ is the monitored SNR by the real-time transponder and SNR_{FEC} is the minimum sufficient SNR that service needs for a successful transmission, which corresponds to FEC threshold.

Fig.2.2 summarizes the relation among service management, real-time monitoring, data collection, GN-model based SNR estimation and power re-optimization with our Autonomous Driving Network "AI-Light" Software Defined Networking (SDN) platform described in [42], which implements a digital twin. Our digital twin works similarly as GNPy [40], and we leverage it to compute optimal launch power of the dynamic power optimization strategy (Section 2.3.2) considering all load-dependent effects as described in Section 3.2, and also non-load-dependent effects such as WSS filtering and transponder back-to-back noise. The validation of our digital twin is shown in Section **??**.

Tab.2.3 shows the computed P_{LOGO} per span per OMS based on the "static" parameters. Note that P_{LOGO} of each span is also used to configure amplifiers' gain and tilt so that their output power matches the one provided by the LOGO. Notably, amplifier configurations are set at the beginning of the experiment and never reconfigured. Fig.2.3(b) shows examples of full load output power spectrum captured by an OSA at the first EDFA on OMS1 when the network is fully loaded. Each subplot shows the power spectrum for each power optimization strategy: "set and forget" (top), static (middle), and dynamic (bottom), highlighting the sharp differences in power allocation across different strategies.

2.6. Results

In this section, first we report results of channel power, gain variation, and SNR degradation of the previously established services induced by loading new batches of services (Section 2.6.1 and Figs. 2.5 and 2.6). Second, we show the SNR improvement by periodically applying both a static or a dynamic power strategy (Section 2.6.2 and Fig. 2.7). Finally, in Section 2.6.3 and Fig. 2.8 , we compare the predicted SNR vs. monitored SNR after the power re-optimization with static or dynamic strategy, showing that the expected SNRs predicted by our digital twin fit well the reality, demontrating the feasibility backand reliability of the re-optimization.

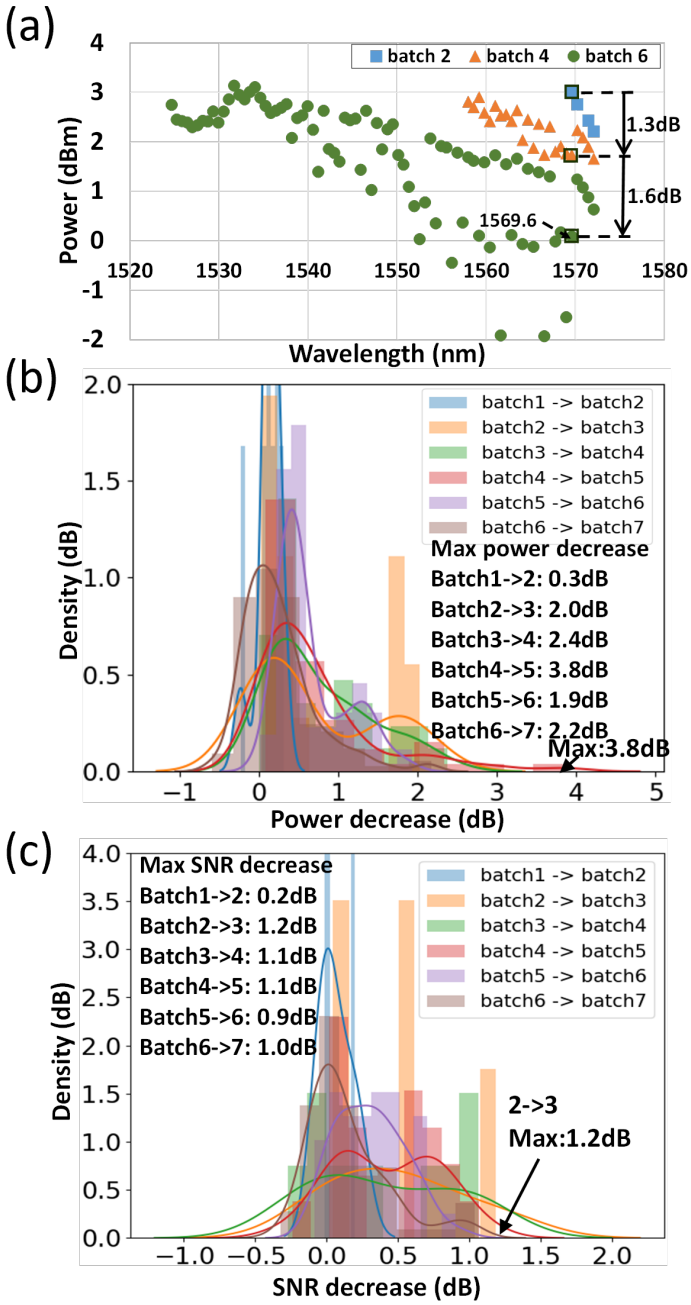


Figure 2.5: (a) Output power spectrum at the booster amplifier of OMS1 after loading batch 2/4/6; (b) Power decrease at the booster amplifier on each OMS of previously existing channels (batch N) due to loading new batch of services (batch $N+1$); (c) SNR decrease of existing services (batch N) due to loading new services (batch $N+1$).

2.6.1. SNR Degradation by Loading New Services

Fig. 2.5(a) shows the output power spectrum measured at the booster amplifier on OMS1 after loading different batches of services with the "set and forget" operation mode. After loading batch 2/4/6 respectively, the number of established channels on OMS1 are 4/24/80 (see Fig. 2.3(a)). We observe that the power of a sample service (with wavelength 1569.6 nm) decreases by 1.3 dB after 24 channels are established on OMS1 (batch 2 -> 4), then, the power of the same service decreases by an additional 1.6 dB after all 80 channels are loaded (full load) on OMS1 (batch 2 -> 6).

Statistical results of the power variation is shown in Fig. 2.5(b), which depicts the Probability Density Function (PDF) and maximum values of channel power decrease of existed channels in batch N induced by loading new services in batch $N+1$. The power is monitored at the output of the booster amplifier on each OMS. We observe that the maximum power drop induced by loading new batches reaches 3.8 dB for $N = 4$. The booster power variation is caused by both the load-dependent SRS variation and the gain spectrum variation due to loading new services. This shows that the power can drift dramatically with different load states in the network, which can cause SNR degradation, as described next.

Fig. 2.5(c) shows the PDF and maximum values of SNR degradation of previously established services in batch N impacted by loading new services in batch $N+1$. We observe that the maximum SNR decrease after loading new batches is up to 1.2 dB for $N = 2$. This SNR decrease of previously established services induced by loading new services warrants the great importance of applying power re-optimization strategy not only of new added services, but also of previously established services to avoid large SNR decrease, hence disruption of service when loading new services.

To further study the impact of loading new services, we focus on the first-loaded service ("Service #1").

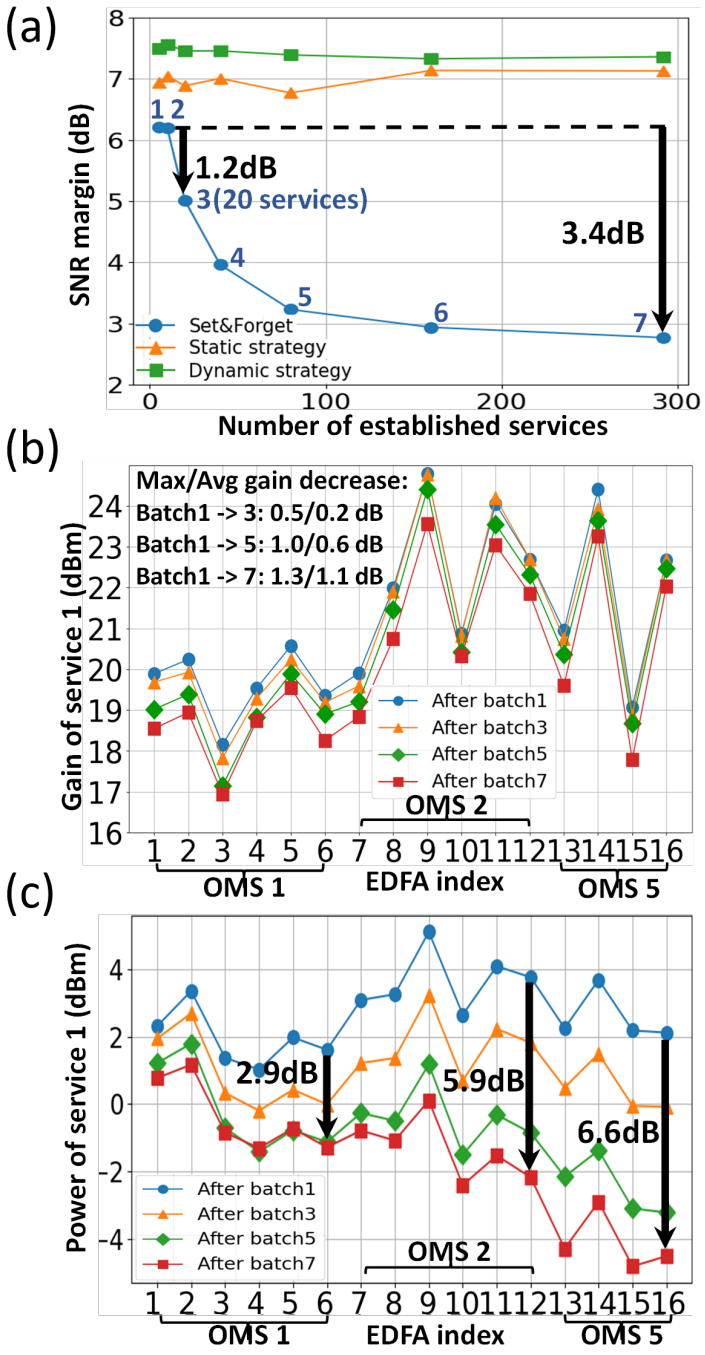


Figure 2.6: (a) SNR variation of Service #1 with different number of established services; (b) Gain of Service #1 at each traversed EDFA; (c) Power of Service #1 after each traversed EDFA.

In Fig. 2.6(a), the blue line shows the SNR degradation of Service #1 after sequentially loading each batch of services when applying "set and forget". Service #1 goes through OMS 1-2-5, crossing 13 heterogeneous spans and 16 EDFAs with service length of 1160km.

We observe that SNR of Service #1 starts to sharply drop by 1.2 dB after loading 3 batches of 20 services in the network and decreases by up to 3.4 dB after loading 7 batches of all 292 services, at which point the network is fully loaded.

To further study the SNR degradation caused by the load-dependence of EDFA gain profile, we track the variation of channel gain (Fig. 2.6(b)) and channel output power (Fig. 2.6(c)) with OSA along each EDFA that Service #1 crosses as different number of batches of services are loaded in the network. In Fig. 2.6(b), we observe that the channel gains of EDFAs crossed by Service #1 generally decrease as new services are loaded in the network (as ripples are load-dependent, it is possible that the power of some services increase as well). After loading all 292 services (batch 7), the maximum and average channel gain decrease are respectively 1.3 and 1.1 dB among all the crossed EDFAs. The channel gain variation induced by the load-dependence of the gain spectrum contributes to channel power variation, as shown in Fig. 2.6(c). In Fig. 2.6(c), we can observe that the channel output power measured at the end of transmission of Service #1 decreases by up to 6.6 dB when all 292 services are loaded in the network, which corresponds to up to 3.4 dB SNR drop in Fig. 2.6(a). We can also observe that the power decrease is roughly proportional to the number of crossed amplifiers due to the accumulation of gain variation induced by load-dependent gain profile of each EDFA. In Fig. 2.6(c), we observe 2.9/5.9/6.6 dB power decrease at the last EDFA of OMS 1/2/5 after loading all 292 services in the network. This could be also observed in Fig. 2.3(b), where the power spectrum was measured at the output of the first EDFA of OMS 1 with "set and forget" mode, shows roughly 3 different power levels due to different number of EDFAs that services cross before arriving to the first EDFA on OMS 1, and the lower channel powers correspond to larger power decreases, i.e., to services that cross more EDFAs, hence more OMSes.

Applying periodic power re-optimization strategy such as static strategy (in orange) or dynamic strategy (in green) in Fig. 2.6(a) mitigates the SNR degradation induced by loading new services. In Fig. 2.6(a), we can observe that SNR margin of the Service #1 can always be maintained at a high level after loading each batch of services until full load is reached. Indeed, for the Service #1, SNR margins are always improved of at least 6.5 dB when loading different number of services by applying the static strategy, and more than 7dB SNR margins is always achieved by the dynamic strategy. In addition, we can observe that SNR margins of the Service #1 are always higher with the dynamic strategy compared with the static strategy after each batch loading (e.g., in Fig. 2.6(a), green line is always above orange line). This is due to the better launch power setting at each OMS by applying dynamic power re-optimization that is based on more accurate

real-time monitoring during network life.

2.6.2. SNR Improvement by Power Re-optimization Strategies

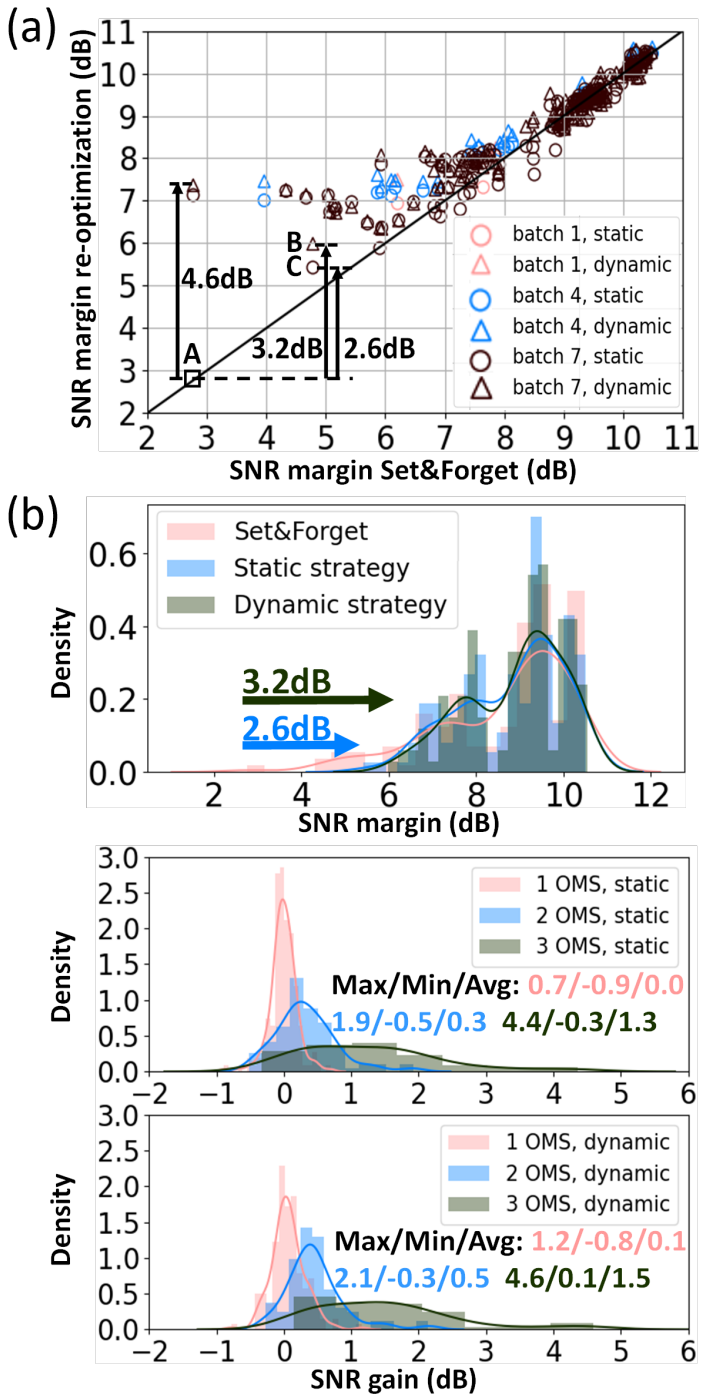


Figure 2.7: (a) SNR of services with power re-optimization strategies vs. "set and forget"; (b) PDF of SNR margins; (c) PDF of SNR gain per length (1, 2, 3 OMS) and per power re-optimization strategy.

Fig. 2.7(a) shows the SNR margin with static (circle) or dynamic (triangle) power re-optimization strategy vs. "set and forget" mode of operation after loading new batches of services. The diagonal black line shown in Fig. 2.7(a) corresponds to the situation where the power re-optimization does not improve/degrade SNR compared to "set and forget". Different colors correspond to different number of loaded services (after loading batch 1/4/7). We observe that most of the triangles and circles are above the black diagonal line, which means that most services' SNR margins with re-optimization strategies are larger than SNR margins with "set and forget" mode. Especially, after loading all 292 services in the network, the SNR margin of the service with the worst SNR improves by up to 4.6 dB with dynamic strategy. In addition, triangular markers are always above circle markers, which shows that dynamic strategy further improves SNR margins due to better adjustment to the actual monitored network configuration compared to the static strategy.

Fig. 2.7(b) shows the PDF of SNR margins of all 292 services when network is fully loaded for each power re-optimization strategy as well as "set and forget". Small SNR margins are all improved with both static and dynamic power re-optimization strategies. If we compare the smallest SNR margin among all services with and without power re-optimization, we observe in Fig. 2.7(b) that the smallest SNR margin is improved by 2.6 dB with the static strategy corresponding to A->C in Fig. 2.7(a) or 3.2 dB with the dynamic strategy corresponding to A->B in Fig. 2.7(a), where the smallest margin with "set and forget" is at point A, the margin with the dynamic strategy is at point B, and margin with the static strategy is at point C. This confirms that dynamic re-optimization strategy further improves SNR margin with respect to the static strategy thanks to real-time monitoring of network configuration.

Next, we study the correlation between SNR gain obtained by power re-optimization and the number of crossed OMSes. Fig. 2.7(c) shows the PDF of SNR gain of all existing services in the network after loading each batch (5, 10, 20, 40, 80, 160, 292 services are established in the network after loading each batch) when applying static (top) or dynamic (bottom) power re-optimization strategy compared to "set and forget" mode. Different colors correspond to SNR gain of services with different number of traversed OMSes. We can observe that after applying dynamic power re-optimization, the SNR decreases for a small number of services. This is because optimal launch power are not computed correctly by our digital twin mainly due to wrong estimation on back-to-back transponder penalty, which is highly transponder sample dependent especially for large SNR region [52, 164]. Thereby, a small number of SNRs corresponding to services crossing single OMS are not improved and, in fact, it decreases by up to 0.9 dB or 0.8 dB with static and dynamic

strategies respectively, however their margins remain still high. For services that cross 2 OMSes, their SNRs improve by up to 1.9 dB and average 0.3 dB with static strategy; up to 2.1 dB and average 0.5 dB with dynamic strategy. SNRs of certain services decrease slightly by 0.5dB and 0.3 dB with static and dynamic re-optimization respectively due to the same reason as described above. Finally, for services that cross 3 OMSes, SNRs are improved with both static and dynamic power re-optimization strategies. Dynamic power re-optimization strategy improves better SNRs for services with 3 OMSes compared to static power re-optimization strategy. The maximum improvement is 4.4 dB, and the average improvement is 1.3 dB by the static strategy, while maximum improvement is 4.6 dB, average improvement is 1.5dB by the dynamic strategy. Notably, the SNRs of the services that cross 3 OMSes are the smallest compared to services with 1 or 2 OMSes, however, these SNRs are always improved with dynamic power re-optimization strategy with a positive 0.1 dB minimum SNR improvement, average 1.5 dB SNR improvement, and maximum 4.6 dB improvement.

2.6.3. Predicted SNR vs. Monitored SNR with Power Re-optimization

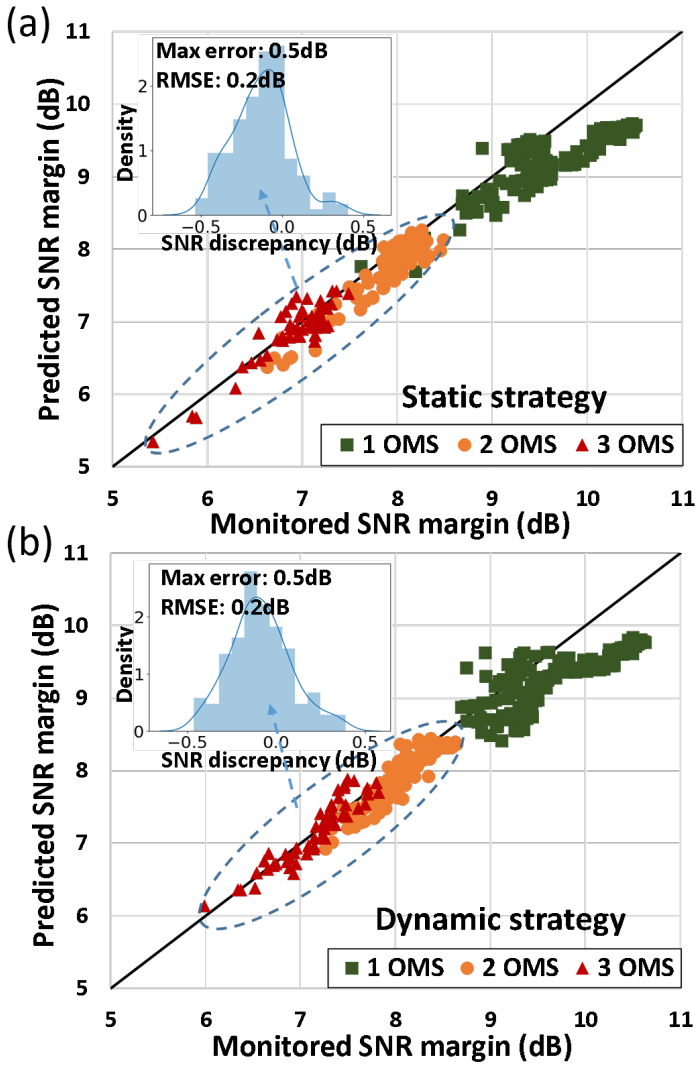


Figure 2.8: Predicted SNR margin vs. measured SNR margin with (a) static strategy; (b) dynamic strategy.

Accurate QoT estimation/prediction by the digital twin is of key importance for accurate optimal launch power computation, ensuring that services can run at their optimum SNRs during network lifetime. In this section, we validate the accuracy of our digital twin by comparing the SNRs predicted by our digital twin using the optimal launch power computed at Step 1 of Fig. 2.1 vs. the monitored SNRs by the transponder after applying power re-optimization strategies, i.e., at Step 3. Since SNRs are predicted using the computed optimal launch power, the predicted SNRs are ones that we expect to

achieve. Notably, only information available in real networks (see Tab. 2.1) is used for both launch power computation and SNR prediction.

In Fig. 2.8, we compare the predicted SNRs vs. monitored SNRs for both static (Fig. 2.8(a)) and dynamic (Fig. 2.8(b)) power re-optimization strategies after loading each batch of services. The diagonal black line shown in Fig. 2.8 corresponds to the hypothetical situation where SNRs monitored by the transponder are ideally predicted by the digital twin. As shown in both Figs. 2.8(a) and (b), SNRs are predicted more accurately for services with smaller SNRs which cross two (orange circles) or three OMSes (red triangles). All the services with large SNRs cross a single OMS (green squares), and they are mainly limited by transponder back-to-back noise, which is determined in our digital twin by two parameters obtained from SNR vs. OSNR back-to-back curve fitting (one is the offset between the characterization curve on the OSNR axis and the ideal SNR=OSNR curve; and the other is the asymptotic value for SNR). Since smaller SNRs have less margin and are more critical to be estimated/predicted accurately, the two mentioned back-to-back parameters are chosen to fit better smaller SNRs by sacrificing the fitting accuracy for large SNRs. Thereby large SNRs are predicted less accurately; however, SNR margins are still high for those services, so lower accuracy of prediction is still acceptable. Good prediction on small SNRs is more important because services with small SNRs have less margin, hence easier to get disrupted due to wrongly predicted launch power setting. Inset PDF plots shows the SNR discrepancy between prediction and monitoring only for services that cross two and three OMSes (orange round points and red triangle points inside dashed blue circle). The maximum prediction error is 0.5 dB and the RMSE is 0.2 dB for both static and dynamic strategy, which can come from intrinsic QoT estimator error and inaccurate parameters estimation i.e., connector losses and gain/power spectra of in-line amplifiers. The result shows that the predicted SNRs by our digital twin fits acceptably the monitored SNRs after applying power re-optimization strategy. Such accuracy of the digital twin during power re-optimization suggests that a feasible and reliable power re-optimization strategy can be applied in practice.

2.7. Conclusions

In this study, we experimentally quantify the impact of establishing new services on previously established services on a 5-OMS testbed using commercial equipment. We observe that SNRs of previously established services are decreased by up to 3.4 dB after loading close to 300 services in the network. To study SNR degradation due to loading new services in the network, we track the output power variation at each crossed EDFA

of the first loaded service as example after loading different number of services in the network, and we find 6.6 dB power decrease at the end of transmission after propagating through 16 EDFAs.

Then, we apply two different strategies, a static and a dynamic strategy, to mitigate the SNR degradation due to loading of new services in the network. We find that, using periodic per-channel, per-OMS power re-optimization strategies, SNR margin is improved by up to 2.6 dB with the static strategy that needs only "static" parameters that can be obtained from design and at commissioning, or 3.2 dB with a dynamic strategy that needs not only "static" but also "dynamic" real-time monitoring information. Both strategies significantly improve the robustness of the network thanks to largely improved SNR margin of the worst service. Finally, we compare the predicted SNR and monitored SNR with applying static or dynamic power re-optimization strategy, and we find a good match between predicted and monitored SNR, which shows the optimized SNRs can be well predicted.

One limitation of this work is that we did not consider service dropping induced by fiber cuts. If a fiber cut happens, network load will change, which means we need to apply power re-optimization again for the OMSes traversed by the dropped services, which is time consuming. In the future, we may consider predicting power drift after loading new services in the network in order to reduce power re-optimization time to meet more practical requirements in real networks (e.g., power re-optimization including in fast re-routing to recover service caused by fiber cut with good SNR margin). Moreover, all the issues related to the scalability of the proposed strategy as well as the transient of the devices are critical aspects which we are planning to assess.

3 | QoT Estimation Improvement with Inputs Refinement Tool for C+L Networks

3.1. Abstract

We propose a technique to estimate lumped losses thus OSNR, nonlinear SNR, GSNR, and SNR in C+L optical networks. We show with simulations that SNR estimation accuracy is within 0.5dB and that the technique is robust to uncertainty due to aging.

3.2. Introduction

Accurately estimating the quality of transmission (QoT), such as the signal-to-noise ratio (SNR) of services, can increase network capacity by reducing overestimated design margins in WDM optical fiber networks [102]. SNR inaccuracies arise from both the QoT models [101, 117] and the inputs to these models. This paper focuses on the latter. "Input refinement" tools have been proposed, e.g., in [3, 85, 86], to refine knowledge of key sources of uncertainty, namely the lumped losses such as connector losses at the beginning and end of each span in single-band transmission systems.

As multi-band systems such as C+L are deployed in commercial networks, any uncertainty in the actual power entering the fiber after the connectors will affect the estimation of the Kerr effect and the band-dependent losses induced by stimulated Raman scattering (SRS). This exacerbates the uncertainty of SNR estimation.

In this paper, we propose an input refinement tool for C+L networks to address per-band uncertainties. Using simulations over a three-span optical multiplex section (OMS), we show that the optical SNR (OSNR), which accounts for amplified spontaneous emission (ASE) noise, is estimated with a root-mean-square error (RMSE) lower than 0.2 dB; the nonlinear SNR, which accounts for the Kerr effect, with RMSE lower than 1.2 dB; and

the generalized SNR (GSNR), which includes both ASE noise and Kerr nonlinearity, with RMSE lower than 0.5 dB.

Furthermore, we extend the simulations to a cascade of 10 OMSs of three spans each, with highly heterogeneous lengths. In this case, the RMSE of the estimated SNR—which accounts for transponder and wavelength-selective switch (WSS) filtering penalties in addition to GSNR—remains below 0.4 dB. We also show that input refinement achieves high accuracy (RMSE $<$ 0.5 dB) even in aging scenarios where splice losses in fibers are not precisely known.

3.3. Setup and Assumptions

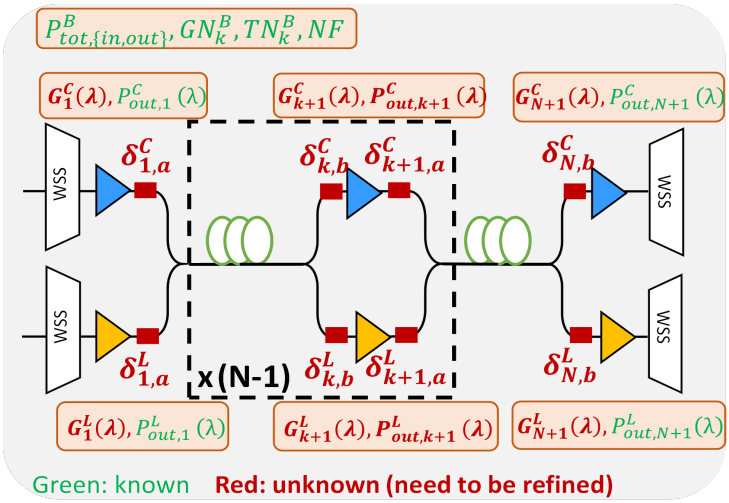


Figure 3.1: Generic N-span OMS C+L system.

Fig. 3.1 depicts a generic N-span C+L OMS. Parameters shown in green are monitored and thus known in real networks: the total input/output power at each amplifier, $P^B_{\text{tot},\{in,out\}}$, for each band $B \in \{C, L\}$, and the output power spectrum after the first (booster, "1") and last ("$N+1$") amplifier of the line, $P^B_{\text{out},\{1,N+1\}}(\lambda)$.

Parameters shown in red are unknown in real networks and must be refined: the lumped losses $\delta^B_{k,\{a,b\}}$ (connector and band multiplexer (MUX) and de-multiplexer (DEMUX)) at the input (a) and output (b) of the kth span, the rippled gain spectrum $G^B_k(\lambda)$ for the kth amplifier, and the output power spectrum $P^B_{\text{out},k}$ of the kth in-line amplifier.

In addition, the nominal (mean) gain GN^B_k and tilt TN^B_k are configured for each span k and band B, and are therefore known. For simplicity, we assume that all amplifiers

share the same noise figure NF. Finally, we assume the use of standard single-mode fiber (SMF), which includes the wavelength-dependent loss as characterized in our laboratory.

3.4. Method Description

In this paper, we compare GSNR and SNR estimation in a transmission scenario using three different methods: Input Refinement (IR), Input Refinement with Ground Truth gain spectrum (IRGT), and a naïve baseline.

Input Refinement (IR)

Initialization: Each amplifier is assumed to have an exactly linear tilt with nominal gain GN_k^B and tilt TN_k^B.

Step 1: Using a gradient descent technique, we propagate $P^B_{\text{out},1}(\lambda)$ through the OMS using our QoT tool and find the optimal lumped loss combination $\{\delta^B_{k,\{a,b\}}\}$ for each span k and band B that minimizes the estimation error on $P^B_{\text{out},N+1}(\lambda)$.

Step 2: We estimate $G_k^B(\lambda)$ by applying $\{\delta^B_{k,\{a,b\}}\}$ obtained from Step 1, again minimizing the same error cost function.

Steps 1 and 2 are iterated until the error cost function falls below a predefined threshold.

Input Refinement with Ground Truth Gain Spectrum (IRGT)

To evaluate whether inaccuracies of IR originate from lumped loss estimation or from amplifier gain spectrum estimation, we employ the ground truth gain spectrum (including ripples) instead of the assumed linear tilted gain spectrum in the above algorithm.

Baseline

For each span and band, we obtain the total lumped loss as the span loss (measured by photodiodes at each amplifier) minus the fiber loss (estimated from the linear attenuation and fiber length). This total lumped loss is then uniformly distributed 50%/50% before and after the span.

Subsequently, the difference in output power spectrum between the first and last amplifier, $P^B_{\text{out},1}(\lambda) - P^B_{\text{out},N+1}(\lambda)$, is uniformly distributed among all in-line amplifiers to set the per-span, per-band launch power $P^B_{\text{out},k}(\lambda)$. From this, we derive the input power $P^B_{\text{in},k}(\lambda)$ for $k > 1$ (in-line amplifiers and pre-amplifier) via per-span propagation. Amplifier gains are

then configured as

$$G_k^B = P_{\text{out},k}^B(\lambda) - P_{\text{in},k}^B(\lambda), \quad k > 1,$$

ensuring that the output power spectrum at the last amplifier of each band, $P_{\text{out},N+1}^B(\lambda)$, matches the ground truth power spectrum at the end of the OMS. Finally, our QoT model is applied to estimate the (G)SNR.

3.5. Simulation Results

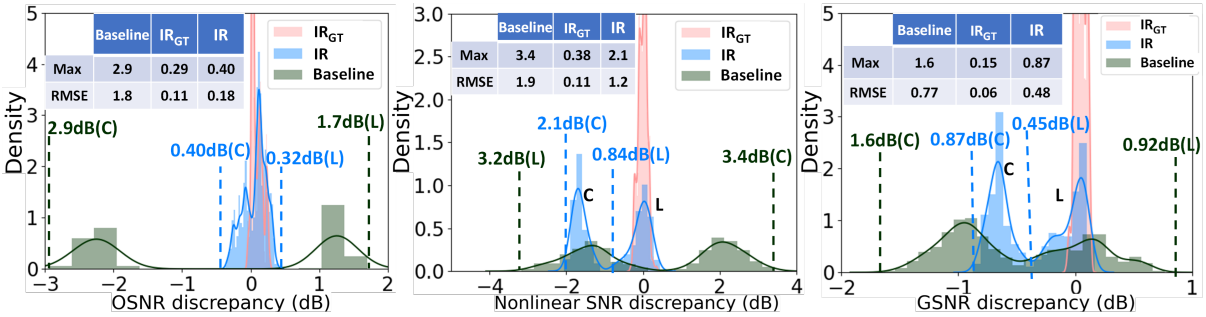


Figure 3.2: (a) OSNR, (b) Nonlinear SNR, (c) GSNR estimation in scenario 1 (3-span single OMS).

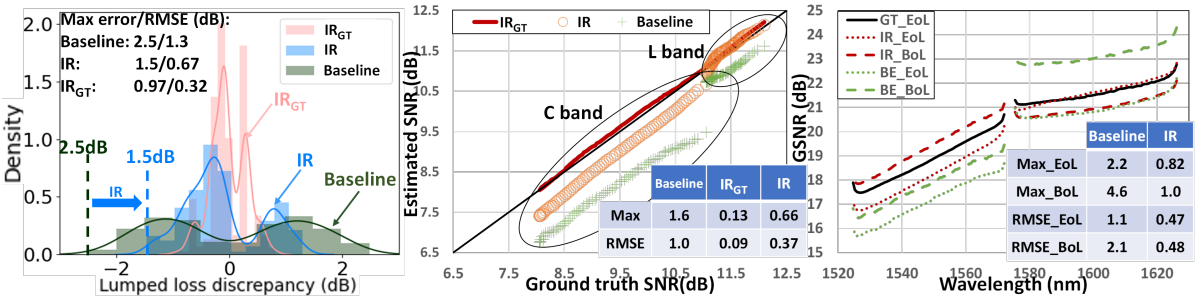


Figure 3.3: (a) Lumped loss estimation in scenario 1 (3-span single OMS); (b) SNR estimation after 10 OMSes in scenario 2 (10 OMSes with 3 spans); (c) GSNR estimation with aging in scenario 3 (aging).

We run all simulations in a 6+6 THz C+L system with 75 GHz channel spacing, yielding 80 channels per band. The baud rate of the emulated channels is 68 Gbaud with 200 Gb/s PDM-QPSK modulation. Lumped losses (connector losses + band MUX/DEMUX losses) are uniformly randomly varied within [1.5, 4] dB; gain ripples are heterogeneous and randomly drawn from a set of five real lab-measured spectra. Amplifiers are configured following the strategy proposed in [39], with booster output power optimized to set the

ASE-to-nonlinear power ratio to 3 dB. In all simulations, the amplifier noise figure is set to $NF = 4.5$ dB, without loss of generality.

Scenario 1: Single OMS (3 spans)

We first consider a single OMS consisting of three SMF spans of 80 km each. Results are reported for 54 independent simulations, each corresponding to a random allocation of lumped losses per span and per band.

Figs. 3.2(a,b,c) and Fig. 3(a) show the probability density function (PDF) of OSNR, nonlinear SNR, GSNR, and lumped loss estimation error, respectively. Inset tables report statistics (in dB) across the 54 simulations.

- **OSNR:** The baseline is inaccurate by up to 2.9/1.7 dB for the C/L bands, while IR improves the maximum error to 0.40/0.32 dB. IR also reduces the RMSE from 1.8 to 0.18 dB, close to IRGT (max error: 0.29 dB, RMSE: 0.11 dB). The residual error stems mainly from lumped loss estimation, since IRGT uses ground truth gain spectra. - **Nonlinear SNR:** As shown in Fig. 3.2(b), the baseline is inaccurate by up to 3.4/3.2 dB for C/L bands. IR improves accuracy (max error: 2.1/0.84 dB), reducing RMSE from 1.9 to 1.2 dB. With IRGT, accuracy is further improved (max error: 0.38 dB, RMSE: 0.11 dB). - **GSNR:** Fig. 3.2(c) shows the baseline is inaccurate by up to 1.6/0.92 dB (C/L). IR improves accuracy (max error: 0.87/0.45 dB), reducing RMSE from 0.77 to 0.48 dB. - **Lumped losses:** Fig. 3.3(a) shows the baseline has maximum error of 2.5 dB and RMSE of 1.3 dB—spanning the entire [1.5, 4] dB randomization range. IR improves this significantly (max error: 1.5 dB, RMSE: 0.67 dB). With IRGT, accuracy improves further (max error < 1 dB, RMSE ≈ 0.3 dB).

Scenario 2: Cascade of 10 OMSs (3 spans each)

We next consider a cascade of 10 OMSs, each with three spans of random fiber lengths (max: 116 km, min: 40 km, mean: 75 km, std. 20 km). SNR is estimated including transponder back-to-back penalties and WSS filtering penalties (using transfer functions of commercial 75 GHz filters characterized in our lab).

Fig. **??**(b) reports SNR estimation versus ground truth SNR for all 160 channels. Lumped losses (120 in total: 30 spans $\times$ 2 bands $\times$ 2 positions per span) are independently drawn from [1.5, 4] dB.

At the end of the cascade: - The baseline yields maximum error of 1.6 dB and RMSE of 1.0 dB. - IR reduces the maximum error to 0.66 dB and RMSE to 0.37 dB. - IRGT

achieves near-perfect accuracy (max error < 0.2 dB, RMSE < 0.1 dB). This confirms that all residual uncertainty in IR arises from lumped loss misestimation.

Scenario 3: Aging Robustness

Finally, we test the robustness of IR to fiber aging on the same 3-span OMS used in Scenario 1. IR assumes the average fiber attenuation is known when computing lumped losses. However, as networks age and repairs introduce splices, the average attenuation becomes uncertain.

We model this by defining Beginning-of-Life (BoL) attenuation α_{BoL} and End-of-Life (EoL) attenuation $\alpha_{\text{EoL}} = \alpha_{\text{BoL}} + 0.05$ dB/km. Ground truth (GT_EoL) is obtained using α_{EoL}, while IR is run assuming either incorrect attenuation α_{BoL} (IR_BoL) or correct attenuation α_{EoL} (IR_EoL).

Fig. 3.3(c) and the inset tables report statistics over 54 simulations: - (a) IR_EoL (max error: 0.82 dB, RMSE: 0.47 dB) and IR_BoL (max error: 1.0 dB, RMSE: 0.48 dB) yield very similar accuracy. When attenuation is set incorrectly, IR maps the additional fiber loss to lumped losses, preserving the physics of propagation. Thus, GSNR estimation accuracy remains unaffected. By contrast, the baseline suffers large errors: max GSNR error grows from 2.2 dB (with correct attenuation) to 4.6 dB (with incorrect attenuation). - (b) IR applied with $\alpha = \alpha_{\text{BoL}}+0.05$ (IR_EoL) estimates GSNR as accurately as IR_BoL. However, the baseline degrades from max/RMSE errors of 1.6/0.77 dB ($\alpha = \alpha_{\text{BoL}}$) to 2.2/1.1 dB ($\alpha = \alpha_{\text{BoL}} + 0.05$).

These results demonstrate that IR is robust to moderate uncertainties in fiber attenuation, unlike the baseline.

3.6. Conclusions

We proposed and validated with simulations an inputs refinement tool which can be used to improve QoT estimation for C+L systems. On a 3-span OMS, the RMSE of estimated OSNR is as low as 0.2dB, the maximum error of estimated nonlinear SNR can be improved by 1.3dB, RMSE of estimated GSNR can be improved to below 0.5dB, and RMSE for estimated connector loss is around 0.7dB. For a network of 10 OMSes of 3 spans each with high span length heterogeneity, the SNR estimation accuracy is also better than 0.5dB (RMSE). Finally, we show that the inputs refinement tool estimates GSNR accurately when the fiber loss is not accurately known, e.g., in the context of aging.

4 | Digital-Twin-Based Active Inputs Refinement for Insertion Loss Estimation and QoT optimization in C and C+L Networks

4.1. Abstract

Quality of Transmission (QoT) prediction is a fundamental function in optical networks. It is typically embedded within a digital twin, and it is used for many operational tasks, including service establishment, service rerouting and (per-channel or per-amplifier) power management to optimize the working point of services and hence to maximize their capacity. Any inaccuracy in QoT prediction results in additional, unwanted design margins. A key contributor to QoT inaccuracy is the uncertain knowledge of fiber insertion loss, e.g., the attenuation due to connector losses at the beginning or at the end of each fiber span, as such loss cannot be directly monitored. Indeed, insertion losses drive the choice of the launch power in fiber spans, which in turn drive key physical effects, including the Kerr and Stimulated Raman Scattering (SRS) effects, that strongly affect services' QoT. It is thus very important to estimate (and detect possibly anomalous) fiber insertion losses at each span. We thereby propose a novel Active Inputs Refinement (AIR) technique using active probing to estimate insertion losses in both C and C+L systems. Here, active probing consists in adjusting amplifier gains span by span to slightly alter Stimulated Raman Scattering (SRS). The amount of adjustment must be sufficient to be measurable (such that insertion losses can be inferred from the measures), but small enough to have a negligible impact on running services in a live network. The method is validated by simulations on a European network with 30 Optical Multiplex Sections (OMSs) in both C and C+L configurations, and by lab experiments on a C-band network, demonstrating

that AIR significantly improves insertion loss estimation, network QoT optimization , and QoT prediction compared to other state-of-the-art monitoring techniques. This work underscores the critical role of accurate estimation of QoT inputs in enhancing optical network performance.

4.2. Introduction

4.2.1. Motivation

Thanks to the recent improvements in optical network monitoring, new opportunities to achieve superior Quality of Transmission (QoT) optimization of services in optical networks are starting to emerge. Connectivity services in optical networks co-propagate, in the form of end-to-end optical circuits, over different wavelengths through one or several links or Optical Multiplex Sections (OMSs). Consequently, the QoT, expressed, e.g., as Bit Error Rate (BER), Q factor, and Signal-to-Noise Ratio (SNR), of these services can be affected by various physical effects, including the fiber nonlinearity that consists of Stimulated Raman Scattering (SRS) and Kerr effect (i.e., self-phase modulation, cross-phase modulation, four-wave mixing) that are highly dependent on the launch power entering to the fiber ; and the load-dependent gain and noise figure spectrum of Erbium-Doped Fiber Amplifiers (EDFA), leading to Amplified Spontaneous Emission (ASE) noise and affecting the Optical Signal to Noise Ratio (OSNR).

Connector insertion loss refers to the loss of optical power that occurs when a connector is inserted between two optical devices. For example, the insertion loss between an optical amplifier and an optical fiber affects the launch power entering the fiber. Moreover, for each fiber span, the insertion loss contributes to the total span loss. As a result, per-span insertion loss indirectly affects both fiber nonlinear effects (Kerr and SRS effects, determined by the launch power into the span) and ASE noise (determined by the amplifier gain set according to the span loss). The insertion loss is generally difficult to measure in practice due to lack of monitoring at connectors. Large insertion loss can be caused by dirty, aged, or incorrectly inserted connectors, which can degrade QoT of services in the optical network. Furthermore, uncertainty of insertion losses affects QoT prediction for network design [41, 102]. Thus, good knowledge of insertion losses can help both the design and maintenance of optical networks.

In optical networks, QoT of services should be always maintained above the required level to ensure successful data transmission. Specifically, the BER (resp., SNR) of services must be lower (resp., larger) than the Forward Error Correction (FEC) threshold. However, as

mentioned before, the QoT of services can vary due to 1) changed load-dependent effects [77, 150] when adding or dropping services and 2) dirty/aged connectors that affect fiber nonlinear effects and ASE noise. Thus, QoT (re-) optimization in physical-layer networks is essential to maintain services running at an optimum state over the network's lifespan to avoid services outage.

QoT optimization is recently carried out using a Digital Twin (DT), which is a virtual replica of the physical network. The DT models the outcome of tentative physical actions on the performance of the physical network, enabling what-if scenario analysis [35, 138]. In this study, the DT performs QoT optimization by setting the optimal configurations of the launch power spectrum and of the amplifier's gain and tilt [48, 123, 138, 150]. Such optimization can only be effective if the DT can accurately predict the outcome of the optimization process. Indeed, an inaccurate DT would lead to perform actions assessed to be optimal by the DT, but in fact resulting in a suboptimum network state, possibly even degrading the QoT of some services. A DT that can accurately predict the impact any physical layer change is thus needed to enable reliable and efficient network re-optimization [123, 151, 154].

A DT may be implemented with neural networks to optimize and predict QoT [105, 108, 118, 141, 148**?**]; however, the performance heavily relies on the training data sets, making it difficult to apply in real networks due to challenges in data collection and to predict unseen scenarios. Moreover, neural networks are largely unexplainable black boxes, where the lack of interpretability can raise problems for troubleshooting and operator trust.

Another more traditional approach, which we use in this study, involves using analytical models to quantify physical effects, i.e., SRS, ASE noise/OSNR, fiber nonlinearity, etc. A closed-form Gaussian Noise (GN) model [101], considering the SRS effect, has been proven fast and accurate with correct model input parameters [117].

Thus, the accuracy of our analytical model-based DT mainly relies on the accuracy of the model input parameters. However, in current networks, certain input parameters are difficult to obtain due to a lack of monitoring, such as connector insertion losses (for Kerr and SRS effects modelling) and amplifier gain spectra (for ASE noise modelling). Hence, the accurate knowledge of insertion losses and gain spectra of amplifiers are key for accurate physical effects modeling and, consequently, accurate QoT optimization and prediction [79].

In this study, we develop a new active input refinement (AIR) method to accurately estimate insertion losses to be used on our DT, and then we combine our proposed method for insertion loss estimation with our previous work [85] for amplifier gain spectrum esti-

mation to build an accurate DT for QoT optimization and prediction.

4.2.2. State of the Art

Table 4.1: Input parameters refinement techniques.

Ref. (band)	**Main Assumptions**	**Estimated Parameters**
[3] (C)	Measured OSNR at OMS	Insertion loss, amplifier noise figure spectrum
[15] (C)	Measured OSNR at OMS, measured output power spectrum at OMS, homogeneous rippled gain spectrum	Fiber parameters, insertion loss, average amplifier noise figure
[85] (C)	Measured output power spectrum at OMS	Insertion loss, amplifier gain spectrum
[151] (C+L)	Measured output power spectrum at OMS	Insertion loss, amplifier gain spectrum
[87] (C)	Measured output power spectrum at OMS, trained EDFA model	Insertion loss, amplifier gain spectrum
[163] (C+L)	Measured output power spectrum at each span, ripple-less gain spectrum	Insertion loss
AIR (proposed, C and C+L)	Measured output power spectrum at OMS, fully ASE-loaded, calibrated full-load amplifier gain spectrum, possibility to adjust amplifier settings on demand (the "active" part)	Insertion loss

Tab. 4.1 surveys some existing techniques for inputs refinement used to achieve accurate QoT prediction. In [3], Ayassi et al. used a Bayesian-optimization-based algorithm to

estimate the connector insertion losses and amplifiers' noise figures by minimizing the OSNR estimation error. The algorithm takes into account only ASE noise, while fiber nonlinear noise was not considered, which impacts SNR estimation accuracy. In [15], Borraccini et al. proposed a method to alter the amplifier gain and tilt settings to estimate fiber parameters (i.e., effective area, loss coefficient, Raman gain coefficient), insertion loss, and average amplifier gain noise figure by minimizing the error between estimated and measured output power spectrum and OSNR at the pre-amplifier of the OMS, however this method assumes all EDFAs have the same gain spectrum. It should be noted that both [3] and [15] methods additionally assume that OSNR can be measured, e.g., with an Optical Spectrum Analyzer (OSA), which is usually not possible in transmission systems except during initial commissioning.

In our previous work [85, 151], as well as in this paper, we leverage Optical Channel Monitors (OCMs) only, which return per-channel optical power only at the beginning and end of each OMS. Specifically, in [85] we applied a gradient descent method to refine connector insertion losses and amplifier gain spectra by minimizing the estimation error of power spectrum(measured by OCM) at the end of each OMS in C-band networks, thereby enabling accurate QoT estimation. Then, in [151], we used a gradient method to upgrade the insertion loss and amplifier gain spectrum refinement technique from C to C+L networks, leveraging the high SRS effect in such multi-band networks, achieving accurate GSNR estimation and showing that inaccurate insertion loss estimation can cause large QoT prediction error. In [87], we combined insertion loss refinement from [85] and a neural network-based EDFA gain spectrum prediction tool to predict the per-channel power variation when adding or dropping services. In [3, 15, 85, 87, 151], multiple unknown parameters are refined simultaneously without per-span monitoring and per-span accuracy of the refined parameters is not achieved. In [163], per-span OCM is assumed to be available and per-span insertion loss can be estimated accurately, assuming ideal, ripple-less amplifier gain spectra; but per-span OCM is not available in all networks, and the ripple-less spectra assumption triggers up to 1.5 dB GSNR estimation error.

Our proposed AIR technique involves active adjustments of the nominal gain of each amplifier to alter the SRS of the corresponding span; the SRS-induced power variation is then detected at the end of each OMS by an OCM to achieve per-span insertion loss estimation accuracy, enabling the detection and localization of anomalous insertion losses (which [3, 15, 85, 87, 151] do not achieve). Compared to [163] that requires OCM for each span, AIR requires only software modifications to the network controller and does not require new hardware, making it amenable to deployment in existing networks. Additionally, this method can be applied to generic single-band and multi-band systems (validated in **??**).

In this work, we consider fully ASE-noise-loaded systems to stabilize the amplifiers and emulate end-of-life conditions [19, 44].

4.2.3. Contributions

We first proposed the AIR technique in OFC 2024 paper [154]. As a reminder, in [154]:

- We proposed the AIR method and validated it experimentally in a single C-band network;
- We demonstrated the ability of AIR to estimate accurately the insertion losses at each connector, thus enabling detection and localization of the anomaly losses;
- We demonstrated that AIR enhances the QoT optimization and achieves larger SNR margins;
- We showed the temporary SNR variation induced by AIR can be controlled and well predicted in the C-band network.

We contribute here with the following extensions:

- We provide an updated and more complete description of the AIR method (Section 4.3).
- We extend our AIR technique to both C and C+L network and validate it by simulations based on the topology of a European network with 30 OMSs for both C-band (Section **??**) and C+L networks (Section **??**);
- We explore the impact of amplifier gain change value on the performance of insertion loss estimation, QoT optimization, and QoT prediction with AIR (Section 4.5);
- We validate with extensive simulations that the temporary GSNR variation induced by AIR can be accurately predicted in both C (Section **??**) and C+L networks (Section **??**).

In particular, Section 4.5 is completely new.

The rest of the paper is organized as follows. In Section 4.3, we introduce the proposed AIR method for insertion loss estimation. In Section 4.4, we introduce our framework for DT-based QoT optimization in optical networks, which leverages the proposed AIR. In Section 4.5, we evaluate the performance of the proposed method in terms of insertion loss estimation, QoT optimization and prediction using simulations on a European network topology, for both C-band and C+L networks. In Section 4.6, we experimentally evaluate the performance of insertion loss estimation and demonstrate the QoT optimiza-

tion enhancement with AIR. In Section 4.7, we discussed the application conditions and challenges of AIR method. In Section 4.8, we draw the conclusion of our study.

4.3. AIR Method Description

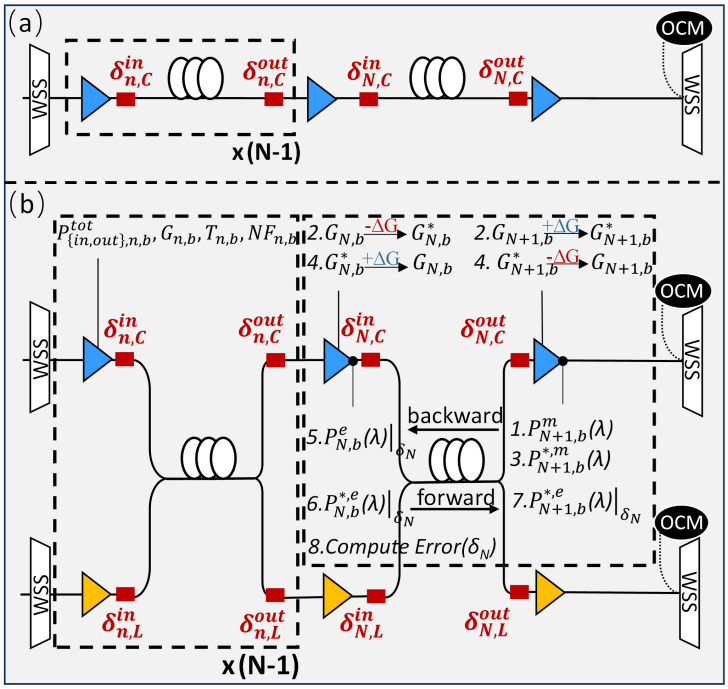


Figure 4.1: Generic N-span OMS topology in a) C and b) C+L networks.

The proposed AIR method is applicable to both single and multiband OMSs, as shown infig. 4.1(a) for C-band, and (b) for C+L-band N-span OMSs. Thereafter, the word "spectrum" indicates wavelength dependence. The gain $G_{(n,b)}$ and tilt $T_{(n,b)}$ settings are known for each amplifier, where $n \in \{1, \ldots, N+1\}$ indicates the index of the amplifiers in an OMS, and $b \in \{C, L\}$ indicates the band. The noise figure of each amplifier $NF_{(n,b)}$ can be obtained from a look-up table for a selection of $(G_{(n,b)}, T_{(n,b)})$ pair calibrated during the fabrication process. The total input and output powers $P^{tot}_{\{in,out\},n,b}$ at each amplifier are monitored by photodiodes integrated into the amplifier. The output power spectrum $P^{m}_{(n,b)}(\cdot)$ is typically monitored (denoted as 'm') only at the first ($n = 1$) and last amplifiers ($n = N+1$) by an OCM. The output power spectra $P^{e}_{(n,b)}(\cdot)$ of in-line amplifiers $n = 2, \ldots, N$ are unknown due to lack of monitoring and need to be estimated (noted as 'e'). Fiber characteristics, such as the (wavelength-dependent) attenuation coefficient α and fiber length L, are assumed to be known. The connector insertion losses at each band b at the input and output of each fiber span, $\delta^{in}_{(n,b)}$ and $\delta^{out}_{(n,b)}$, cannot be monitored

and need to be estimated. The gain spectrum of each amplifier is unknown due to lack of monitoring of the input power spectrum. However, the full-load gain spectrum of each amplifier $G^{cal}_{(n,b)}(G_{(n,b)},\cdot)$ can be calibrated during the amplifier fabrication process by inputting a flat input power spectrum, and monitoring the output power spectrum with different $G_{(n,b)}$. It should be noted that $G^{cal}_{(n,b)}(G_{(n,b)},\cdot)$ cannot be exactly the same but only an estimated version of the actual amplifier gain spectrum because the input power spectra are not always flat in real networks. Parameters with a '*', i.e., $G^{*}_{(n,b)}$, $P^{(*,e)}_{(n,b)}(\lambda)$, $P^{(*,m)}_{(n,b)}(\cdot)$, correspond to parameter values after adjusting amplifier gain during AIR. ΔG represents the gain variation value during AIR. We apply the SRS triangular approximation model in AIR, as it is demonstrated valid for C+L networks (bandwidth < 13.2 THz) [10].

The proposed AIR algorithm consists of 9 iterated steps for each OMS which are indicated infig. 4.1(b) and described below. Steps 1-4 involve hardware settings changes and data collection, while steps 5-9 involve DT-enabled (software) computations:

Step 1: Monitor the output power spectrum of the last amplifier for each band $P^{m}_{(N+1,b)}(\cdot)$.

For each span n (from the last to the first span of the OMS), iterate steps 2 to 4:

Step 2: Change the nominal gain of amplifier n (the amplifier before the nth fiber span) by $-\Delta G$ to $G^{*}_{(n,b)} = G_{(n,b)} - \Delta G$, and simultaneously change nominal gain of amplifier $n+1$ (the amplifier after the nth fiber span) by $+\Delta G$ to $G^{*}_{(n+1,b)} = G_{(n+1,b)} + \Delta G$. The gain change at amplifier n forces the launch power into span n to change by $-\Delta G$, hence altering SRS. The gain change of amplifier $n+1$ compensates for the total power change and isolates all variations to a single span, in order to minimize SNR variations of the existing services.

Step 3: After changing the gains of the two amplifiers, monitor the output power spectrum of the last amplifier of each band $P^{(*,m)}_{(N+1,b)}(\cdot)$.

Step 4: Revert the nominal gain of amplifiers n and $n+1$ to their original settings.

For each insertion loss combination $\delta_n = (\delta^{in}_{(n,b)}, \delta^{out}_{(n,b)})$ in a predefined list of insertion loss combinations

$$\{(\delta^{in}_{(n,b)} = 0,\ \delta^{out}_{(n,b)} = \delta^{tot}_{(n,b)}), \ldots, (\delta^{in}_{(n,b)} = \delta^{tot}_{(n,b)},\ \delta^{out}_{(n,b)} = 0)\},$$

where $\delta^{tot}_{(n,b)} = \delta^{in}_{(n,b)} + \delta^{out}_{(n,b)}$ is the total connector loss for span n and band b, which is obtained by subtracting the fiber Wavelength Dependent Loss (WDL) from the total span loss (known from the photodiodes located at amplifier's input and output), iterate steps

5 to 8:

Step 5: Estimate output power spectrum $P^{e}_{(n,b)}(\cdot)$ at amplifier n by backward propagation. The backward propagation starts from the output power spectrum of the last amplifier $N+1$: $P^{m}_{(N+1,b)}(\cdot)$ to the estimated input power spectrum of amplifier n: $P^{e}_{(n,b)}(\cdot)$. This estimation involves fiber wavelength dependent loss $WDL_n(\cdot)$ and wavelength-dependent SRS effect $SRS_n(\delta_n,\cdot)$ on power at span n, dependent on the assumed insertion losses δ_n. The backward propagation can be represented as (in linear scale):

$$P^{e}_{(n,b)}(\lambda) = \prod_{k=N}^{n} \Big[P^{m}_{(k+1,b)}(\lambda)\ SRS^{-1}(\delta_k,\lambda)\ WDL_k^{-1}(\lambda)\ G^{cal,-1}_{(k+1,b)}(G_{(k+1,b)},\lambda) \Big]. \tag{4.1}$$

Step 6: Estimate spectrum $P^{(*,e)}_{(n,b)}(\cdot)$ at amplifier n as (linear scale):

$$P^{(*,e)}_{n}(\lambda) = P^{e}_{n}(\lambda)\ \frac{G^{cal}_{(n,b)}(G_{(n,b)},\lambda)}{G^{cal}_{(n,b)}(G^{*}_{(n,b)},\lambda)}. \tag{4.2}$$

Step 7: Estimate spectrum $P^{(*,e)}_{(N+1,b)}(\lambda)$ at the end of the OMS by forward propagation (linear scale):

$$P^{(*,e)}_{(N+1,b)}(\lambda) = \prod_{k=n}^{N} \Big[P^{(*,e)}_{(k,b)}(\lambda)\ SRS_k(\delta_k,\lambda)\ WDL_k(\lambda)\ G^{cal}_{(k+1,b)}(G_{(k+1,b)},\lambda) \Big]. \tag{4.3}$$

Step 8: Compute the error function with assumed δ_n (in dB):

$$Error(\delta_n) = \sum_{b} \sum_{\lambda} \Big(P^{(*,e)}_{(N+1,b)}(\lambda) - P^{(*,m)}_{(N+1,b)}(\lambda) \Big)^2. \tag{4.4}$$

Step 9: The refined insertion losses at span n are then obtained by:

$$\delta_n^{refined} = \arg\min_{\delta_n} Error(\delta_n). \tag{4.5}$$

After refining insertion losses of all the spans in the OMS, the gain spectra of amplifiers in the OMS are refined using the gain refinement technique in [85].

4.4. QoT Optimization Leveraging Inputs Refinement

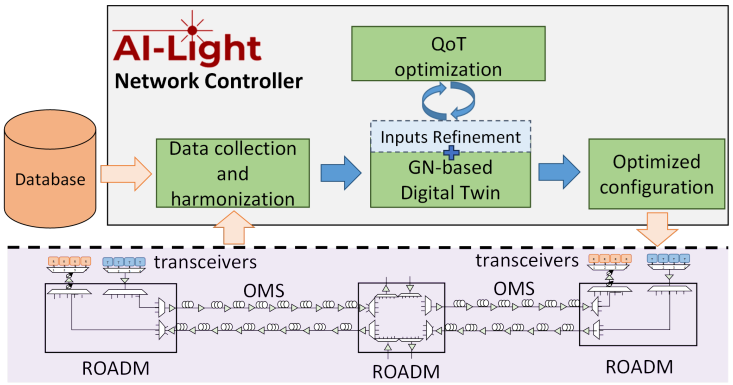


Figure 4.2: DT-enabled QoT optimization Framework.

Fig. 4.2 illustrates the framework for QoT optimization using our AI-Light Software-Defined Network (SDN) platform. The process begins with the collection of "known" parameters from both the network database (i.e., fiber types, fiber lengths, noise figure look-up table, etc.) and the real network monitoring (i.e., amplifiers' gain and tilt settings, total output power, OCM power spectra, etc.). Then, IR techniques are applied to estimate "unknown" parameters, such as insertion losses (by AIR) and amplifier gain spectra (by PIR). Moreover, the "known" parameters, along with the estimated "unknown" parameters are then given as input parameters for a GN-based DT (works similarly to GNPy [40]) to optimize and predict QoT of services.

In this study, we refer QoT optimization as the process of adjusting, on each OMS 1) the amplifier's gain and tilt settings [13, 39, 70]), and 2) the per-channel launch power at the first amplifier (booster) (by appropriately adjusting the per-channel attenuation of the Wavelength Selective Switch (WSS) at the start of each OMS [48, 107, 123, 150, 160]). The optimization process of the end-to-end services' QoT can be conducted in parallel through OMS-wide optimization. This means that the optimum design parameters, such as the amplifier gain and tilt settings, as well as launch power spectrum at booster amplifier, are computed in parallel by the DT for each OMS based on the applied optimization method, ensuring that the per-channel GSNR of the crossed OMSs, excluding the transponder's performance from SNR, is optimized.

For each OMS, the optimal amplifier gain and tilt are set based on the Local Optimization Global Optimization (LOGO) [101] algorithm combined with pre-emphasis to compensate the SRS effect [148] to optimize the launch power per span to enhance capacity in the network. Then, WSS per-channel attenuation is subsequently adjust to flatten the GSNR

to maximize the lowest GSNR across all services crossing the OMS, i.e., we optimize the "GSNR margin", to move away from the services' FEC limits to enhance the robustness in the network [33]. Both the amplifier and WSS settings optimization rely on accurate inputs to DT.

Moreover, optimum QoT can be predicted with the DT-computed design parameters. The DT with accurate inputs predicts accurately QoT before configuring the network; otherwise, inaccurate inputs can cause service outage due to incorrect DT-computed designs.

Finally, the DT-computed design parameters are configured in the physical network.

4.5. Simulation Validation for AIR

In this study, we compare the proposed AIR method with 2 baseline methods: Passive Inputs Refinement (PIR), and All monitoring Information (All Info).

PIR: We apply our previous work on passive inputs refinement, which is based on the gradient descent method to refine connector insertion losses and amplifier gain spectra based on the monitoring information from the current network state (without actively changing amplifiers gains). This process minimizes the estimation error of power spectrum at the end of each OMS, as described in [85] for C network and [151] for C+L network. PIR estimates overall insertion losses and amplifier gain spectra at OMS level (i.e., the estimation of QoT metrics such as (G)SNR will be correct after each OMS, as reported earlier), however, PIR does not achieve per-span accuracy.

All Info: This is an ideal scenario where all monitored and to-be-estimated parameters are assumed to be measurable in the lab. However, in real networks, this is difficult to achieve due to lack of monitoring. We validate the methods using simulation on a European country-sized network topology. The network comprises 30 unidirectional OMSs and 104 Standard Single Mode Fiber (SSMF) spans.

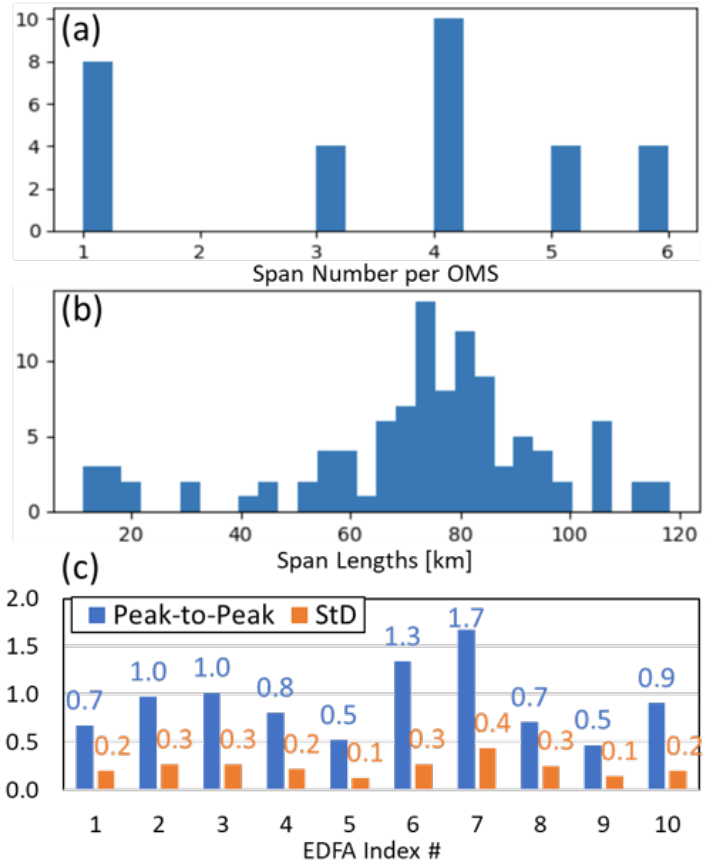


Figure 4.3: a) Histogram of number of spans per OMS, b) histogram of fiber lengths in the considered network, and c) amplitude (i.e., range width) and standard deviation of the gain ripple of each amplifier.

To maintain confidentiality, we do not report the full details of the topology, however, we provide aggregated topological statistics infig. 4.3, that reports the histograms a) of the number of spans per OMS and b) of the fiber lengths of each span. Each OMS consists of 1 to 6 spans. Across the 104 fiber spans, fiber lengths are highly heterogeneous, with the shortest span being 11 km, the longest span being 118 km, and the average span length being 73 km.

For each span and each band, the connector insertion losses $\delta^{in}_{(n,b)}$ and $\delta^{out}_{(n,b)}$ are randomly generated with a uniform distribution between 0 and 5 dB. The launch power spectrum of the booster amplifier of each OMS is set to be flat at fiber input, with the total power calculated by LOGO [101]. The nominal gain of each amplifier is set to compensate the span loss per span and per band. The noise figure spectra are considered flat at 4.5/5.5 dB for C/L band. The gain ripples of each amplifier are randomly selected from a list of 10 representative EDFAs measurements during the experiment in Section 5.fig. 4.3(c)

shows the amplitude (i.e., range width) and Standard Deviation (StD) of the gain ripple of each amplifier, defined as the difference between the measured gain spectrum and a gain spectrum with nominal gain setting and a linear tilt equal to the nominal tilt setting. The results show significant heterogeneity among amplifiers, with ripple amplitude ranging from 0.5 to 1.7 dB and standard deviations ranging from 0.1 to 0.4 dB.

4.5.1. C-band Network

In the C-band study, we validate the performance of the insertion loss estimation with PIR [85] and AIR (with varied ΔG) and we compare the performance of QoT optimization and QoT prediction with PIR, AIR, and All Info. Furthermore, we show that the temporary QoT variation induced by AIR can be controlled and accurately predicted.

4.5.1.1. Insertion Loss Estimation

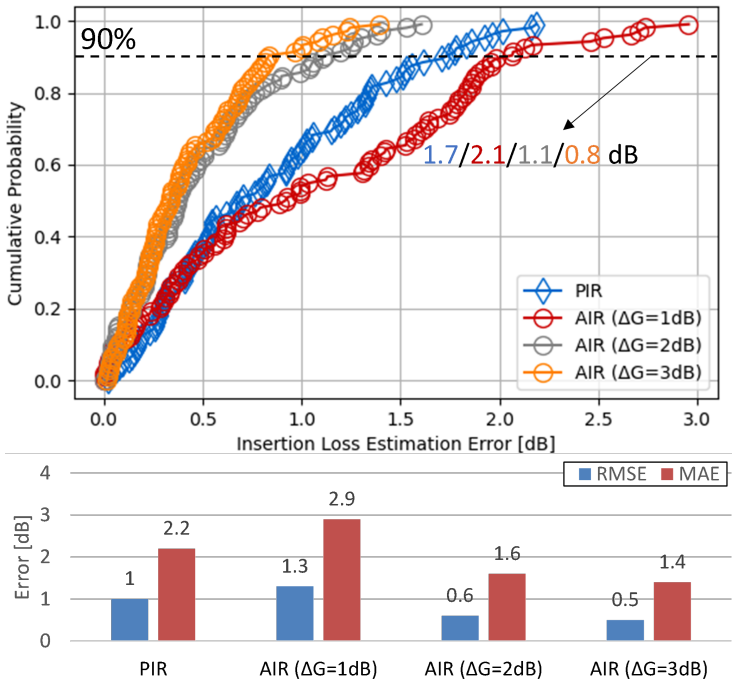


Figure 4.4: Insertion loss estimation in a C network.

Fig. 4.4 shows the Cumulative Distribution Function (CDF) of insertion loss estimation errors over all 104 spans. Different markers indicate different methods. For AIR, we compare three different gain variations during the AIR process, corresponding to $\Delta G = 1, 2, 3$ dB.

The results indicate that AIR with $\Delta G = 1/2/3$ dB estimates insertion losses more

accurately as ΔG increases, showing lower Root-Mean-Square Error (RMSE) values of 1.3/0.6/0.5 dB and Maximum Absolute Error (MAE) values of 2.9/1.6/1.4 dB compared to the PIR, which exhibits RMSE/MAE values of 1.0/2.2 dB.

AIR with larger ΔG estimates insertion losses more accurately due to the more significant SRS variations induced by the active amplifier gain changes. With $\Delta G = 1$ dB, AIR estimates less accurate insertion losses compared to PIR due to not evident SRS variation induced by the 1 dB amplifier gain change, thus the detected power variation by OCM is noised by the error of the calibrated amplifier gain spectrum. When $\Delta G \geq 2$ dB, AIR outperforms PIR for both MAE and RMSE.

The black dashed line represents the 90% threshold for insertion loss estimation error. It is observed that with AIR at $\Delta G = 3$ dB, 90% of the connector insertion losses can be estimated accurately with an error of less than 0.8 dB. When $\Delta G \geq 2$ dB, AIR outperforms PIR, where the 90% error reaches up to 1.7 dB.

4.5.1.2. GSNR Margin Optimization

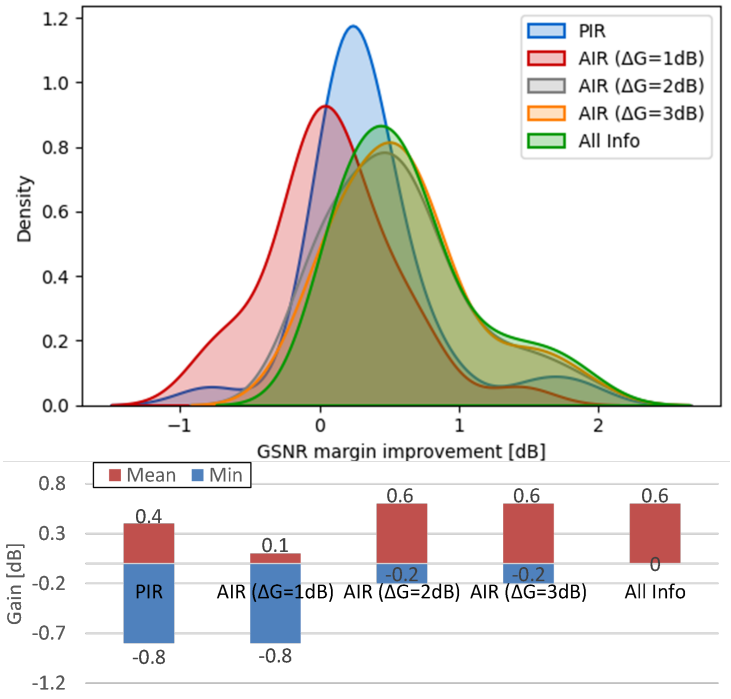


Figure 4.5: GSNR margin improvement in a C network.

In this section, we conducted the QoT optimization for each OMS in parallel (presented in Section 4.4) to adjust the amplifier gain, tilt, and booster power spectrum.fig. 4.5 shows the Probability Density Function (PDF) of GSNR margin gain compared to before

optimization by different methods over all 30 OMSs, with the histogram below indicating the minimum and average GSNR margin improvements.

With inaccurate per-span estimated insertion losses from the PIR method, incorrect parameters (launch power spectrum, amplifier gain, and tilt) are computed in the DT and subsequently reconfigured in the physical network. This results in up to 0.8 dB GSNR margin degradation, i.e., the worst (across all services going through the OMS) GSNR of at least one OMS degrades by 0.8 dB, possibly jeopardizing the services crossing this OMS if they are too close to the FEC limit.

With $\Delta G = 1$ dB, AIR performs similarly as PIR due to the weak SRS effect as explained in Section 4.5.1.1. However, when $\Delta G = 2$ or 3 dB, AIR significantly improves the GSNR margin compared to PIR. The GSNR margin degradation due to incorrect estimated inputs is reduced to only 0.2 dB, and the mean GSNR margin gain among all OMSs is improved to 0.6 dB, achieving the same average gain value as with the All Info method.

Hence, accurate estimated input parameters by AIR can substantially enhance the GSNR margin during the power re-optimization process compared to the PIR methods when $\Delta G \geq 2$ dB.

4.5.1.3. GSNR Prediction

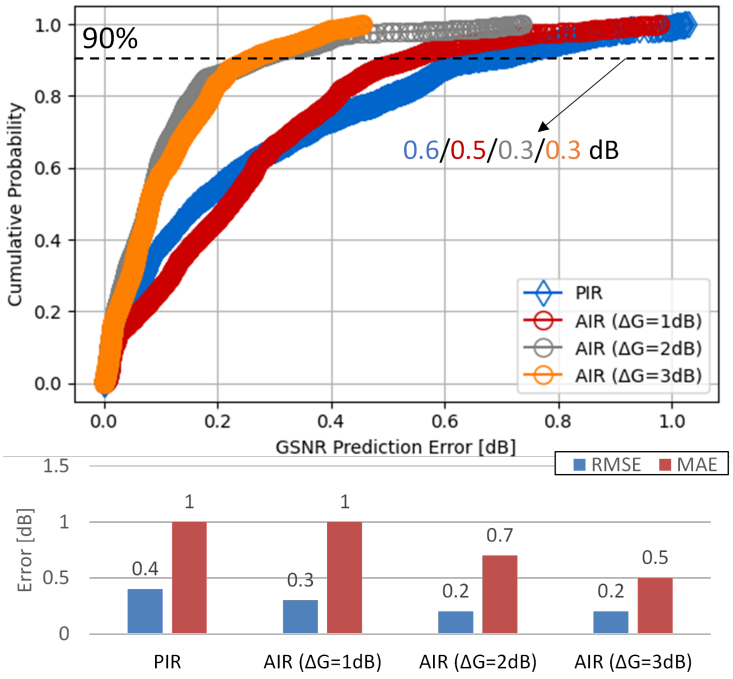


Figure 4.6: GSNR prediction in a C network.

Even in a fully (ASE-)loaded network, services' GSNR may vary due to physical layer reconfigurations (e.g., WSS adjustment for power re-optimization). Hence, accurate GSNR prediction is crucial for ensuring network reliability even in the full-load case. Accurate GSNR prediction requires accurate inputs to the GN-based DT, as inaccurate inputs can lead to incorrect computations by the digital twin, resulting in QoT degradation, as previously shown.

We simulated the power re-optimization of 30 OMSs and assessed the accuracy of the predicted GSNR after the re-optimization, given the network state before the re-optimization.fig. 4.6 shows the CDF of GSNR prediction error across all 30 OMSs, comprising 2400 samples (30×80 channels/OMS). The results indicate that the estimated insertion losses from the AIR method lead to superior GSNR prediction accuracy compared to the inaccurate estimated insertion losses from the PIR method. Notably, larger ΔG values result in better prediction performance, with AIR for $\Delta G = 3$ dB achieving the best GSNR prediction accuracy with RMSE/MAE values of 0.2/0.5 dB. This is a significant improvement over the PIR method, which has RMSE/MAE values of 0.4/1 dB.

Furthermore, AIR with $\Delta G = 2$ or 3 dB achieves a 90% GSNR prediction error of less than 0.3 dB. These findings demonstrate that AIR significantly enhances GSNR prediction accuracy due to the accurate estimation of insertion losses and gain spectrum at each span.

4.5.1.4. GSNR Variation During AIR

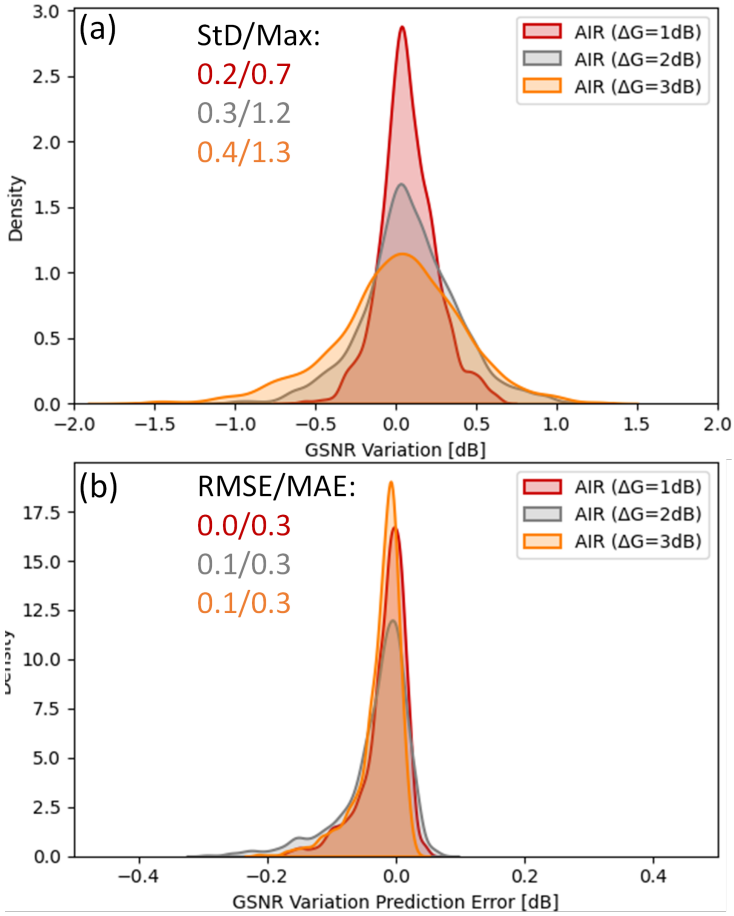


Figure 4.7: (a) GSNR variation in a C network; (b) GSNR variation prediction error in a C network.

As described in Section 4.3, the mechanism of AIR involves adjusting the nominal gain of amplifiers to alter the launch power into a single span, thereby altering SRS, and hence GSNR (of OMS) and SNR (of services). During the AIR process (Section 4.3, Steps 1-4), this can lead to a temporary variation of GSNR. To mitigate the impact on real-time services' QoT, the nominal gain of the nth and $(n+1)$th amplifier are adjusted simultaneously to compensate the total power change induced by the nth amplifier's gain change. Despite such mitigation, a single-span physical layer change still impacts OMS-level and end-to-end QoT, which we quantify here.

Fig. 4.7(a) shows the PDF of the GSNR variation when changing nth/n+1th amplifier's gain by $\mp\Delta G = 1, 2, 3$ dB. We report the standard deviation and maximum of GSNR variation. Larger gain changes induce larger GSNR variation, with a $\Delta G = 3$ dB gain change causing up to 1.3 dB GSNR variation and 0.4 dB StD. In case a service is close

to the FEC limit and AIR could jeopardize this service, PIR [85] could be first applied to refine the insertion losses and gain spectra, allowing the DT to roughly estimate the GSNR variation that would occur during AIR, before conducting AIR.

Accordingly, fig. 4.7(b) shows the PDF of the prediction error of the GSNR variation induced by $\Delta G \in \{1, 2, 3\}$ dB with the refined insertion losses and gain spectra from PIR. The GSNR variation can be accurately predicted with a MAE of less than 0.3 dB for all ΔG values. This accurate prediction of GSNR variation ensures the security and reliability of implementing the AIR technique in real networks, thereby avoiding disruptions of real-time services, especially in scenarios with small SNR margins.

4.5.2. C+L Multi-Band Network

In this subsection, we validated the applicability of the AIR technique for multi-band systems when the SRS effect is large. The complexity of running AIR in C+L networks is doubled compared to C-band networks, as it requires changing and monitoring components in both bands (e.g., amplifiers, OCMs). This increases the time required to apply AIR and introduces more synchronization challenges.

We validated the performance of insertion loss estimation, QoT optimization, and QoT prediction with PIR [151] and AIR. Furthermore, we demonstrate that temporary QoT variation induced by AIR can be controlled and well predicted.

4.5.2.1. Insertion Loss Estimation

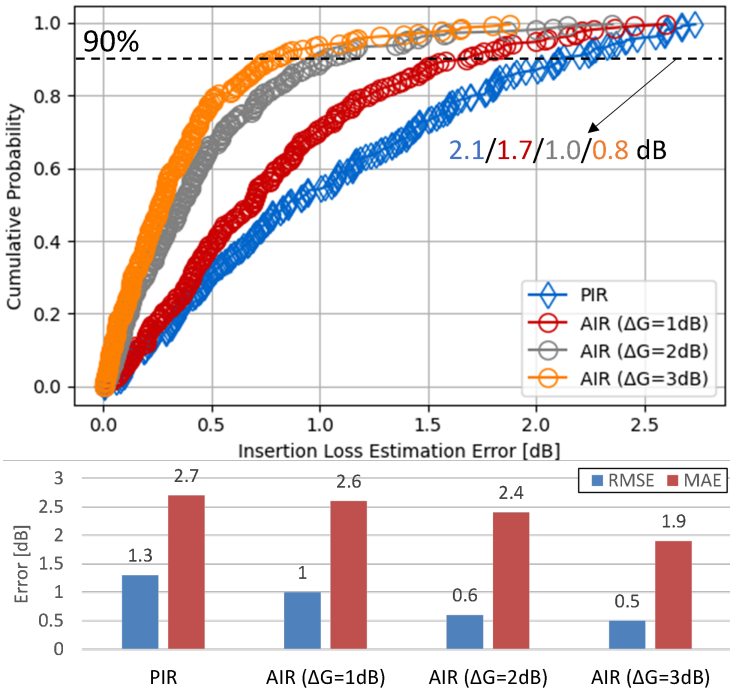


Figure 4.8: Insertion loss estimation in a C+L network.

Fig. 4.8 shows the CDF of insertion loss estimation error over all 104 spans. We can observe that AIR with ΔG = 1/2/3 dB estimates the insertion losses more accurately, with lower RMSE values of 1.0/0.6/0.5 dB and MAE values of 2.6/2.4/1.9 dB, compared to PIR with 1.3 dB RMSE and 2.7 dB MAE. PIR is less accurate (1.3/2.7 dB RMSE/MAE) for C+L networks compared with C-band networks (1/2.2 dB RMSE/MAE). The reason is that in C+L networks, for each span, different combinations of C- and L-band insertion losses can induce the same SRS effect, which makes PIR struggle. On the contrary, the stronger SRS effects in C+L networks help AIR, as SRS variations are more easily detected by the OCMs.

Note that uncertainty from the calibrated gain spectra degrades AIR performance in the C-band network for small ΔG (1 dB). AIR with larger ΔG better estimates the insertion losses thanks to more significant SRS variation. The black dashed line corresponds to the 90% quantile of insertion loss estimation error. We observe that with AIR at ΔG = 3 dB, 90% of connector insertion losses can be estimated with an error of less than 0.8 dB. This is significantly more accurate than PIR, where the 90% error reaches up to 2.1 dB. Hence, AIR can estimate insertion losses more accurately than PIR in C+L networks, particularly with larger ΔG values.

4.5.2.2. GSNR Margin Optimization

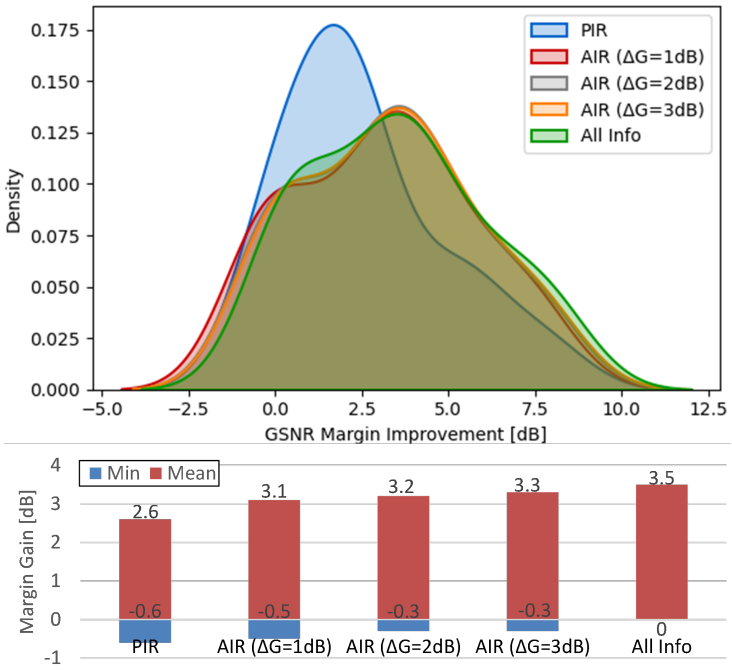


Figure 4.9: Insertion loss estimation in a C+L network.

Fig. 4.9 presents the PDF of GSNR margin gain across 30 OMSs in the C+L network, with the histogram below indicating the minimum and average GSNR margin improvements for different methods.

We can find that with per-span inaccurate estimated input parameters from PIR, configuring incorrect design parameters cause up to 0.6 dB GSNR margin degradation after optimization in the C+L network. In contrast, AIR can optimize the GSNR margin of OMSs where PIR fails. The GSNR margin degradation due to incorrect estimated inputs is reduced to 0.3 dB, and the average gain is improved to 3.3 dB, which is close to the average gain of 3.5 dB achieved by the All Info method.

We demonstrate that accurate inputs from AIR improve significantly GSNR margin compared to the PIR method.

4.5.2.3. GSNR Prediction

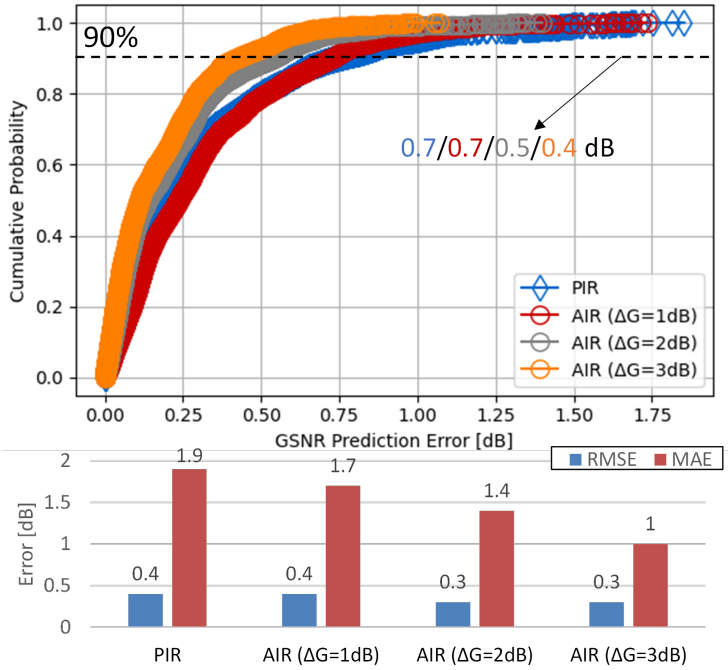


Figure 4.10: Insertion loss estimation in a C+L network.

Fig.4.10 shows the CDF of GSNR prediction error across 30 C+L OMSs, comprising 4800 samples (30 OMSs × (80 C + 80 L) channels/OMS). We observe that AIR achieves better GSNR prediction accuracy compared to PIR. Larger ΔG values result in better prediction performance, with AIR at $\Delta G = 3$ dB achieving the best GSNR prediction accuracy, with RMSE/MAE values of 0.3/1 dB. This represents an improvement over PIR, which exhibits 0.4/1.9 dB RMSE/MAE.

Moreover, AIR with $\Delta G = 3$ dB achieves a 90% GSNR prediction error of less than 0.4 dB, whereas PIR exhibits a larger 90% prediction error of up to 0.7 dB. These results demonstrate that AIR significantly improves GSNR prediction accuracy, owing to its more accurate per-span insertion loss estimation.

4.5.2.4. GSNR Variation During AIR

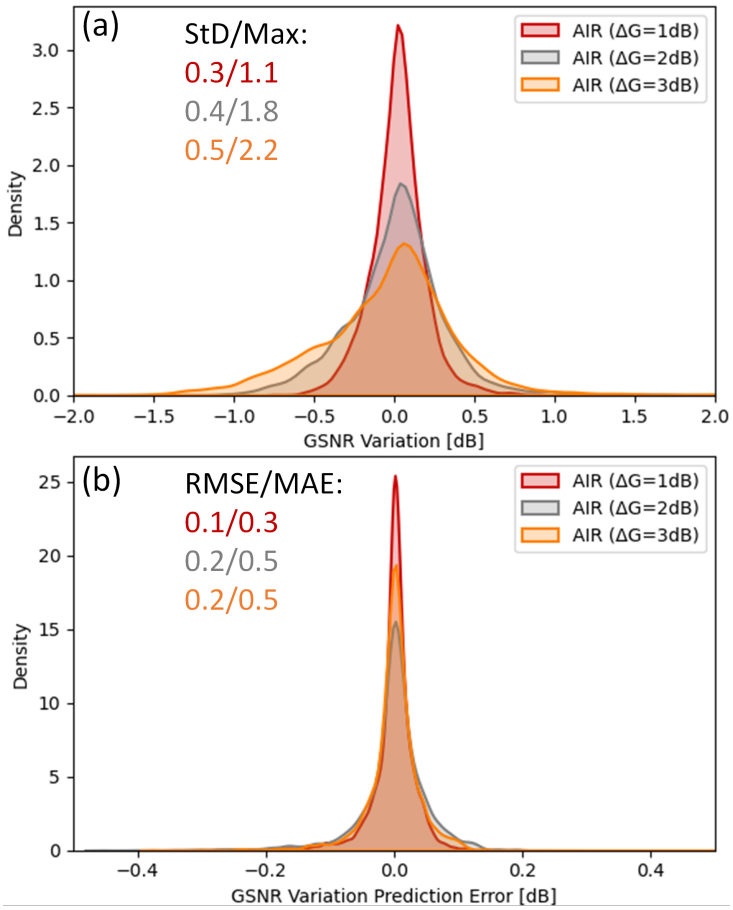


Figure 4.11: (a) GSNR variation in a C+L network; (b) GSNR variation prediction error in a C+L network.

Fig. 4.11(a) shows the PDF of the GSNR variation when changing the per-band $n^{\text{th}}/(n+1)^{\text{th}}$ amplifier's gain by $-/+\ \Delta G = 1, 2, 3$ dB in the C+L network. We observe that AIR with a large $\Delta G = 3$ dB can induce up to 2.2 dB GSNR variation and 0.5 dB StD, which is larger than in the C-band (1.3 dB maximum and 0.4 dB StD), owing to the stronger SRS effect. As before, PIR [**?**] is first applied to refine the insertion losses and gain spectra, allowing the DT to predict the GSNR variation before conducting AIR.

Fig. 4.11(b) shows the PDF of the prediction error with PIR for $\Delta G = 1, 2, 3$ dB. We observe that the GSNR variation can be accurately predicted with an MAE of 0.5 dB. This prediction accuracy ensures the security and reliability of implementing the AIR technique in real C+L networks, thereby minimizing the risk of disruptions to real-time services.

4.5.3. Robustness of Uncertainty of Power Monitoring and Fiber Attenuation Coefficient

We test the robustness of the AIR technique against two factors: 1) the uncertainty in channel power monitoring by the OCM, and 2) the uncertainty in the fiber attenuation coefficient.

4.5.4. Power Monitoring Noise

Compared to OSA, OCM provides a cost-effective solution for monitoring per-channel power in current networks by sacrificing monitoring accuracy in exchange for reduced cost. The inaccuracy of OCM power monitoring originates from integrated passive components (e.g., splitters) that must be characterized prior to deployment, with residual errors remaining even after characterization. In this study, we emulate the channel power uncertainty induced by OCM by generating a time-invariant monitoring error that follows a uniform distribution $U[-0.5, 0.5]$ or $U[-1, 1]$ dB for each channel (independently) of each OCM. We then evaluate the AIR performance (with $\Delta G = 3$ dB) through simulations in the C+L network.

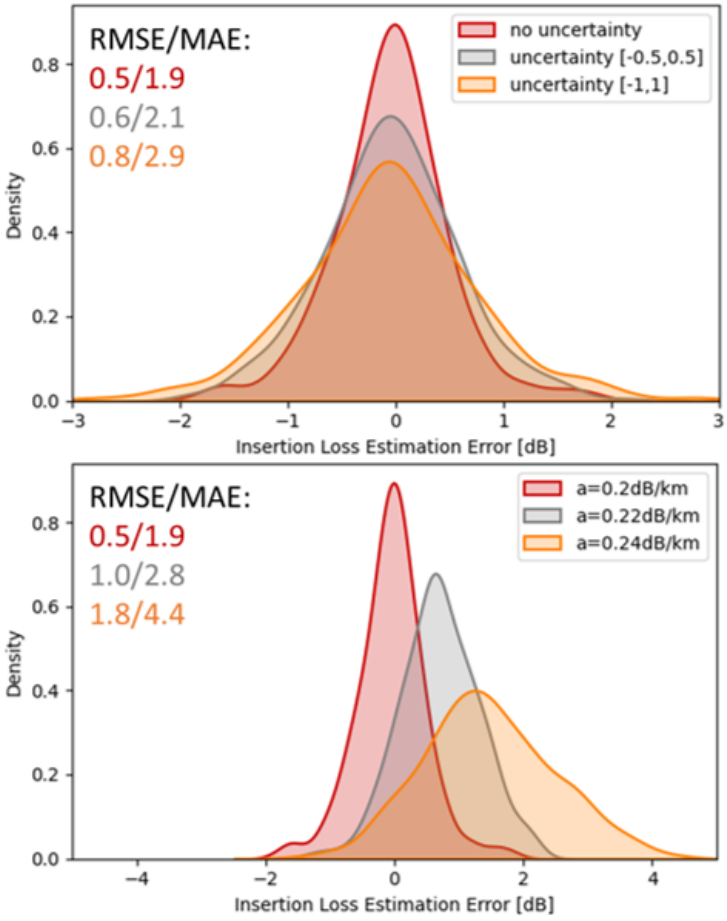


Figure 4.12: Insertion loss estimation error with (a) channel power uncertainty, and (b) fiber attenuation coefficient uncertainty.

Fig. 4.12(a) shows the PDF of the insertion loss estimation error under different ranges of power uncertainty. We observe that channel power uncertainty with a range of ±0.5 dB has a minor impact, degrading the RMSE/MAE by only 0.1/0.2 dB, whereas a range of ±1 dB has a more pronounced effect, degrading the RMSE/MAE by 0.3/1 dB. Notably, no large RMSE degradation is observed, indicating that AIR is generally robust to channel power uncertainty. This robustness arises because AIR relies on the *variation* of the SRS effect—rather than its absolute value—when amplifier parameters are adjusted.

4.6. Experimental Validation in a C-Band Network

We now experimentally validate our proposed AIR method in a C-band network testbed, and compare its performance with the PIR and All Info methods. We assess three key aspects: insertion loss estimation, SNR optimization and prediction. Moreover, we investigate the temporary SNR variation during the AIR process, demonstrating experimentally

that it can be addressed by the PIR technique with accurate prediction accuracy before conducting AIR.

4.6.1. Experimental Testbed

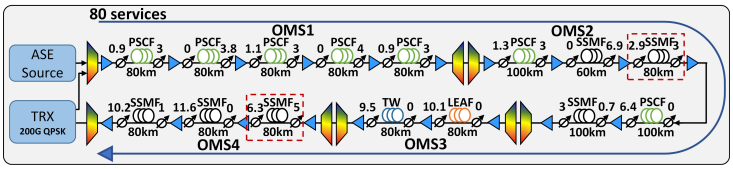


Figure 4.13: Tandem network testbed with 80 point-to-point services crossing 4 heterogeneous OMSs.

We experimentally validate the proposed AIR technique on a tandem network with four heterogeneous OMSs (OMS1–2–3–4), encompassing a total of 15 spans with varying fiber lengths (60, 80, and 100 km) and fiber types (SSMF, PSCF, TW, LEAF), as depicted in Fig. 4.13. At each span, a Variable Optical Attenuator (VOA) is placed before and/or after the fiber to emulate insertion losses, as indicated in Fig. 4.13 above each VOA. The VOA attenuation values before the fiber range from 0 to 5 dB, while the values after the fiber range from 3 to 11.6 dB, including a 3 dB coupler for per-span power spectrum monitoring (only used in the All Info case).

Eighty point-to-point services are loaded in the network, traversing all four OMSs. These services are emulated using an ASE source with 75 GHz channel spacing. The pre-FEC BER and SNR of seven services uniformly spread across the 6 THz C-band are monitored using a real-time 200 Gb/s PDM-QPSK commercial transponder.

In the initial network state, the configuration follows the setup in Section 4.5: the launch power spectrum is set to be flat at fiber input, with the total power calculated by LOGO [101]; the nominal gain of amplifiers is set to compensate for span loss; and amplifier tilt is configured to compensate for SRS tilt at each span. In this study, the nominal gain variation ΔG ranges from 2 to 3 dB per amplifier, depending on the available tuning margin.

4.6.2. Insertion Loss Estimation

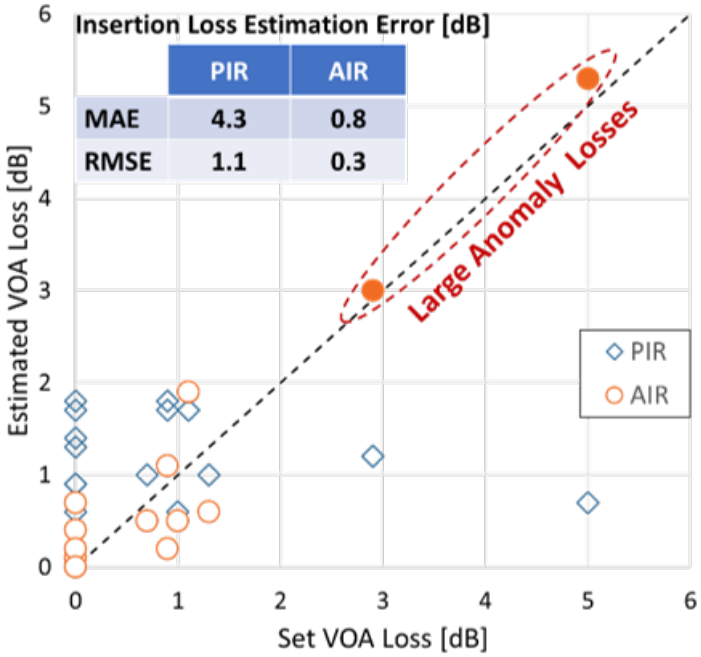


Figure 4.14: Insertion loss estimation (red dashed circle: anomaly detection and localization).

Fig. 4.14 presents the estimated insertion losses before each of the 15 spans, δ_n^{in}, obtained with AIR (orange circles) and PIR (blue diamonds). To test the localization ability of large anomalous losses with AIR, VOAs before the third span of OMS2 and the first span of OMS4 are set to 2.9 dB and 5 dB, respectively. The corresponding estimated losses are highlighted with solid orange disks. The inset table reports the MAE and RMSE of the loss estimation achieved with AIR and PIR. AIR shows a substantial improvement over PIR, reducing the MAE from 4.3 to 1.6 dB and the RMSE from 1.1 to 0.3 dB. Furthermore, AIR effectively identifies and localizes the anomalous insertion losses of 2.9 dB and 5 dB at the corresponding spans, as indicated by the red dashed circles.

4.6.3. Impact of Insertion Loss Estimation on QoT Estimation, Prediction, and Optimization

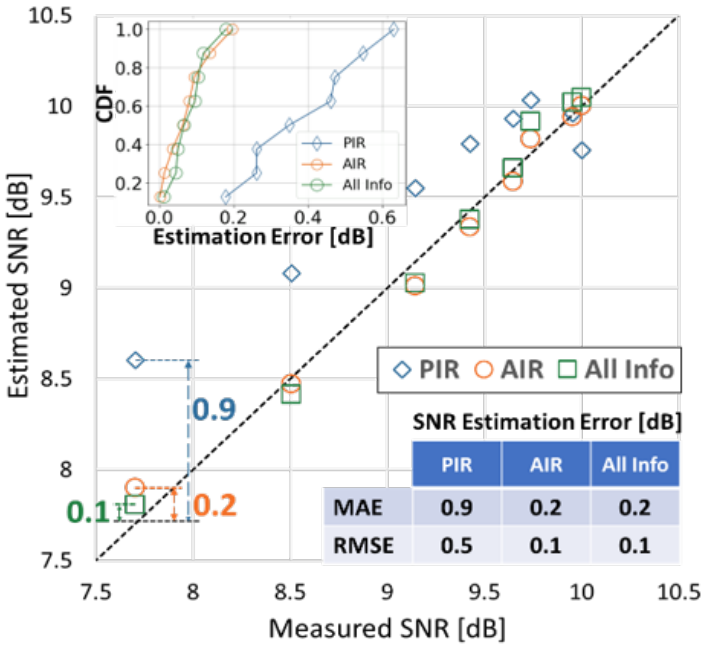


Figure 4.15: SNR estimation accuracy.

Fig. 4.15 shows the SNR estimation accuracy at the initial network state using the GN-based DT with inputs from three different methods: PIR (blue), AIR (orange), and All Info (green). The inset plot (top left) presents the CDF of the estimation error, highlighting that AIR improves SNR estimation accuracy compared to our state-of-the-art baseline PIR (which itself already outperforms simpler digital twins such as GNPy that lack parameter refinement). Remarkably, AIR achieves the same SNR estimation accuracy as the All Info case, which would only be achievable with unrealistic full monitoring capability, thanks to its accurate estimation of per-span insertion losses.

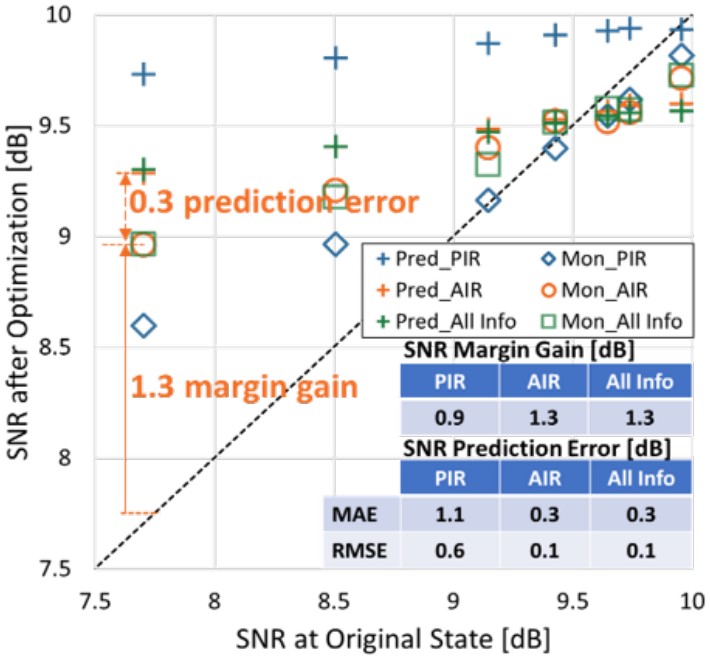


Figure 4.16: SNR optimization with predicted SNR and monitored SNR.

Fig. 4.16 shows the SNR optimization results obtained with the GN-based DT when insertion losses are estimated using PIR, AIR, and All Info. The same amplifier gain/tilt and launch power spectrum optimization strategy described in Section 4.4 is applied. The x-axis shows the monitored SNR at the initial network state, while the y-axis reports the DT-predicted optimized SNRs (denoted as "Pred_X" for each method X) and the monitored optimized SNRs after applying the corresponding DT-computed parameters in the network ("Mon_X"). The inset table summarizes the SNR margin improvement, defined as the SNR improvement of the worst-performing service. AIR improves the network margin by 0.4 dB compared to PIR, reaching the same level as All Info thanks to accurate per-span insertion loss estimation. In contrast, incorrect inputs from PIR can yield prediction errors of up to 1.1 dB, whereas AIR substantially enhances prediction accuracy, achieving MAE and RMSE values of 0.3 and 0.1 dB, respectively—matching the accuracy of All Info. These results demonstrate that AIR strengthens the accuracy of the digital twin and thereby enhances the reliability and efficiency of the QoT optimization process.

4.6.4. SNR Variation During AIR

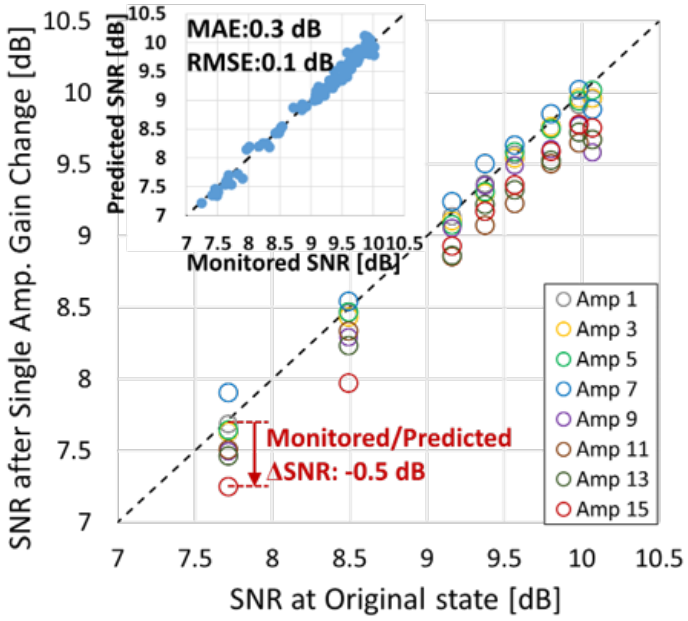


Figure 4.17: Monitored and predicted varied SNR after gain change of each amplifier pair during AIR process.

During the AIR process, the nominal gain of each amplifier is varied by up to 3 dB to induce SRS variations. This procedure may cause temporary SNR fluctuations of existing services. Fig. 4.17 illustrates the SNR variation observed during the simultaneous adjustment of the nth and $(n+1)$th amplifier gains ($n = 1, \ldots, 15$). Across all 15 amplifier pairs, the maximum observed SNR degradation does not exceed 0.5 dB. The inset plot shows the prediction of SNR variation prior to AIR execution using PIR-refined parameters, demonstrating that the degradation can be accurately forecast with an RMSE of only 0.1 dB. These results confirm that AIR can be safely deployed in networks carrying live traffic, as the SNR margin remains acceptable during the process. Importantly, when accounting for the temporary 0.5 dB degradation and the permanent 1.3 dB SNR margin improvement achieved by QoT optimization, a net margin gain of 0.8 dB is realized with AIR-based insertion loss estimation.

4.7. Discussion on AIR Application Conditions and Limitations

The AIR technique is designed to estimate insertion losses and achieve span-level accuracy. Here, we discuss its challenges and application conditions:

4.7.1. Challenges

AIR relies on a reference gain spectrum, which can be calibrated during the fabrication process, and on the intensity of the SRS effect. Applying AIR in partially-loaded networks introduces several challenges:

1. **Reference Gain Spectrum Calibration:** In partially-loaded networks, the diversity of channel allocations and power levels complicates the pre-calibration of the reference gain spectrum. The method proposed in [141] addresses this issue by employing a machine-learning-based approach to predict the gain spectrum under partial loads. However, this solution requires a substantial training dataset, and the prediction accuracy must be sufficiently high to avoid introducing errors larger than the SRS-induced variations.

2. **Reduced SRS Effect:** With fewer channels, the SRS effect weakens, thereby reducing the accuracy of insertion loss estimation. Our observations in partially-loaded C-band networks confirm that AIR accuracy strongly correlates with channel load. Consequently, AIR is not recommended in lightly- or partially-loaded scenarios. A possible future direction is to exploit monitored power and SNR information to refine insertion loss estimates. However, care must be taken to avoid overfitting by inadvertently absorbing uncertainties from transponders, WSS, and other components into the insertion loss model.

3. **Uncertainty from Fiber Profile:** Variations in the fiber profile can lead to systematic overestimation of insertion losses by AIR. This challenge can be mitigated by first applying optical time-domain reflectometry (OTDR) and longitudinal power monitoring to identify and compensate anomalous losses caused by uncertain attenuation coefficients, as discussed in Section 4.5.3.

4. **Synchronization Between Amplifiers:** For each span, the gain adjustments of the paired amplifiers must be synchronized to prevent excessive SNR fluctuations. This can be effectively managed by incrementally adjusting the amplifier gain in small steps (e.g., 0.5 dB or less) until the desired ΔG target is reached, thereby

ensuring stable operation and avoiding service degradation.

4.7.2. Application Scenarios

Considering these limitations, we propose the following scenarios for applying AIR:

1. **Commissioning Stage:** AIR can be applied after the installation of optical components and prior to service deployment to estimate insertion losses and detect anomalies (e.g., dirty connectors). At this stage, an ASE source can be made available for both C- and C+L-band networks. Since services are not yet established, AIR can operate without inducing SNR variation.

2. **Network Maintenance:** AIR is also suitable during network maintenance operations. For example, in the event of a fiber cut, services in the affected OMS are already disrupted. AIR can thus be executed on the maintained OMSs without incurring additional SNR variation.

3. **Live Networks with Existing Services:** AIR is not recommended in partially- or lightly-loaded networks due to the weak SRS effect. However, in noise-loaded or highly-loaded networks where SRS is significant, AIR is applicable. While AIR may cause a slight and predictable GSNR penalty, it is triggered infrequently—typically in response to major events such as span power profile adjustments or service addition/removal—rather than at regular intervals. In dynamic environments such as spectrum-as-a-service models, AIR can still be applied: for a given OMS, AIR can be initiated, temporarily interrupted by service establishment, and resumed without loss of accuracy. Since each AIR step modifies and restores amplifier gains within a few seconds, the process remains compatible with networks where services are not provisioned more frequently than every few seconds.

The AIR framework can also be extended to systems with forward Raman amplifiers, but not with backward Raman amplifiers. In long-haul transmission systems, backward Raman amplifiers are typically deployed at the fiber end, introducing insertion losses at the output. Because AIR relies on the SRS effect, which is stronger at the fiber input, accurate loss estimation at the fiber end becomes challenging. For forward Raman amplifiers, AIR can still be applied by adjusting the Raman gain to detect power variations at the end of each OMS. This requires calibrated Raman gain spectra and accurate fiber characterization (e.g., attenuation coefficients, Raman gain efficiencies) to ensure precise insertion loss estimation. Care must also be taken to avoid large GSNR variations when using AIR in live networks. By addressing these factors, AIR can be extended to more complex network scenarios, including Raman-amplified spans.

4.8. Conclusions

We proposed a novel technique, called AIR, for accurate insertion loss estimation, QoT optimization and prediction in optical networks. AIR, by adjusting amplifier gains for active probing of SRS, significantly improves the accuracy of insertion loss estimations, which are critical for predicting and optimizing GSNR and SNR. We validated the method by simulations on a European C and C+L network with 30 OMSs, and also by experiments on a tandem C-band network with 4 OMSs in our lab. Results show that AIR substantially enhances insertion loss estimation, QoT optimization and prediction in optical networks. This advancement underscores the importance of accurate input parameter estimation for the performance and reliability of modern optical networks. The proposed methodology not only addresses the challenges posed by physical effects and network reconfigurations, but also provides a scalable solution requiring minimal monitoring hardware, paving the way for more robust and automated optical fiber networks capable of meeting the increasing data demands of 5G and 6G technologies.

5 | Input Refinement with Incremental Learning for Accurate Digital Twin-Enabled Self-Driven QoT Optimization in Optical Networks

5.1. Abstract

Reliable Quality of Transmission (QoT) prediction is essential to ensure that services operate near their optimal working point, maximizing network capacity and efficiency while avoiding large design margins. A major source of QoT prediction error lies in the uncertain modeling of nonlinear fiber impairments, particularly the Kerr effect and Stimulated Raman Scattering (SRS), which are difficult to monitor with existing hardware. Accurate modeling of these effects requires knowledge of fiber insertion loss. In addition, the gain spectrum of optical amplifiers, which governs Amplified Spontaneous Emission (ASE) noise is not directly monitored. Further uncertainties stem from service end-to-end (E2E) impairments, including Wavelength Selective Switch (WSS) filtering-induced noise and from device-specific back-to-back (B2B) transponder performance, both of which are typically unknown at deployment time. To address these challenges, we propose Incremental Learning-based Input Refinement (IIR), a parameter estimation method that leverages multiple network snapshots to jointly refine fiber insertion losses, amplifier gain spectra, and end-to-end offset noise (comprising WSS filtering and transponder B2B contributions). IIR is applied incrementally during routine, live network (re-)optimization, requiring no intrusive measurements. The proposed method is validated through (1) simulations using experimental data on a C-band ring network, and (2) experimental validation on a C-band mesh network. Results show that IIR significantly improves the estimation of key physical-layer parameters, enhancing QoT prediction accuracy and enabling effective

closed-loop power optimization.

5.2. Introduction

5.2.1. Motivation

Recent advancements in optical network monitoring are opening new opportunities for more effective Quality of Transmission (QoT) (re-) optimization. In optical networks, end-to-end (E2E) services are transmitted over multiple wavelengths and traverse several links or Optical Multiplex Sections (OMSs). The QoT of these services, typically quantified by Bit Error Rate (BER), Q-factor, or Signal-to-Noise Ratio (SNR), is influenced by various physical-layer impairments. Key contributors include fiber nonlinearities such as Kerr effects (including self-phase modulation, cross-phase modulation, and four-wave mixing) and Stimulated Raman Scattering (SRS), both of which are highly sensitive to the launch power into each fiber span. Additionally, Amplified Spontaneous Emission (ASE) noise, generated by Erbium-Doped Fiber Amplifiers (EDFAs) and determined by their gain and noise figure (NF) spectra, directly impacts the Optical SNR (OSNR). Other important impairments include Wavelength Selective Switch (WSS) filtering penalties and the back-to-back (B2B) performance of transponders, both of which can further degrade QoT.

To ensure reliable data transmission, service QoT must consistently remain above a required threshold. Specifically, the BER must stay below, and the SNR above, the Forward Error Correction (FEC) limit. However, service QoT can degrade over time due to (i) load-dependent effects, which vary when services are added or dropped [77, 150], and (ii) dirty or aged connectors, which affect both nonlinear impairments and ASE noise [153]. Consequently, automated network QoT optimization [13, 24, 39, 48, 78, 107, 150] at the physical layer is critical to maintain optimal service performance throughout the network's operational lifespan and prevent service outages.

Digital twin (DT) technology has recently emerged as a powerful tool for QoT prediction [35, 138] and optimization [77, 125]. A DT allows predictive modeling of network behavior under hypothetical configurations and supports what-if scenario analysis. For example, by simulating changes in booster (the first amplifier in an OMS) launch power spectrum, a DT can estimate the potential impact on service quality before the changes are implemented. This capability enables predictive and non-intrusive QoT optimization.

In this study, we adopt an analytical model-based digital twin, which offers greater transparency, explainability, and adaptability than neural network-based approaches [103, 105, 108, 118, 141, 148**?**]. Analytical models explicitly represent key physical-layer effects such

as SRS, ASE noise, Kerr nonlinearity, WSS filtering, and transponder B2B performance. The Gaussian Noise (GN) model [40, 101], extended to account for SRS, provides a computationally efficient and accurate framework [117]. However, the accuracy of such a DT strongly depends on the accuracy of its input parameters [41, 153]. When properly calibrated, the DT enables reliable QoT prediction and effective optimization. If the input parameters are inaccurate, optimization decisions may be suboptimal, resulting in degraded QoT and inefficient resource usage [102].

In practice, several input parameters are difficult to obtain due to limited monitoring capability, such as (i) fiber insertion losses, affecting power entering and propagating along the fiber, hence affecting Kerr and SRS effects; (ii) amplifier gain and NF spectra that affect the ASE noise modeling; and (iii) E2E offset noise from WSS filtering and transponder B2B performance. Inaccurate estimation of these parameters leads to unreliable QoT prediction and degraded optimization outcomes [79].

To overcome this challenge, network snapshots can serve as a valuable resource. These snapshots, collected by the network management system, represent distinct network states and include physical-layer data such as service information (i.e., routing table, rate), power spectra from Optical Channel Monitors (OCMs), total power readings from photodiodes (PDs) in EDFAs, and BER values observed at the receivers. However, improper use of snapshot data can compromise parameter estimation. For instance, in [85], refining insertion losses and amplifier gain spectra using only a single snapshot led to overfitting of nonlinear impairments. This caused transponder B2B noise and WSS penalties to be misinterpreted, resulting in underestimated insertion loss values.

To address this limitation, we propose a method called Incremental-learning-based Input Refinement (IIR). This technique uses multiple snapshots, collected during a multi-step power optimization process, to incrementally estimate fiber insertion loss, amplifier gain spectrum, and E2E offset noise. By capturing variations across snapshots, the IIR method improves estimation accuracy without overfitting. This allows the construction of a more accurate DT, capable of supporting self-driven QoT optimization in dynamic optical networks.

5.2.2. State of the Art

Table 5.1: Input parameter refinement techniques.

Ref. (band)	Main inputs and assumptions	Estimated Parameters
[3] (C)	Measured OSNR at OMS output	Insertion loss, amplifier noise figure spectrum
[15] (C)	Measured OSNR at OMS output, measured OMS output power spectrum, homogeneous rippled gain spectrum	Fiber parameters, insertion loss, average amplifier noise figure
[85] (C)	Measured output power spectrum at OMS	Insertion loss, amplifier gain spectrum
[151] (C+L)	Measured output power spectrum at OMS	Insertion loss, amplifier gain spectrum
[87] (C)	Measured output power spectrum at OMS, trained EDFA model	Insertion loss, amplifier gain spectrum
[163] (C+L)	Measured output power spectrum at each span, ripple-less gain spectrum	Insertion loss
[150] (C, C+L)	Measured output power spectrum at OMS, fully ASE-loaded system, calibrated full-load amplifier gain spectrum, possibility to adjust amplifier settings on-demand (the "active" part)	Insertion loss
[25] (C+L)	Measured output power spectrum at each span, fully ASE-loaded system	Insertion and splice loss
[161]	Measured input/output power spectrum at span with Raman amplifier	Output power spectrum with Raman amplifier
[IIR] (proposed, C)	Multi snapshots of measured output power spectrum at each OMS and service BER	Insertion loss, amplifier gain spectrum, E2E offset noise

Table 5.1 summarizes several existing techniques for input parameter refinement aimed at improving the accuracy of digital twin (DT) models for optical network optimization. The work in [3] proposed a Bayesian optimization-based algorithm to estimate fiber insertion losses and amplifier noise figures by minimizing the error in Optical Signal-to-Noise Ratio (OSNR) estimation. This method considers only ASE noise and does not account for nonlinear fiber noise, which limits its SNR prediction accuracy. In [15], a method was presented to jointly estimate fiber parameters, including effective area, attenuation coefficient, Raman gain coefficient, and insertion losses, along with the average amplifier noise figure. The approach modifies amplifier gain and tilt settings to minimize the discrepancy between estimated and measured output power spectra and OSNR at the pre-amplifier of each OMS. However, the method assumes homogeneous gain spectra across all EDFAs, which may not reflect real-world conditions.

Paper [161] proposes an input refinement paradigm that improves the accuracy of both physics-based and machine learning models for received power estimation after Raman amplifiers in dynamic C+L-band optical networks using particle swarm optimization. It is important to note that both methods in [3, 15, 161] require access to measured OSNR values, typically obtained via an Optical Spectrum Analyzer (OSA). Such measurements are generally not available in live transmission systems and are usually restricted to initial commissioning stages.

Our previous works [85, 151] leveraged OCMs, which provide per-channel optical power measurements at both the input and output of each Optical Multiplex Section (OMS), without the need for an OCM at each inline amplification site. In [85], we applied a gradient descent method to refine fiber insertion losses and amplifier gain spectra by minimizing the estimation error of the output power spectrum (measured by OCMs) in C-band networks, thereby enabling accurate QoT estimation. In [151], this approach was extended to C+L-band networks. By leveraging the stronger SRS effect in multi-band environments, we demonstrated that accurate insertion loss estimation is essential for prediction of Generalized SNR (GSNR), which accounts for ASE noise and Kerr nonlinearity but excludes transponder back-to-back noise. Consequently, GSNR can be evaluated at the OMS level. The study also showed that misestimation of insertion losses can result in large QoT prediction errors.

In [87], fiber insertion loss refinement from [85] was combined with a neural network-based EDFA gain spectrum prediction model to predict the per-channel power variation when adding or dropping services; note that the new proposed parameter refinement technique in this paper could also be combined with advanced EDFA models as in [87] to improve the SNR prediction scenario. In [153], amplifier gain settings were actively adjusted to induce

SRS-based power variation across spans. These variations were captured by OCMs and used to estimate per-span insertion losses and detect anomalies. However, this method depends heavily on the presence of a strong SRS effect and is therefore not well-suited to partial-load or low-load network scenarios.

The method proposed in [163] assumes the availability of per-span OCMs and ripple-free gain spectra to enable accurate per-span insertion loss estimation. However, such assumptions are often unrealistic, and ignoring spectral ripple can lead to GSNR estimation errors of up to 1.5 dB. Similarly, the method in [25] localizes splice loss using SRS effects in full-load C+L systems, but accuracy depends heavily on device characterization, particularly EDFA gain spectra.

To address these limitations, we propose the IIR method. IIR leverages multiple network snapshots that contain OCM-measured power spectra (at the input and output of each OMS) and BER (SNR) measurements from the receivers. The method sequentially refines amplifier gain spectra, fiber insertion losses, and E2E offset noise (resulting from WSS filtering penalties and transponder variability). This approach enables autonomous QoT optimization in partially loaded C-band mesh networks, without requiring per-span OCM monitoring or idealized amplifier assumptions.

5.2.3. Contributions

We first introduced the IIR method in our OFC 2025 paper [**?**], where:

- The IIR algorithm was proposed and validated through simulation using experimental data from [123], based on a C-band ring-topology network. For the sake of completeness, we develop the algorithm in this paper, in Section 2.
- It was shown that the accuracy of fiber insertion loss estimation improves with the number of available snapshots, enabling enhanced QoT prediction and optimization. This is reported in Section 3.

This paper extends our previous work with the following new contributions, reported in Section 4:

- We propose a self-driven QoT optimization framework, and experimentally validate the IIR method in a C-band mesh-topology network (Sections 4.1 and 4.2).
- We demonstrate that IIR enables a multi-step, closed-loop optimization process, in which each network reconfiguration step (e.g., WSS adjustment) generates a new snapshot. These successive snapshots are exploited by IIR to continuously

refine estimates of fiber insertion loss, amplifier gain spectra, and E2E offset noise. As a result, the DT becomes progressively more accurate, leading to continuous improvement in network margin (Sections 4.2 and 4.3).

Overall, this incremental refinement capability supports increasingly accurate and autonomous QoT optimization, enabling real-time decision-making in partially loaded mesh networks.

5.3. IIR Method Description

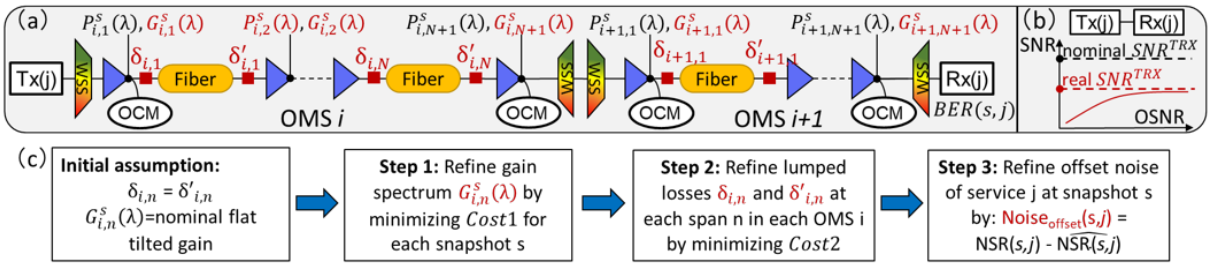


Figure 5.1: (a) Topology of OMS-based optical network and its parameters; (b) Transponder back-to-back limit; (c) Three-step IIR method.

Fig. 5.1(a) shows the topology of an OMS-based optical network. The variables $s/j/i/n$ represent the snapshot/service/OMS/span index, respectively. For example, in snapshot s, service j is transmitted by $Tx(j)$ and received by $Rx(j)$, passing through OMS i, with $BER(s,j)$ monitored by $Rx(j)$. The output power spectra at amplifiers $n = 1$ and $n = N + 1$ are monitored and known by OCM as $P^s_{(i,1)}(\lambda), P^s_{(i,N+1)}(\lambda)$. We use boldface notation for vectors and indicate wavelength-dependence and vector products are all element-wise.

The red parameters indicate unknown network parameters to be estimated by IIR, such as the (1) output power spectra of in-line amplifiers $P^s_{(i,n)}(\lambda)$, (2) gain spectra of all amplifiers $G^s_{(i,n)}(\lambda)$, and (3) the fiber insertion losses at the input/output $\delta_{(i,n)}/\delta'_{(i,n)}$ of each span.

Note that (1) and (2) vary across network snapshots (states). The total uncertain insertion loss of each span ($\delta^{\text{total}}_{(i,n)} = \delta_{(i,n)} + \delta'_{(i,n)}$) is known and calculated as span loss minus fiber loss, where span loss is monitored by amplifier photodiodes, and fiber loss is calculated from fiber length and attenuation coefficient. Noise figure spectrum is assumed known from a lookup table for each amplifier. Additionally, the transponder B2B noise can be represented by SNR^{TRX}, which is the maximum achievable SNR in a B2B configuration, as shown in Fig. 5.1(b). We only know the nominal SNR^{TRX} from datasheets while the

real SNR^{TRX} is difficult to pre-calibrate since it depends on both Tx and Rx, and their pairing is unknown before deployment. Therefore, SNR^{TRX} is also treated as an unknown for each transponder pair (service). All the known and unknown parameters are fed into the DT.

The monitored BER can be converted into equivalent SNR, and subsequently into a Noise-to-Signal Ratio (NSR). The NSR of service j at snapshot s, denoted as $NSR(s, j)$, is composed of multiple contributions:

$$NSR(s, j) = NSR^{ASE}(s, j) + NSR^{NLI}(s, j) + NSR^{TRX}(j) + FP(j) \tag{5.1}$$

Where:

- $NSR^{ASE}(s, j)$: noise from amplified spontaneous emission (ASE) generated by each amplifier along the service;
- $NSR^{NLI}(s, j)$: noise from fiber Kerr nonlinearity (NLI), influenced by the launch power spectrum per span;
- $NSR^{TRX}(j)$: transponder B2B noise;
- $FP(j)$: penalty due to WSS filtering.

The IIR method improves estimates of insertion losses, amplifier gain spectra, and residual noise offset through three main steps:

Initialization: For each OMS i traversed by service j, the uncertain insertion loss for span n is initially split equally between the input and output of each span:

$$\delta_{(i,n)} = \delta'_{(i,n)}$$

The amplifier gain spectra are initially assumed to be linearly tilted.

—

Step 1: Gain Spectrum Refinement For each snapshot s, a gradient-descent algorithm [85] refines the amplifier gain spectra $G^s_{(i,n)}(\lambda)$ to minimize the discrepancy between the monitored and estimated power spectrum at the end of the OMS i:

$$\text{Cost1} = \sqrt{\sum_{\lambda} \left[P^s_{(i,N+1)}(\lambda) - \hat{P}^s_{(i,N+1)}(\lambda) \right]^2} \tag{5.2}$$

Where:

- $P^s_{(i,N+1)}(\lambda)$ is the monitored power spectrum at the end of OMS i.
- $\hat{P}^s_{(i,N+1)}(\lambda)$ is the estimated spectrum at the end of OMS i after propagation from the first amplifier, including SRS, wavelength-dependent fiber attenuation, and the current gain profile estimate:

$$\hat{P}^s_{(i,N+1)}(\lambda) = P^s_{(i,1)}(\lambda) \cdot \prod_{n=1}^{N} \delta_{(i,n)} \cdot \rho_{(i,n)}(\alpha_{(i,n)}, g_{(i,n)}, \ldots) \cdot \delta'_{(i,n)} \cdot G^s_{(i,n)}(\lambda) \tag{5.3}$$

Here, $\rho_{(i,n)}$ models the power evolution term including SRS effect (SRS coefficient $g_{(i,n)}$) and wavelength-dependent fiber attenuation (fiber attenuation coefficient $\alpha_{(i,n)}$). We apply the SRS triangular approximation model, which was experimentally validated in [10].

—

Step 2: Insertion Loss Refinement The variation in NSR between snapshot s and a baseline snapshot k is defined as:

$$\begin{aligned} \Delta NSR(s,j) &= NSR(s,j) - NSR(k,j) \\ &= \big(NSR^{ASE}(s,j) - NSR^{ASE}(k,j)\big) \\ &\quad + \big(NSR^{NLI}(s,j) - NSR^{NLI}(k,j)\big) \end{aligned} \tag{5.4}$$

Note that $NSR^{TRX}(j)$ and $FP(j)$ are assumed to be constant with time for each service j, therefore they cancel out.

The ASE and NLI components are calculated as follows:

$$NSR^{ASE}(s,j) = \sum_i \sum_{n=1}^{N+1} \frac{hfF^s_{(i,n)}G^s_{(i,n)}R_s}{P^s_{(i,n)}} \tag{5.5}$$

$$NSR^{NLI}(s,j) = \sum_i \sum_{n=1}^{N+1} \gamma_{(i,n)} \cdot \big(P^s_{(i,n)}\big)^2 \cdot \big(\delta_{(i,n)}\big)^2 \tag{5.6}$$

Where: h: Planck's constant, f: optical frequency of the service, $F^s_{(i,n)}$ and $G^s_{(i,n)}$: the NF and gain spectra at span n in OMS i for snapshot s, R_s: baud rate, $\gamma_{(i,n)}$: nonlinear coefficient.

Insertion loss $\delta_{(i,n)}$ and $\delta'_{(i,n)}$ are refined to minimize the following cost function:

$$\text{Cost2} = \sqrt{\sum_{s}\sum_{j}\left[\Delta NSR(s,j) - \Delta\widehat{NSR(s,j)}\right]^2} \tag{5.7}$$

Since booster launch power spectrum changes over snapshots, both $NSR^{ASE}(s,j)$ and $NSR^{NLI}(s,j)$ are snapshot-dependent, which we account for. In contrast, we neglect the variation of $NSR^{TRX}(j)$ and $FP(j)$ and assume constant noise across snapshots.

—

Step 3: E2E Offset Noise Refinement For each service j at snapshot s, the residual E2E offset noise is estimated as:

$$Noise_{\text{offset}}(s,j) = NSR(s,j) - \widehat{NSR(s,j)} \tag{5.8}$$

Where: $NSR(s,j)$ is the monitored NSR derived from BER, $\widehat{NSR(s,j)}$ is the estimated NSR after refinement of insertion loss $\delta_{(i,n)}, \delta'_{(i,n)}$ and amplifier gain spectrum $G^s_{(i,n)}$ from Steps 1 and 2.

This final step captures the residual noise that may arise from inaccurate E2E modeling such as transponder B2B noise or WSS-induced penalties. The error of SNR (NSR) estimation with refined $Noise_{\text{offset}}$ is reduced to zero by construction; as will be seen later, $Noise_{\text{offset}}$ is used to reduce the prediction error.

5.4. Simulation Validation for IIR

5.4.1. Simulation Testbed

Table 5.2: OMS info.

Item	OMS1	OMS2	OMS3	OMS4	OMS5
Number of spans	2	2	5	2	1
Span details	40+80 km LEAF	80+20 km SMF	5×80 km SMF	80 km LEAF + 80 km TW	20 km SMF
Total length [km]	120	100	400	160	20
# channels	30	35	45	40	30

Channel information: 400 Gb/s (90 Gbaud, PCS16QAM) transponder, 100 GHz grid in the 6 THz C-band.

Table 5.3: Routing table.

Source	Sink	Path	Service #
C	B	3-4-5-1	5
B	A	2-3-4-5	5
A	E	1-2-3-4	5
D	C	4-5-1-2	5
C	A	3-4-5	5
C	E	3-4	5
B	E	2-3-4	5
D	B	4-5-1	5
A	D	1-2-3	5
B	D	2-3	5
E	C	5-1-2	5
C	D	3	5

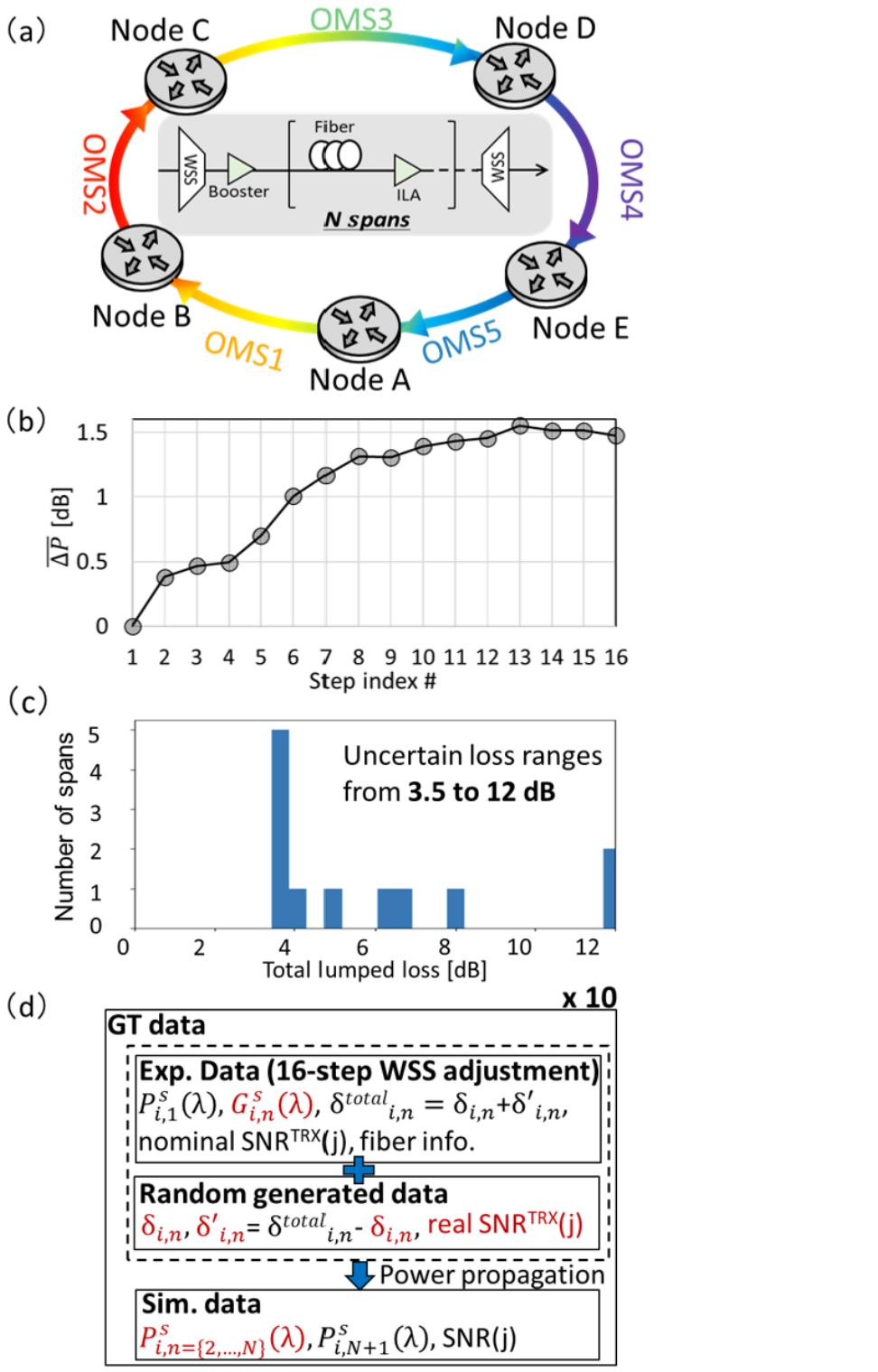


Figure 5.2: (a) 5-OMS ring-topology network; (b) Average booster power variation across snapshots; (c) Histogram of total uncertain insertion loss across all spans; (d) Data usage assumption for simulation validation.

The proposed IIR method was first validated through simulations using experimental data gathered in the experiment described in [123]. The experimental dataset includes 15 steps (16 snapshots in total, including the initial snapshot) of WSS adjustments in a C-band ring-topology network to optimize power profiles. The testbed, illustrated in Fig. 5.2(a), consists of 5 OMSs with heterogeneous fiber lengths and types; 12 routing paths are configured, with additional OMS details provided in Table 5.2 and service routing information in Table 5.3 . Each routing path carries five services traversing between 1 and 4 OMSs, for a total of 60 services using 90 Gbaud 400G PCS-16QAM modulation. At each step, WSS reconfiguration modifies the attenuation of multiple channels (up to 1 dB per channel) on a single OMS, thereby altering its booster power spectrum. Fig. 5.2(b) shows the average (taken over all channels used by a service) booster power variation across the $M = 5$ OMSs for all 16 snapshots, denoted as $\overline{\Delta P}$:

$$\overline{\Delta P}(s) = \frac{1}{M} \sum_{i=1}^{M} \left| P^{s}_{(i,1)}(:) - P^{1}_{(i,1)}(:) \right| \tag{5.9}$$

Additional implementation details for the underlying experimental dataset can be found in [123].

As shown in Fig. 5.2(d), we generate 16 network snapshots using a combination of experimental and randomly generated data.

The experimental data include:

- Booster power spectra $P^{s}_{(i,1)}$ from each WSS step;
- Amplifier gain spectra $G^{s}_{(i,n)}(\lambda)$;
- Total insertion losses $\delta^{\text{total}}_{(i,n)}$ (ranging from 3.5 to 12 dB, also shown in
- Nominal transponder B2B ceiling SNR: SNR^{TRX};
- Fiber characteristics.

The randomly generated data include:

- Insertion loss at input of the fiber: $\delta_{(i,n)} \sim U[0, 3]$ dB;
- Insertion loss at output of the fiber: $\delta'_{(i,n)} = \delta^{\text{total}}_{(i,n)} - \delta_{(i,n)}$;
- B2B transponder ceiling SNR with added uncertainty: $SNR^{TRX} + U[-1, 1]$ dB.

For each snapshot, the booster power spectrum $P^{s}_{(i,1)}(\lambda)$ is propagated along the OMS to compute the intermediate and output spectra $P^{s}_{(i,n)}(\lambda)$, $n = 2, \ldots, N + 1$. The SNR for

each service is then calculated using the Gaussian noise model [117].

All experimental, random, and simulated parameters are treated as ground truth (GT) to construct the 16 snapshots. The IIR algorithm is then applied to estimate the unknown parameters (highlighted in red in Fig. 5.1), using only the known parameters (in black in Fig. reffigjocn25.1) from the generated snapshots. We use the initial snapshot as the baseline snapshot ($k = 1$ in Eq. (4)). To enable statistical validation of the IIR method, 10 independent test cases are generated and evaluated.

5.4.2. Simulation Results

5.4.2.1. Insertion Loss Estimation

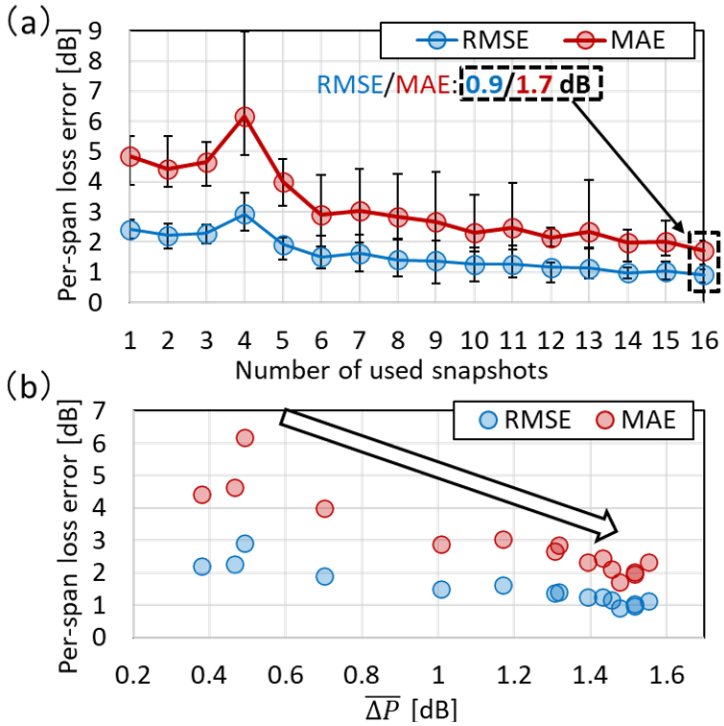


Figure 5.3: (a) Per-span insertion loss estimation accuracy; (b) Correlation between insertion loss estimation accuracy and power variation.

Fig. 5.3(a) shows the accuracy of per-span insertion loss refinement using IIR as a function of the number of utilized snapshots. Both root-mean-square error (RMSE) and maximum absolute error (MAE) are reported. Each data point represents the average of 10 randomized test cases, and the error bars indicate the range. At snapshot #1, the initial assumption $\delta_{(i,n)} = \delta'_{(i,n)}$ yields an RMSE and MAE of 2.4 dB and 4.8 dB, respectively. With only a few snapshots (e.g., 4), the MAE increases to 6.2 dB due to insufficient

variation to be learned, hence hindering proper parameter estimation and thus causing large error. As more snapshots are collected, IIR significantly improves the connector loss accuracy, reducing the error to 0.9 dB RMSE and 1.7 dB MAE when using all 16 snapshots.

Fig. 5.3(b) shows the correlation between fiber insertion loss estimation error and average booster power variation $\overline{\Delta P}$ (shown in Eq. (9)). As the power variation and the associated SRS and BER variations increase, insertion loss estimation improves. With average power variation reaching approximately 1.5 dB, the RMSE converges to 0.9 dB.

5.4.2.2. QoT Estimation and Prediction

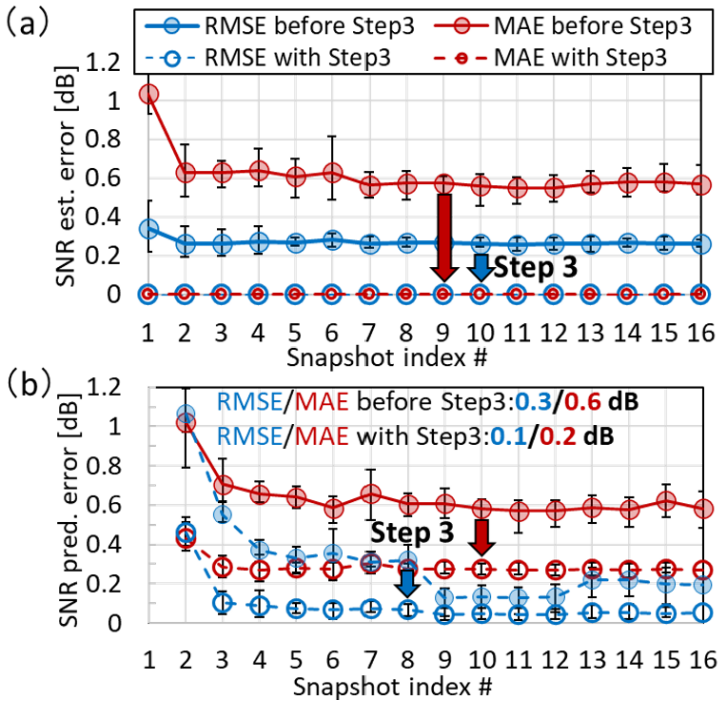


Figure 5.4: (a) SNR estimation with IIR; (b) SNR prediction with IIR.

Fig. 5.4(a) reports the estimated SNR at snapshot s, using IIR-refined parameters from snapshots #1 to s as input to the DT. At snapshot #16, the error remains at 0.3 dB RMSE and 0.6 dB MAE, mainly due to the uncertainty of the E2E offset noise. In Step 3 of IIR, this E2E offset is estimated and used to correct the SNR estimation error, which is reduced to zero by construction. As shown later, this offset correction enables highly accurate SNR prediction.

Fig. 5.4(b) presents the SNR predicted at snapshot s using IIR-refined parameters from snapshots #1 to $s-1$. Without the offset correction, the prediction error at snapshot #16

is 0.3 dB RMSE and 0.6 dB MAE. When the refined offset noise from Step 3 is included, the error decreases to 0.1 dB RMSE and 0.2 dB MAE. The remaining error is due to imperfections in parameter refinement and unmodeled changes in amplifier gain spectra.

5.4.2.3. One-shot QoT Optimization

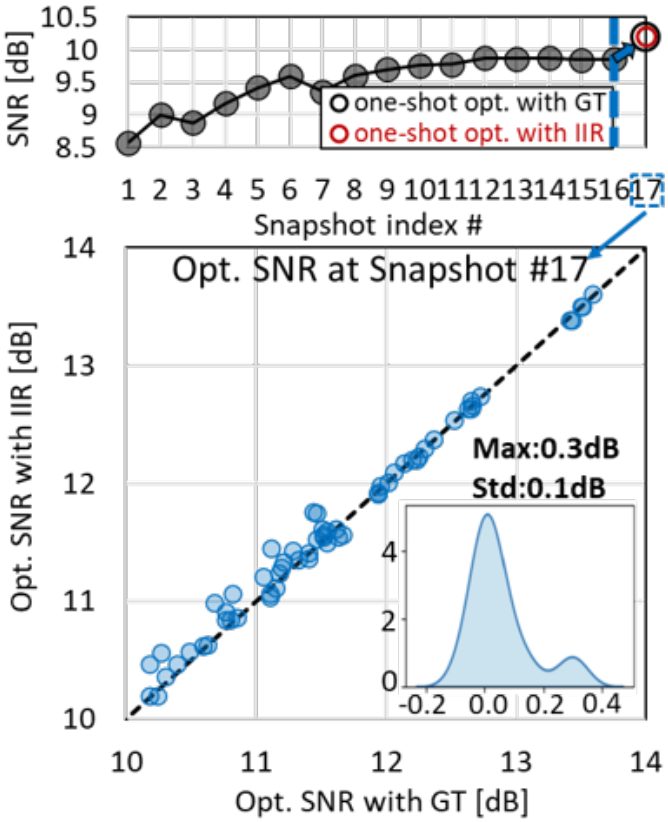


Figure 5.5: Optimized network margin (top) and one-shot optimized SNR (bottom).

Fig. 5.5 (top) shows the network margin (i.e., the worst-case SNR among all services) during the 15-step WSS-based power optimization, using GT parameters from snapshots #2 to #16 (black dots, left of the blue dashed line). At snapshot #16, a further one-shot power optimization is performed by adjusting the launch power spectrum of the booster of each OMS for snapshot #17 using DT-based targets to achieve ASE/NLI equal to 3 dB for each service at the output of each OMS, as suggested by the LOGO strategy [101]. The optimization is performed with either GT parameters (black circle at snapshot #17) or IIR (red circle)-refined parameters. In both cases, the network margin increases from 9.8 dB to 10.2 dB, indicating that IIR-refined parameters are sufficiently accurate for optimization.

Fig. 5.5 (bottom) compares DT-optimized SNRs for all 60 services at snapshot #17 using IIR-refined versus GT parameters. The inset shows the probability density function of the SNR difference. The results confirm close agreement, with a standard deviation of 0.1 dB and a maximum difference of 0.3 dB.

5.5. Experimental Validation for IIR

5.5.1. Experimental Testbed

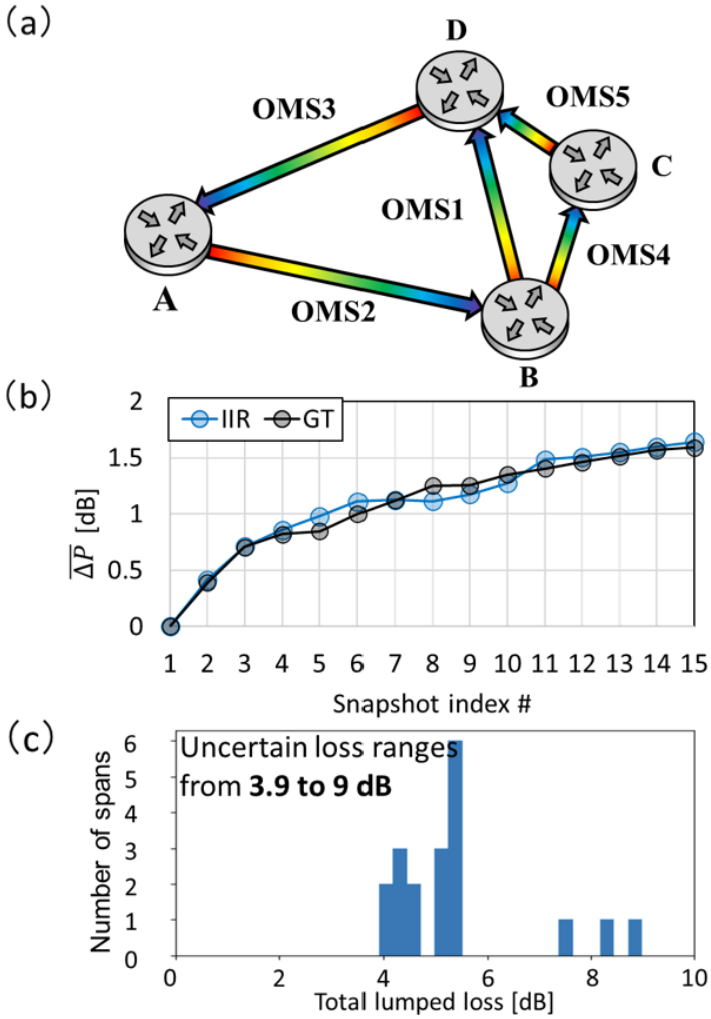


Figure 5.6: (a) 5-OMS mesh network; (b) Average booster power variation; (c) Histogram of total uncertain insertion losses.

Table 5.4: OMS info.

Item	OMS1	OMS2	OMS3	OMS4	OMS5
Number of spans	5	5	5	2	2
Span details	5×80 km SMF	5×100 km PSCF	2×100 km PSCF + 60/80/100 km SMF	80 km LEAF + 80 km TW	40+80 km SMF
Total length [km]	400	500	440	160	120
# channels	30	50	50	30	30

Channel information: 400 Gb/s (90 Gbaud, PCS16QAM) transponder, 100 GHz grid in the 6 THz C-band.

Table 5.5: Routing table.

Source	Sink	Path	Service #
B	D	1	10
B	A	1-3	10
A	D	2-1	10
A	C	2-4	5
D	B	3-2	5
D	C	3-2-4	15
B	C	4	10
C	D	5	10
C	A	5-3	5
C	B	5-3-2	15

The proposed IIR method was then experimentally validated in a 5-OMS mesh-topology network, shown in Fig. 5.6(a). The details of the testbed configuration are provided in Table 5.4. It consists of 5 OMSs with heterogeneous fiber types (i.e., SMF, PSCF, LEAF, and TW) and span lengths ranging from 40 km to 100 km. Table 5.5 summarizes the 10 routing paths configured in the network. Each path carries between 5 and 15 services, traversing 1 to 3 OMSs, for a total of 95 services in this partially loaded C-band network. Channel loading is emulated using an ASE source, and the BER (and corresponding SNR) is measured using a real-time transponder operating at 90 Gbaud with 400G PCS-16QAM modulation. Transponder B2B SNR^{TRX} is characterized in the lab, and for QoT prediction, an uncertainty uniformly distributed over $[-1, 1]$ dB is added to reflect realistic uncertainty of SNR^{TRX}.

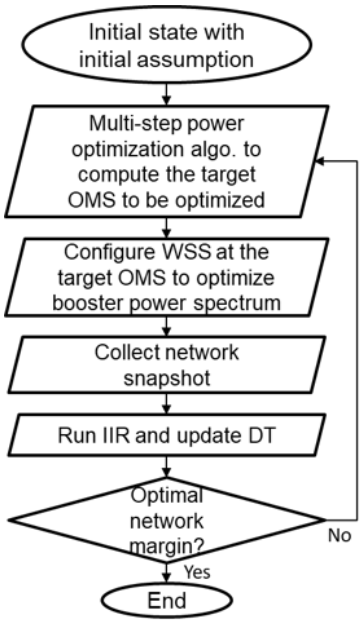


Figure 5.7: Flow chart of the IIR-enabled closed-loop multi-step power optimization.

This experiment focuses on an automated closed-loop QoT optimization framework based on a DT, whose architecture is shown in Fig. 5.7. The objective is to maximize the network margin (the worst-case SNR among all services), using a multi-step power optimization algorithm adapted from [125]. At each optimization step, the algorithm selects a target OMS for WSS reconfiguration, based on the predicted improvement to the network margin. The WSS attenuation profile of selected channels is modified by up to 1 dB per channel, altering the booster power spectrum of the selected OMS.

The average booster power variation across all five OMSs $\overline{\Delta P}$ (shown in Eq. 5.9) over the 14 optimization steps with 1) GT parameters and 2) IIR-refined parameters are shown in Fig. 5.6(b). Fig. 5.6(c) shows the total insertion losses $\delta^{\text{total}}_{(i,n)}$, ranging from 3.9 to 9 dB.

The OMS selection and attenuation control rely entirely on the accuracy of QoT predictions enabled by the DT, which in turn depend on the accuracy of its input parameters. To ensure accurate input parameter refinement, a new network snapshot is collected after each WSS adjustment, and the IIR method is applied using all accumulated snapshots, enabling incremental refinement of fiber insertion losses, amplifier gain spectra, and E2E offset noise. These refined parameters are used to update the DT model, allowing progressively improved QoT prediction and more effective decision-making at each step of the optimization process to improve the network margin.

5.5.2. Experimental Results

5.5.2.1. Insertion Loss Estimation

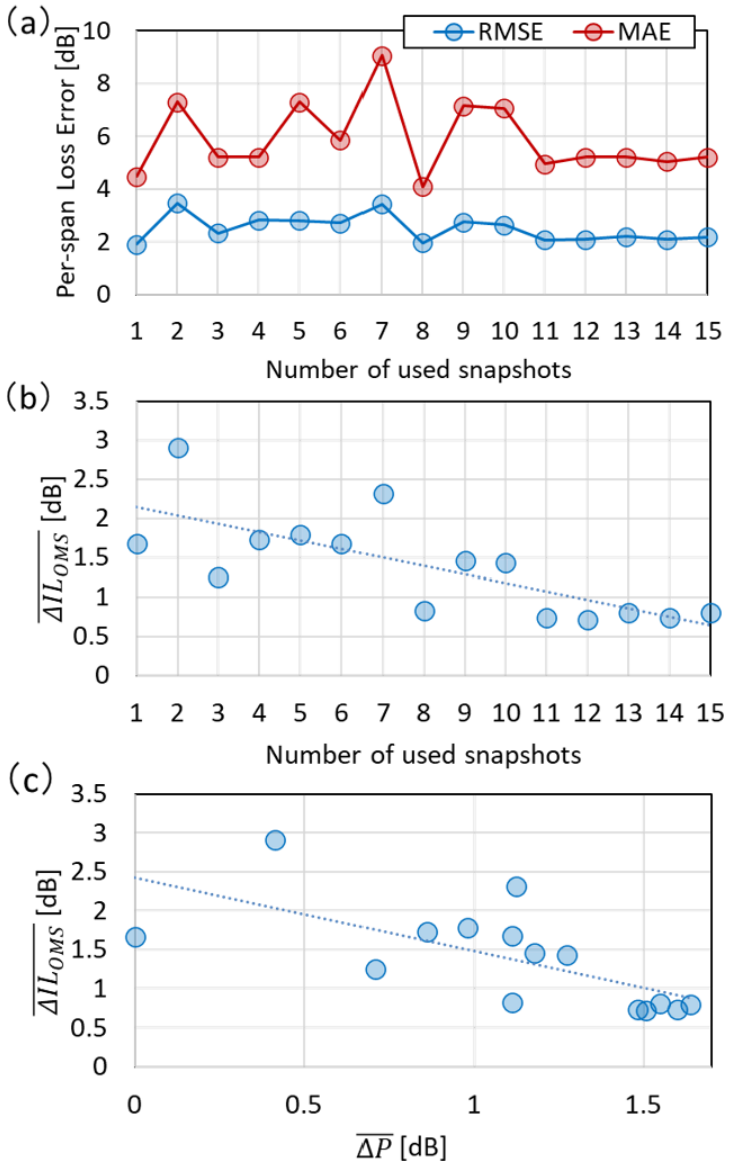


Figure 5.8: (a) Per-span insertion loss estimation accuracy; (b) Average absolute error of OMS-level insertion loss estimation; (c) Correlation between OMS-level insertion loss estimation accuracy and power variation.

Fig. 5.8(a) shows the accuracy of per-span insertion loss refinement using IIR across different numbers of snapshots. Both RMSE and MAE do not show improvement with additional snapshots: the initial 50%/50% insertion loss split assumption yields an RMSE/MAE of 1.9/4.5 dB, while IIR using 15 snapshots results in slightly worse values of 2.2/5.2 dB. This degradation is primarily due to modeling inaccuracies such as SRS and Kerr effects, which limit the accuracy of per-span estimation. In contrast, simulation results

in Section 3 show improved accuracy under idealized conditions without such modeling uncertainties.

Fig. 5.8(b) shows the average absolute error of per-OMS insertion loss estimation across $M = 5$ OMSs, as defined by:

$$\overline{\Delta IL}_{\text{OMS}} = \frac{1}{M} \sum_{i=1}^{M} \left| \overline{IL_i^{\text{IIR}}} \right|, \tag{5.10}$$

where the average insertion loss per OMS is given by:

$$\overline{IL_i^{\text{IIR}}} = \frac{1}{N} \sum_{n=1}^{N} \left(IL_{(i,n)}^{\text{IIR}} - IL_{(i,n)}^{\text{GT}} \right). \tag{5.11}$$

The results show that while per-span insertion loss estimation remains inaccurate, IIR significantly improves insertion loss estimation at the OMS level. With 15 snapshots, the average OMS-level insertion loss error is reduced from 1.7 dB to 0.7 dB. This improvement is due to IIR's ability to aggregate the effects over multiple spans, thereby mitigating modeling inaccuracies. Since the impact of insertion loss on QoT, primarily through Kerr nonlinearity, depends on the characteristics of each span, it is possible to achieve accurate SNR estimates even if individual span losses are inaccurate, as long as their cumulative nonlinear effect is preserved. In contrast, the initial 50/50% split often results in incorrect aggregate impact. In summary, IIR refines insertion losses so that QoT estimation or prediction remains globally accurate at the OMS and service levels, despite local per-span errors.

Fig. 5.8(c) illustrates the correlation between the average OMS-level insertion loss estimation error and the average booster power variation $\overline{\Delta P}$ across 5 OMSs between snapshot s and snapshot #1. The results indicate that greater power variation, and consequently greater BER (SNR) variation, leads to more accurate insertion loss estimation. When the average power variation reaches 1.6 dB, the OMS-level insertion loss error is reduced from 1.7 dB to 0.7 dB.

5.5.2.2. QoT Estimation and Prediction

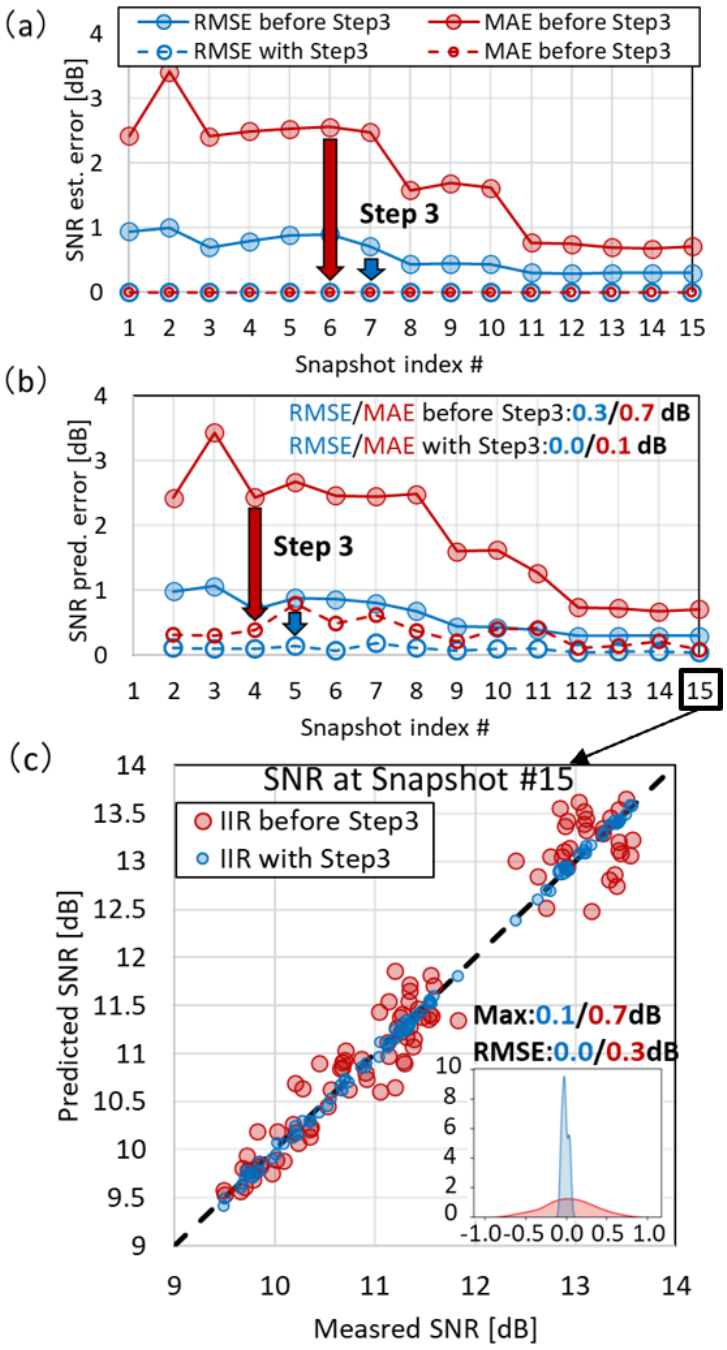


Figure 5.9: (a) SNR estimation with IIR; (b) SNR prediction with IIR; (c) SNR prediction accuracy with/without IIR step 3 at Snapshot #15.

Fig. 5.9(a) reports the estimated SNR at snapshot s, using IIR-refined parameters from snapshots #1 to s as input to the DT model. At snapshot #15, the error remains 0.3 dB RMSE and 0.7 dB MAE, a substantial improvement compared to the initial state using

the default parameter assumptions, where the RMSE and MAE are 0.9 dB and 2.4 dB, respectively. This demonstrates that, although per-span insertion loss estimation remains inaccurate, IIR significantly improves OMS-level insertion loss estimation, thereby enhancing the accuracy of nonlinear impairment modeling. The remaining error is primarily attributed to the uncertainty in the E2E offset noise. In Step 3 of the IIR process, this E2E offset is estimated and used to correct the NSR error, effectively reducing the error to zero (by construction).

Fig. 5.9(b) presents the SNR predicted at snapshot s using IIR-refined parameters from snapshots #1 to $s-1$. Without offset correction (Step 3; red disks), the prediction error is improved from 1.0 dB RMSE and 2.4 dB MAE at initial state to 0.3 dB RMSE and 0.7 dB MAE for snapshot $s = 15$. When the refined offset noise from Step 3 is incorporated (blue disks), the error is further reduced to < 0.1 dB RMSE and 0.1 dB MAE. These results demonstrate that IIR enables highly accurate QoT prediction by progressively refining physical-layer parameters and compensating for E2E offset noise contributions.

Fig. 5.9(c) presents the predicted SNR using IIR-refined parameters, with and without the application of Step 3 (E2E offset noise refinement). The results are consistent with those shown in at snapshot #15. Before applying Step 3, the prediction exhibits an RMSE/MAE of 0.3/0.7 dB. After Step 3 is applied, the prediction accuracy significantly improves, reducing the error to below 0.1 dB for both RMSE and MAE. The inset displays the probability density function of the SNR prediction error, confirming the improved prediction accuracy achieved through E2E offset noise refinement.

5.5.2.3. IIR-enabled Multi-step QoT Optimization

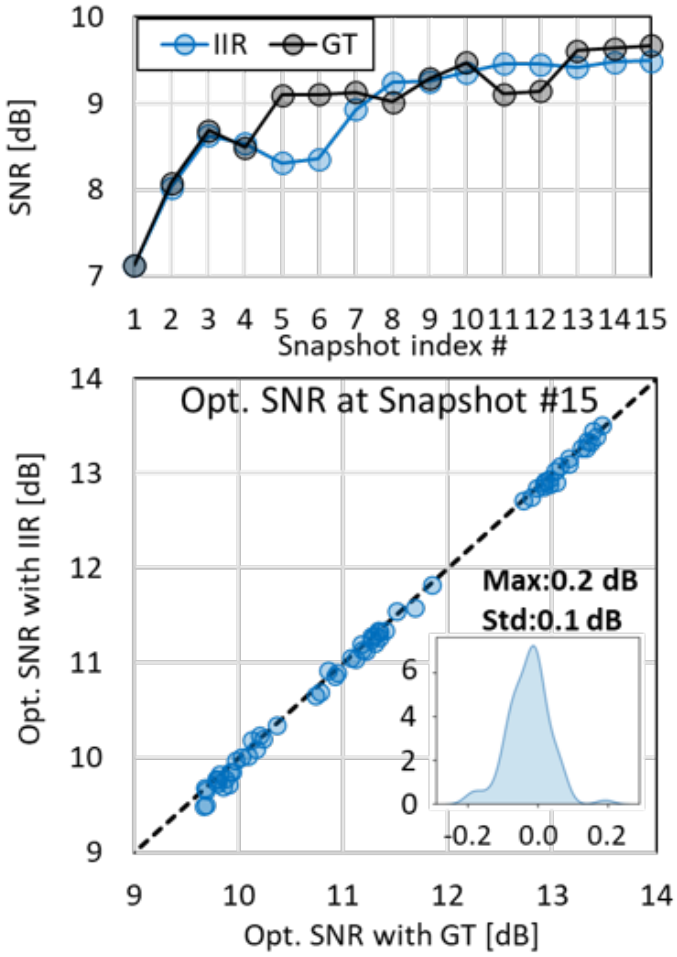


Figure 5.10: Optimized network margin enabled by IIR-refined/GT parameters (top), and optimized SNR at snapshot #15 (bottom).

Fig. 5.10 (top) shows the network margin (worst-case SNR) among all 95 services at different snapshots during the multi-step optimization process, using either 1) GT or 2) IIR-refined parameters. With GT parameters, the margin increases from 7.1 dB to 9.7 dB, while IIR-refined parameters yield an improvement from 7.1 dB to 9.5 dB. This small 0.2 dB difference confirms that the IIR-refined parameters are sufficiently accurate to enable effective QoT optimization, achieving near-identical performance to the GT case.

Fig. 5.10 (bottom) compares the optimized SNRs for all 95 services at snapshot #15 using IIR-refined versus GT parameters. The inset shows the probability density function of the SNR differences. The results demonstrate strong agreement, with a standard deviation

of 0.1 dB and a maximum deviation of 0.2 dB.

5.6. Conclusions

We proposed a novel technique, IIR, that leverages multiple network snapshots to iteratively refine amplifier gain spectrum, fiber insertion loss, and E2E service offset noise. This approach enables accurate QoT prediction and efficient self-driven QoT optimization in optical networks. The IIR method was validated through both simulations (based on experimental data on a C-band ring-topology network with 5 OMSs), and experiments on a C-band mesh-topology network with 5 OMSs. Results demonstrate that IIR significantly improves insertion loss estimation, QoT prediction accuracy, and optimization performance, achieving near-identical performance to the case knowing GT parameters.

These findings highlight the critical importance of accurate physical-layer parameter estimation for the performance and reliability of modern optical networks. By effectively exploiting monitored data across multiple network snapshots, the proposed IIR method offers a practical and scalable solution to address uncertainties arising from nonlinear effects and hardware variability. It lays a foundation for robust and autonomous optical network control, well-aligned with the stringent performance and flexibility demands of emerging 5G and 6G infrastructures.

6 | Integrating PPE and Inputs Refinement for Enhanced QoT Estimation and Optimization in an Optical Mesh Network

6.1. Abstract

We propose and experimentally validate a novel method for improved power and insertion loss estimation, enabling anomalous loss detection, QoT estimation and optimization in a mesh network, achieving 0.7 dB average SNR increase and 1 dB network margin enhancement.

6.2. Introduction

Accurate monitoring of physical parameters is essential for network anomaly detection, Quality of Transmission (QoT) estimation, and AI-based automation [15, 56, 98, 102, 123, 154]. Two recent techniques, fiber longitudinal Power Profile Estimation (PPE) and Inputs Refinement (IR), have emerged to enhance monitoring accuracy in optical networks.

PPE enables accurate per-channel longitudinal power profile $P(z)$ estimation from received signal samples at a coherent receiver [22, 112, 114]. Recent theoretical studies indicate that Least-Squares (LS) based PPE can approach absolute power-profile estimation when ignoring noise (e.g., laser phase noise and Amplified Spontaneous Emission (ASE) noise) and distortion (e.g., from transceiver and in-line optical filtering), and essentially requires fine spatial resolution enabled by large baud rates [113]. However, these conditions are unrealistic in current operational networks; hence, experimental demonstrations of PPE have focused on relative profile estimation, which enables detection of intermediate power losses along spans [82, 127]. Accurate absolute PPE remains an un-

solved problem under typical constraints, yet it is crucial for connector-loss estimation, fiber nonlinearity estimation, and accurate QoT estimation.

IR aims to improve ("refine") the estimation of physical parameters that are difficult to monitor in real networks, namely connector insertion losses and amplifier gain profiles. Specifically, in our previous work [87], IR was demonstrated to accurately estimate real-time overall insertion losses and amplifier gain profiles at the Optical Multiplex Section (OMS) level, thereby enabling accurate Generalized Signal-to-Noise Ratio (GSNR) estimation for each OMS. However, span-level estimation accuracy was difficult to achieve. This limitation was overcome in [154], but required actively probing the network by temporarily changing amplifier operation points, at the expense of a (small) SNR penalty that operators may be unwilling to accept. Moreover, IR in [87, 154] only yields $P(z = 0)$, i.e., the fiber launch power (LP) of each span, but not $P(z)$ for all z.

In this paper, we integrate IR (without active probing) with LS-based PPE for real-time estimation of insertion losses, amplifier gain profiles, and longitudinal power profiles. This integration enables: anomalous connector-loss detection and localization, accurate QoT estimation, and ultimately network capacity and margin enhancement. All of these features are experimentally demonstrated in a testbed emulating a realistic mesh optical network.

6.3. Method Description

Table 6.1: Input and output parameters of IR and PPE.

	IR [87]	**PPE [112]**
Input	Output power profiles of booster and pre-amplifier; Total input/output power at each amplifier; Fiber types and lengths	Received samples; Total dispersion; Fiber types and lengths
Output	Insertion losses and amplifier gain profiles (per span, inaccurate)	Longitudinal power profile (*relative*)

The input parameters (available in real networks) and outputs of PPE and IR are summarized in Tab. 6.1.

PPE: LS-based PPE method [112].

IR: Our previous work on inputs refinement [87], without any active probing.

IR+PPE (proposed): The proposed method consists of three steps:

1. **Initialization of inputs:**

   (a) For each service i, run PPE [112] and extract the (inaccurate absolute) estimated launch power (LP) over each span s crossed by service i: $LP_{i,s}^{\mathrm{PPE}}$. The (accurate relative) normalized LP is then calculated as:

   $$\widehat{LP}_{i,s}^{\mathrm{PPE}} = LP_{i,s}^{\mathrm{PPE}} - \mathrm{mean}_s\langle LP_{i,s}^{\mathrm{PPE}}\rangle.$$

   (b) Assume a 50/50% distribution of the total insertion loss between the input and output of each span.

2. **Gain profile estimation:** Estimate the amplifier gain profile in the network as described in [87].

3. **Insertion loss estimation:** Estimate the insertion losses for each span using the gradient descent method L-BFGS-B [165] to minimize the following error function:

   $$\mathrm{error} = \sum_i \sum_s \left| \widehat{LP}_{i,s}^{\mathrm{PPE+IR}} - \widehat{LP}_{i,s}^{\mathrm{PPE}} \right|^2,$$

   where the normalized estimated LP is defined as

   $$\widehat{LP}_{i,s}^{\mathrm{PPE+IR}} = LP_{i,s}^{\mathrm{PPE+IR}} - \mathrm{mean}_s\langle LP_{i,s}^{\mathrm{PPE+IR}}\rangle.$$

   Here, $LP_{i,s}^{\mathrm{PPE+IR}}$ is obtained by simulating power propagation along service i using the estimated insertion losses and gain profiles.

Finally, the proposed IR+PPE method provides: (i) estimated per-span insertion losses, (ii) gain profiles of each amplifier, and (iii) per-channel longitudinal power along spans.

6.4. Experimental Testbed

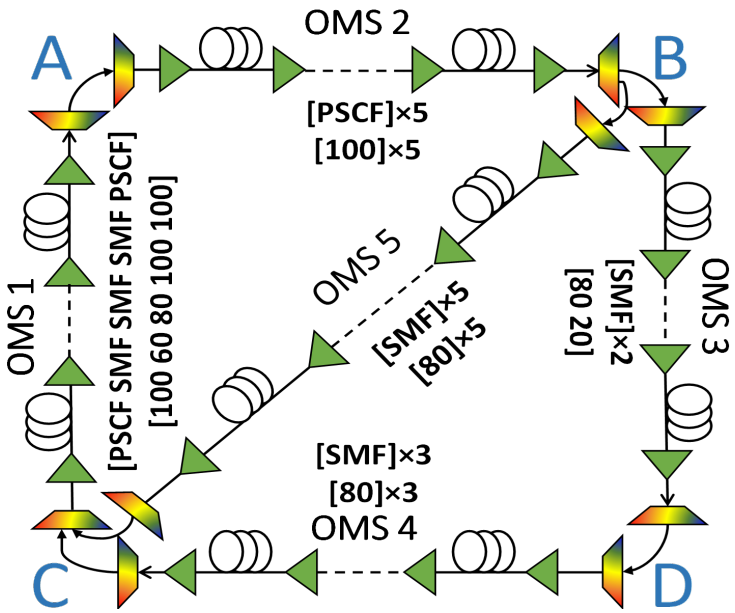


Figure 6.1: 5-OMS mesh network testbed.

We experimentally implement in our lab a mesh network based on commercial equipment, which comprises 5 OMSs with heterogeneous span numbers, fiber lengths, and fiber types (see Fig. 6.1). Other fiber parameters come from datasheets. To emulate a realistic partially-loaded network, 81 services are emulated by an ASE source with 100 GHz channel spacing in the 6 THz C-band. The services' sources and destinations are randomly picked and first-fit wavelength allocation is used. The resulting channel occupancy of OMS 1/2/3/4/5 is 77/65/40/45/45%. Services' received samples and SNR are measured by replacing each one of the 81 emulated services with an offline transponder (PDM-PCS-16QAM, 90 Gbaud, 400 Gb/s). Variable Optical Attenuators (VOAs) are utilized to set insertion losses at input/output of each span with a range of up to 5 dB to emulate (anomalous) insertion losses at the connectors. The booster LP profile is set to be flat, with the total power calculated by LOGO [101]; amplifier nominal gain is set to compensate for span loss. In Step 1, we use an average of 10 PPE runs, each time collecting 600k samples (1 sample per symbol) per polarization.

6.5. Results

6.5.1. Power Profile Estimation Enhancement

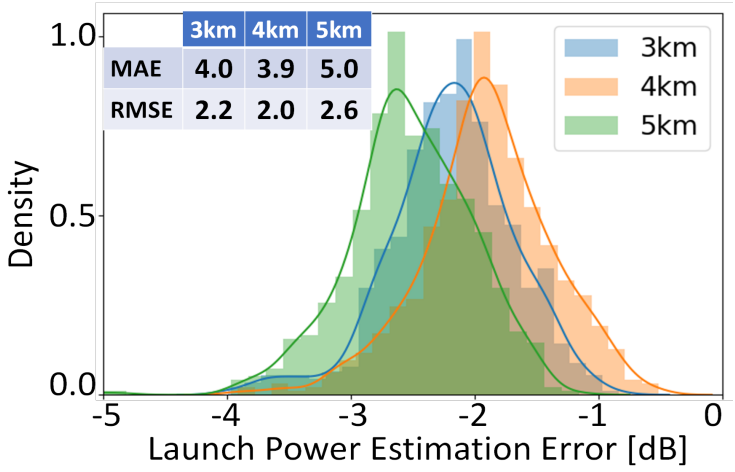


Figure 6.2: PPE performance with different spatial resolutions.

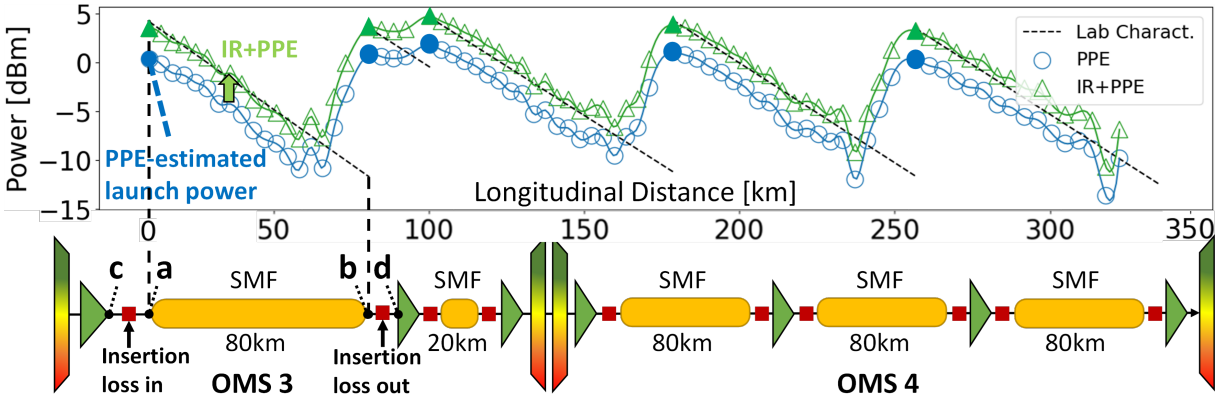


Figure 6.3: Power profile estimation by PPE and by IR+PPE; plain markers are the estimated LPs.

Fig. 6.2 illustrates the PPE-estimated LP error per span across all 81 services with $\{3, 4, 5\}$ km different spatial resolutions. The inset table shows the Maximum Absolute Error (MAE) and Root-Mean Square Error (RMSE) of LP estimation. We find that LPs are underestimated with all resolutions; 4 km resolution provides the lowest error, which nevertheless remains large with 2 dB RMSE. In the following results, PPE and IR+PPE are obtained with 4 km resolution.

Fig. 6.3 provides an example of improvement on the accuracy of longitudinal power profile estimation for a single service achieved by IR+PPE. The sample service traverses OMS3 (2 spans) and OMS4 (3 spans). The black dashed line represents the "true" longitudinal power profile characterized in the lab with a linear interpolation based on powers at the

beginning ("a" in Fig. 3) and at the end ("b") of each span, which are obtained by adding measured powers (by optical spectrum analyzer) at amplifier output ("c")/input ("d") to the VOA-emulated insertion loss in/out, respectively. The blue circles/green triangles represent the power profile estimated by PPE/IR+PPE, respectively (plain markers are the LPs). We find that PPE has large underestimation error, while IR+PPE significantly improves the accuracy of the estimated profile, closely aligning it with the measured profile.

6.5.2. Connector Insertion Loss Estimation and Anomaly Detection

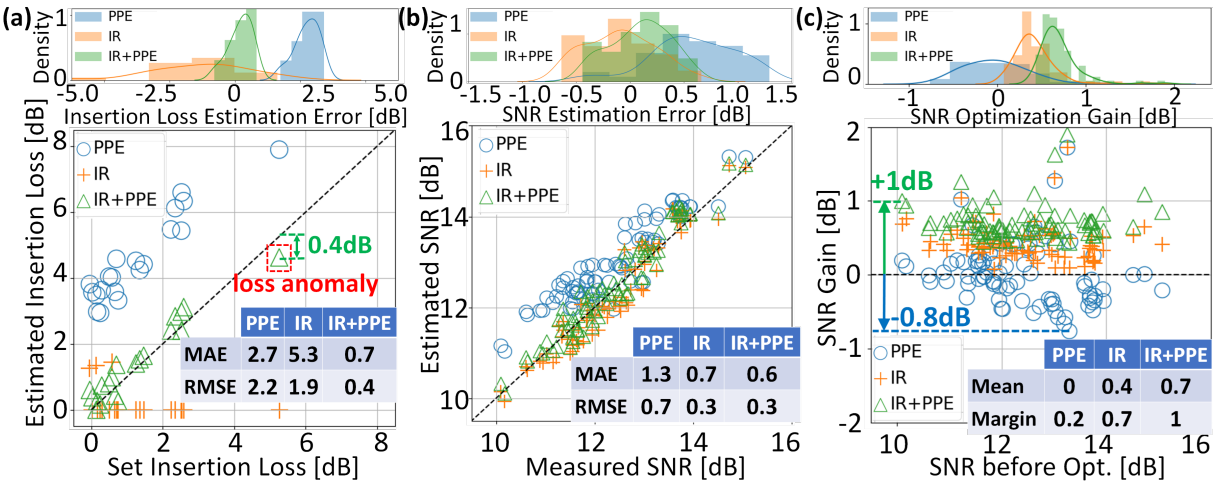


Figure 6.4: (a) Insertion losses estimation; (b) QoT estimation; (c) QoT optimization.

Fig. 6.4(a) shows estimated insertion loss vs. actual insertion loss at the input of each span. The black dashed line represents an ideal scenario where the estimated insertion loss equals the measured. Different markers indicate the insertion losses estimated by different methods: blue circles/orange plus signs/green triangles for PPE/IR/IR+PPE. We observe that, for PPE, the insertion losses are overestimated, which are calculated by subtracting the total output power at the amplifier from the sum of the underestimated LP across all channels traversing that span. The inset table indicates MAE and RMSE, and the probability density function plot is displayed above. We demonstrate that IR+PPE significantly improves insertion loss estimation with MAE/RMSE of 0.7/0.4 dB, compared to using PPE/IR alone, where the error can be up to 2.7/5.3 dB. Additionally, we demonstrate that the 5 dB anomalous loss can be well estimated with only 0.4 dB error, demonstrating the capability of IR+PPE to detect and localize anomalous losses.

6.5.3. QoT Estimation Optimization

For QoT estimation, Fig. 6.4(b) shows the estimated vs. the measured SNRs of all 81 services. Our Digital Twin (DT), similar to GNPy [40], is based on an analytical representation of the physical network, relying on accurate parameters' monitoring. We observe that IR and IR+PPE have similar QoT estimation accuracy, while PPE overestimates SNRs due to underestimation of fiber nonlinear noise (by underestimated LP). IR+PPE achieves the best performance for QoT estimation with only 0.6/0.3 dB MAE/RMSE.

For QoT optimization, we optimize each OMS booster power profile to attain a power ratio between ASE and Kerr noises of 3 dB at the end of each OMS [70, 150]. Optimal power profile is computed by the DT fed with parameters from PPE/IR/IR+PPE, respectively. The optimal power profile at each OMS is then set by adjusting the attenuation of a wavelength selective switch for each channel at the booster side. Fig. 6.4(c) shows the SNR gain with optimization. The inset table indicates the average SNR gain of all services, and the SNR margin gain on the worst service, which is the most vulnerable to disruptions. We observe that with PPE, after optimization, certain services' SNR can degrade by up to 0.8 dB, as the power is computed and set too high due to overestimation of insertion losses, thereby pushing the service into the nonlinear regime. In contrast, with accurate parameters from IR+PPE, the power is set optimally, significantly enhancing both the network's average SNR and the worst service's SNR by 0.7 and 1 dB, respectively, which bolsters the network's capacity and robustness.

6.6. Conclusions

We have proposed a method that integrates two emerging monitoring techniques, IR and PPE. We demonstrate that our combined method IR+PPE significantly enhances the performance of longitudinal power profile estimation and insertion loss estimation, which in turn enables anomalous loss detection and localization. Our proposed method improves QoT estimation accuracy (achieving a very small 0.3 dB RMSE), the average/worst services' SNRs are also improved by 0.7/1 dB, leading to a corresponding increase of network capacity and robustness.

7 | Capacity Scaling Limits of DCI Networks: A Comparative Study of ZR, ZR+, and High-Performance Transponders

7.1. Abstract

We evaluate capacity scaling achieved by ZR, ZR$^+$, and high-performance transponders for short-reach DCI networks under varying span loss, bandwidth, and WDM configurations. High-performance transponders achieve 50% more capacity over ZR/ZR$^+$ when span loss $\leq$ 31 dB. In multiplexer-based systems, optimizing loading improves capacity by 24.8 Tbps.

7.2. Introduction

The rapid traffic growth in Data Center Interconnect (DCI) networks is being driven by emerging AI applications (e.g., distributed training of large language models (LLMs) [60, 124, 159]). This study analyses the system capacity enabled by three transponder types: 800G ZR (ZR), 800G ZR$^+$ (ZR$^+$), and high-performance (HP) transponders, under progressive deployment in DCI networks.

Our analysis considers two key factors:

1. Wavelength-Division-Multiplexing (WDM) options: Multiplexer (Mux) without Amplified Spontaneous Emission (ASE) loading vs. Wavelength Selective Switch (WSS) with ASE loading.

2. Bandwidth evolution: from an initial 4.8 THz C-band to 6 THz C-band, followed by

upgrades to 4.8 THz C + 4.8 THz L-band, and ultimately a full 6 THz C + 6 THz L-band.

We evaluate the achievable capacity by simulations for each transponder type across a span loss range of 24–36 dB, using experimentally characterized data from commercial equipment in a single-span short-reach DCI scenario.

7.3. Assumptions

To model the three transponder types: {ZR, ZR+, HP}, we use the parameters shown in Tab. 1.

ZR: ZR uses 16QAM, achieving 800 Gbps with Spectral Efficiency (SE) of 5.33 bit/s/Hz. The back-to-back Signal-to-Noise Ratio (SNR), SNR_{B2B} is derived from specification in [94], including: a required pre-Forward-Error-Correction (FEC) SNR SNR_{FEC} of 12.7 dB (16QAM, OFEC), a required $OSNR_{0.1\,\mathrm{nm}}$ ($ROSNR$) of 27 dB, and a baud rate R_s of 118 Gbaud.

The Required Generalized SNR (RGSNR), accounting for ASE and fiber nonlinear noise, is given by:

$$RGSNR = \frac{ROSNR}{R_s/12.5} \quad \text{(linear)} \tag{7.1}$$

hence obtaining $RGSNR = 17.3$ dB for ZR.

As end-to-end SNR can be expressed as:

$$\frac{1}{SNR} = \frac{1}{SNR_{\mathrm{B2B}}} + \frac{1}{GSNR} \quad \text{(linear)} \tag{7.2}$$

then, by substituting $SNR = SNR_{\mathrm{FEC}}$ and $GSNR = RGSNR$, we compute $SNR_{\mathrm{B2B}} =$ 14.6 dB for ZR.

ZR+/HP: ZR+ uses PCS-16QAM/8QAM/QPSK, enabling 800/600/400 Gbps at 5.33/4/2.67 bit/s/Hz, while HP supports PCS-64QAM, enabling 1200/900 Gbps at 8/6 bit/s/Hz. As no standardized SNR_{B2B} exists, we assume ZR+ shares the same value as ZR (14.6 dB), while HP gains 3 dB (i.e., 17.6 dB) from advanced DSP and components (e.g., driver, modulator, transimpedance amplifier). SNR_{FEC} for ZR+/HP is derived from pre-FEC Bit Error Rate (BER) and modulation format.

We compare two WDM configuration options:

1. **Mux without ASE loading:** Common in point-to-point short-reach links with fixed grid, moderate insertion loss (6.5 dB [93, 94]) and cost, but lacking per-channel attenuation control and incompatible with ASE loading.

2. **WSS with ASE loading:** Enables flexible grid and per-channel attenuation setting. We assume a 3 dB average per-channel attenuation, resulting in 3 dB higher loss than Mux (i.e., 9.5 dB total). ASE loading is used to: a) stabilize load-dependent effects (e.g., amplifier gain/Noise Figure (NF), Stimulated Raman Scattering (SRS)), and b) set and adjust booster power spectrum.

7.4. Experimental Testbed

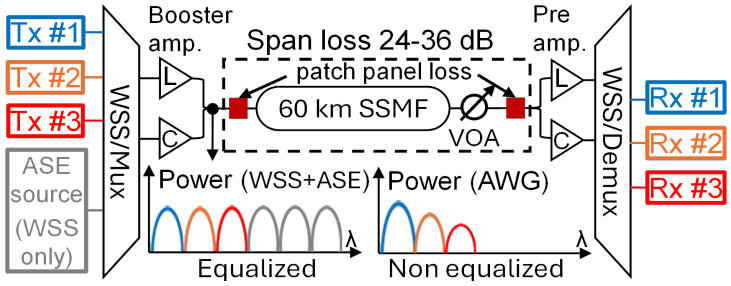


Figure 7.1: 1-span short-reach DCI network.

The experimental testbed in Fig. 7.1 emulates a 1-span DCI network and is used to collect characterized (load-dependent) booster and preamplifier gain/NF spectra to be fed into the SNR model (next section). Measurements are performed over a 60 km span of standard single-mode fiber (SSMF), with a variable optical attenuator (VOA) adjusting the span loss to 24 dB. Booster amplifier gain/tilt are configured to maximize capacity [115] under an End-of-Life (EoL) assumption (i.e., full-load spectrum); the preamplifier compensates for span loss. Transponder channel loading is emulated using an ASE source with 150 GHz spacing.

Four representative bandwidth scenarios are measured: 1) 4.8 THz C-band, 2) 6 THz C-band, 3) 4.8+4.8 THz C+L-band, and 4) 6+6 THz C+L-band,

under two WDM configuration options:

1. **Mux without ASE loading:** Gain and NF spectra of both booster/preamplifier are recorded after each channel addition, as channels are incrementally added under three orders: (i) short-to-long, (ii) long-to-short, and (iii) central-to-edges wavelength. The Mux is emulated by a WSS with flat power spectrum at the booster

amplifier input.

2. **WSS with ASE loading:** The ASE source pre-fills the spectrum at the beginning of life to stabilize the network. WSS attenuation is set to equalize the SNR across all services [48], and the fully loaded gain/NF spectra are recorded.

7.5. Modelling

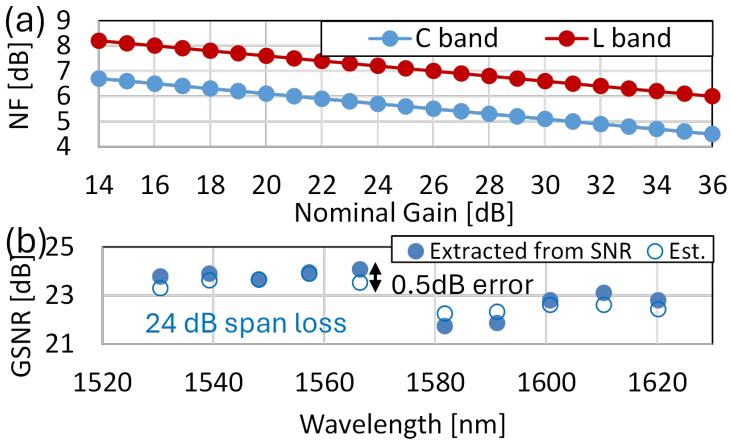


Figure 7.2: (a) NF look up table; (b) GSNR modelling validation.

Based on experimentally characterized amplifier gain/NF spectra, we evaluate the total capacity under varying span loss, total bandwidth, and channel loading order (Mux only). The modeling includes:

Span loss: Includes 2 dB patch panel loss per end (4 dB total, Fig. 7.1) and fiber loss. A lab-characterized attenuation profile is used [115], adjusted to 0.25 dB/km at 1550 nm to account for splice loss [32, 44]. Span loss varies from 24–36 dB by adjusting fiber length between 80–128 km.

Amplifier configuration: Booster amplifier gain is set assuming EoL condition as:

$$G = P_{\text{tot}}^{\text{opt}} + IL - \sum_{\lambda} P_{\text{TX}}(\lambda) \quad \text{(dB)} \tag{7.3}$$

where $P_{\text{tot}}^{\text{opt}}$ is the optimal booster output power [115], $P_{\text{TX}}(\lambda)$ is the transmit power of channel λ (Tab. 1), and Insertion Loss IL is the Mux/WSS loss. The preamplifier gain is set equal to the span loss.

Gain/NF spectra: Load-dependent gain spectra (measured at 24 dB span loss) are

shifted to align the calculated gain from Eq. (7.3). Load-dependent NF spectra are shifted (according to the calculated gain) using the lookup table in Fig. 7.2(a)

Booster power spectrum: 1) *WSS with ASE loading*: set to equalize SNR [48]. 2) *Mux without ASE loading*: determined by $P_{\mathrm{TX}}(\lambda)$, IL, and the (load-dependent) booster gain spectrum.

GSNR and SNR estimation: ASE noise is derived from measured gain/NF spectra, and fiber nonlinear noise is estimated using a closed-form EGN model [117]. GSNR is then estimated and validated against experimentally obtained values (extracted from real-time transponder SNR and known back-to-back performance) for 10 services over the 6+6 THz C+L-band at 24 dB span loss in the *WSS with ASE loading* scenario. A $\leq$0.5 dB estimation error (Fig. 7.2 (b)) is observed, confirming the modelling platform's accuracy.

End-to-end SNR: For {ZR, ZR$^+$, HP}, end-to-end SNR is calculated using Eq. (2) with accurately estimated GSNR and corresponding SNR_{B2B}. The SNR margin of each transponder is defined as:

$$\text{SNR margin} = SNR - SNR_{\mathrm{FEC}} \quad \text{(dB)} \tag{7.4}$$

Network margin: SNR margin of the worst channel.

Total capacity: Sum of bit rates of all channels.

7.6. Results

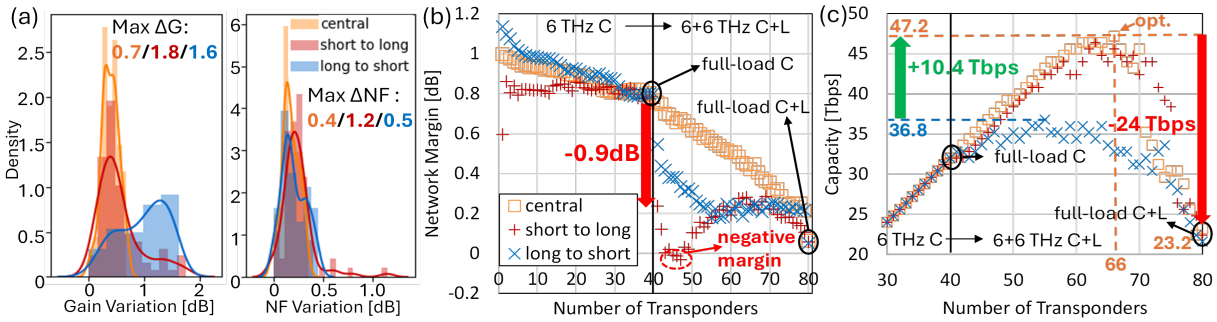


Figure 7.3: (a) PDF of booster amplifier gain/NF variation; (b) Network margin variation (ZR); (c) Total capacity variation (ZR).

7.6.1. Impact of Channel Loading Order with Mux

In non-ASE-loaded mux-based systems, margin and capacity depend on the channel ordering.

Fig. 7.3(a) shows the measured probability density functions (PDF) of the absolute maximum per-channel gain and NF variations across 80 channels in a 12 THz C+L system under three loading orders: central-to-edge, short-to-long, and long-to-short wavelengths. Loading order significantly affects amplifier behavior, with maximum gain variations of 0.7/1.8/1.6 dB and NF variations of 0.4/1.2/0.5 dB. Since the amplifier gain tilt is set for EoL, central-to-edge results in the lowest gain variation as the tilt evolves more smoothly under symmetric loading. NF is higher and more variable at short wavelengths, making short-to-long loading the worst for NF variation.

Fig. 7.3(b) shows the evolution of network margin vs. the number of plugged ZR at 31 dB span loss in 12 THz. In C-band, long-to-short/short-to-long wavelength loading offers the highest/lowest network margin during intermediate stages due to lower/higher NF at long/short wavelengths. After fully loading the C-band, the L-band is incrementally added. The optimal loading is central-to-edge, which mitigates SRS effects and amplifier gain/NF variation, yielding a smoother network margin evolution. In contrast, short-to-long induces a sharp 0.9 dB margin drop when the first short wavelength is added due to high NF, resulting in temporary negative margin that increases the risk of service interruption and operational complexity, though this channel's margin recovers as more transponders are added. All orders converge at full loading of C and C+L band.

Fig. 7.3(c) shows capacity with ZR at 34 dB span loss. Central-to-edge achieves the highest capacity at 47.2 Tbps—10.4 Tbps more than long-to-short. Counter-intuitively, adding TRX does not always increase capacity as the system reacts to the changing load. Highest capacity is achieved with 66 ZRs for central-to-edge loading.

7.6.2. Capacity Analysis

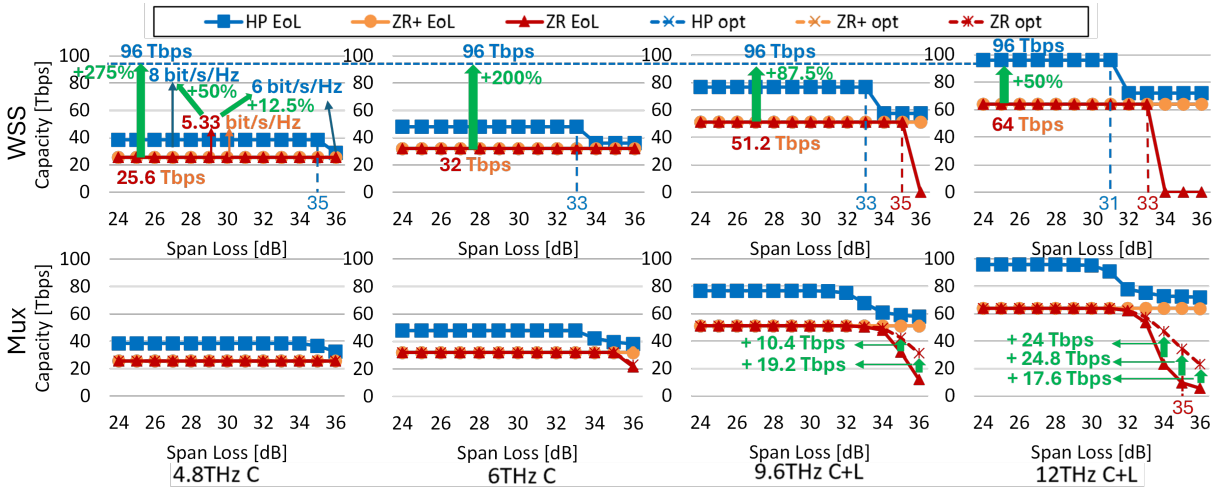


Figure 7.4: Capacity analysis.

With ZR, channel capacity is binary (either 800 Gbps or 0), while ZR+ and HP support multiple rates via adaptive modulation. We compare total capacity across all combinations of transponder type, Mux/WSS configuration, C/C+L bandwidth, and EoL/optimal loading (Mux only).

Fig. 7.4 shows HP achieves the highest capacity in all scenarios. With WSS + ASE loading at EoL (top row), HP reaches 8 bit/s/Hz SE using PCS-64QAM for span losses $\leq 35/33/33/31$ dB at 4.8/6/9.6/12 THz—outperforming ZR and ZR+ (SE = 5.33 bit/s/Hz) by 50% with the same bandwidth. Beyond these thresholds, HP operates at 6 bit/s/Hz—still 12.5% higher than ZR/ZR+.

ZR+ maintains maximum rate across all span losses up to 36 dB using PCS-16QAM, while ZR begins degrading at 35 dB with 16QAM in bandwidths ≥ 9.6 THz. In typical commercial cases, HP with 12 THz achieves 275% higher capacity than ZR at 4.8 THz, and 87.5% more than ZR+ at 9.6 THz, thanks to larger total bandwidth and SE (but with higher cost and power consumption).

Mux-based systems follow similar trends at EoL (Fig.7.4, bottom row). However, optimal loading (order and transponder number) significantly optimizes capacity for ZR with binary rate. Fig. 7.4 (bottom row) shows ZR gains up to 24.8 Tbps capacity at 35 dB span loss with optimal loading vs. EoL loading. In contrast, ZR+ shows no gain due to operating at maximum rate, and HP is unaffected by loading due to adaptive modulation.

7.7. Conclusions

We compared the capacity of ZR, ZR$^+$, and HP transponders in DCI networks under varying span losses, bandwidths, Mux/WSS configurations, and loading strategies. For the same bandwidth, HP offers 50% more capacity than ZR/ZR$^+$ at span loss $\leq$ 31 dB, and 12.5% more capacity beyond that. In Mux-based systems, optimal loading strategy improves ZR capacity by up to 24.8 Tbps. This highlights the importance of key design choices to maximize DCI performance.

8 | Conclusion

8.1. Conclusions and Future Work

8.1.1. Conclusions

This thesis has addressed the fundamental challenge of sustaining reliable Quality of Transmission (QoT) in optical networks under dynamic loading, heterogeneous spans, and limited observability. The contributions span from experimental studies to the development of novel monitoring and refinement techniques, as well as design insights for emerging Data Center Interconnect (DCI) networks.

First, we demonstrated experimentally that the widely adopted "set-and-forget" service allocation strategy significantly degrades established services during network reconfiguration, and that both static and dynamic power re-optimization strategies can effectively mitigate such impairments.

Second, we advanced the fidelity of digital twins for optical networks by proposing a family of input refinement (IR) techniques, each offering unique capabilities:

- **Passive Input Refinement (PIR):** A non-intrusive approach that leverages one snapshot and the SRS effect to refine insertion losses and amplifier gains at the Optical Multiplex Section (OMS) level, extended from C-band to C+L-band networks.
- **Active Input Refinement (AIR):** A probing method that actively adjust amplifier gain to induce measurable SRS variations, enabling span-level loss estimation and anomaly localization.
- **Incremental Input Refinement (IIR):** A progressive method that exploits multiple network snapshots to refine uncertain parameters over time, achieving robustness even under partial-load conditions.
- **Hybrid IR + Power Profile Estimation (PPE):** An integrated framework that combines IR and PPE to jointly improve insertion loss estimation, longitudinal power profiling, anomaly detection, and QoT prediction.

Their integration into an SDN control plane demonstrated the practicality of automated monitoring, refinement, and closed-loop QoT optimization.

Third, we provided system-level design guidelines for short-reach DCI networks by benchmarking ZR, ZR+, and high-performance transponders under realistic deployment scenarios. The results highlight the trade-offs between simplicity, cost, and performance, and demonstrate how intelligent service allocation strategies can unlock additional capacity in bandwidth-constrained DCI environments.

Together, these four techniques form a complementary toolkit: PIR provides OMS-level visibility in single- or multi-band systems, AIR extends monitoring granularity to the span level, IIR enables robust refinement during network evolution or partial loading, and IR+PPE integrates complementary observability sources to maximize accuracy and reliability in realistic networks.

Overall, this thesis bridges analytical modeling, experimental validation, and system-level design, demonstrating how refined monitoring, digital twins, and closed-loop optimization collectively enable the vision of *large-capacity, robust, and automated optical networks*.

8.1.2. Future Work

While the contributions of this thesis represent important steps toward scalable and automated optical networks, several promising research directions remain open:

- **Scalability and real-time operation:** Extending input refinement and closed-loop optimization to large-scale networks will require further advances in algorithmic efficiency, distributed orchestration, and real-time execution.
- **Ultra-wideband systems:** As network operators increasingly deploy C+L and potentially S-band extensions, refinement and optimization algorithms must be adapted to account for stronger inter-band stimulated Raman scattering, complex amplifier chains, and spectrum management challenges.
- **AI-driven refinement and control:** Large language models (LLMs) and advanced machine learning approaches hold the potential to further automate decision-making by learning correlations across monitoring data, digital twins, and historical network states. Integrating AI-driven reasoning with physics-informed models may enable faster convergence and improved robustness.
- **Service-aware and cross-layer optimization:** Future networks will demand not only physical-layer QoT guarantees but also application-aware performance metrics,

such as latency or availability for distributed AI workloads. Extending refinement and optimization to jointly consider physical- and higher-layer constraints remains a critical avenue.

- **Practical deployment and field trials:** Moving from laboratory testbeds to operational networks requires addressing practical challenges such as limited observability, compatibility with vendor equipment, and operational overheads. Field demonstrations in collaboration with network operators will be crucial to validate the feasibility and benefits of the proposed techniques.
- **Evolution of DCI networks:** As DCI demand continues to grow, further work is needed on benchmarking emerging coherent pluggables (e.g., 1.6T-class modules), dynamic bandwidth allocation schemes, and the interaction between physical-layer optimization and traffic engineering.

In summary, this thesis demonstrates that accurate monitoring, parameter refinement, and closed-loop optimization constitute the foundation of next-generation optical infrastructures. By integrating analytical modeling, advanced monitoring, and AI-driven control within a comprehensive digital twin, future research can further advance the scalability, resilience, and automation of optical networks—ultimately achieving the vision of *large-capacity, robust, and automated optical networks*.

Copyright Statement

In reference to IEEE copyrighted material which is used with permission in this thesis, the IEEE does not endorse any of Politecnico di Milano's products or services. Internal or personal use of this material is permitted.

If interested in reprinting/republishing IEEE copyrighted material for advertising or promotional purposes, or for creating new collective works for resale or redistribution, please visit: `http://www.ieee.org/publications_standards/publications/rights/rights_link.html` to learn how to obtain a License from RightsLink.

If applicable, University Microfilms and/or ProQuest Library, or the Archives of Canada, may supply single copies of the dissertation.

Bibliography

[1] J. Albert, M. Fokine, and W. Margulis. Grating formation in pure silica-core fibers. *Opt. Lett.*, 27:809–811, 2002.

[2] A. Amari, O. A. Dobre, R. Venkatesan, O. S. Kumar, P. Ciblat, and Y. Jaouën. A survey on fiber nonlinearity compensation for 400 gb/s and beyond optical communication systems. *IEEE Communications Surveys & Tutorials*, 19(4):3097–3113, 2017.

[3] R. Ayassi, A. Triki, M. Laye, E. L. Rouzic, N. Crespi, and R. Minevra. Bayesian optimization-based algorithm to improve the quality of transmission estimation. *Advanced Photonics Congress*, pages 1–3, 2021.

[4] R. Ayassi, X. Yang, C. Sun, Y. Pointurier, and G. Charlet. Filtering impairments-aware digital twin for snr prediction over network life-cycle. *Optical Fiber Communication Conference (OFC)*, pages 1–3, 2025.

[5] S. Azodolmolky, M. Klinkowski, E. Marin, D. Careglio, J. S. Pareta, and I. Tomkos. A survey on physical layer impairments aware routing and wavelength assignment algorithms in optical networks. *Computer networks*, 53(7):926–944, 2009.

[6] S. Azodolmolky, J. Perelló, M. Angelou, F. Agraz, L. Velasco, and S. Spadaro. Experimental demonstration of an impairment aware network planning and operation tool for transparent/translucent optical networks. *J. Light. Technol.*, 29:439–448, 2011.

[7] D. Azzimonti, C. Rottondi, A. Giusti, M. Tornatore, and A. Bianco. Comparison of domain adaptation and active learning techniques for quality of transmission estimation with small-sized training datasets [invited]. *J. Opt. Commun. Netw.*, 13: A56–A66, 2021.

[8] M. Barnoski, M. Rourke, S. Jensen, and R. Melville. Optical time domain reflectometer. *Applied optics*, 16(9):2375–2379, 1977.

[9] P. M. Becker, A. A. Olsson, and J. R. Simpson. *Erbium-doped fiber amplifiers: fundamentals and technology*. Elsevier, 1999.

[10] S. Bigo, S. Gauchard, A. Bertaina, and J. P. Hamaide. Experimental investigation of stimulated raman scattering limitation on wdm transmission over various types of fiber infrastructures. *Photonics Technology Letters*, 11:671–673, 1999.

[11] R. Borkowski, R. J. Duran, C. Kachris, D. Siracusa, A. Caballero, and N. Fernandez. Cognitive optical network testbed: Eu project chron. *J. Opt. Commun. Netw.*, 7: A344–A355, 2015.

[12] G. Borraccini, A. D'Amico, S. Straullu, A. Nespola, S. Piciaccia, A. Tanzi, G. Galimberti, S. Bottacchi, S. Swail, and V. Curri. Cognitive and autonomous qot-driven optical line controller. *J. Opt. Commun. Netw.*, 13:E23–E31, 2021.

[13] G. Borraccini, A. D'Amico, S. Straullu, F. Usmani, A. Ahmad, and V. Curri. Iterative supervised learning approach using transceiver bit-error-rate measurements for optical line system optimization. *J. Opt. Commun. Netw.*, 15:111–118, 2023.

[14] G. Borraccini, S. Straullu, A. Giorgetti, R. Ambrosone, E. Virgillito, A. D'Amico, R. D'Ingillo, F. Aquilino, A. Nespola, N. Sambo, F. Cugini, and V. Curri. Experimental demonstration of partially disaggregated optical network control using the physical layer digital twin. *IEEE Transactions on Network and Service Management*, 20:2343–2355, 2023.

[15] G. Borraccini, Y. Huang, A. D'Amico, T. F. de Lima, E. Ip, V. Curri, T. Wang, and K. Asahi. Optical line physical parameters calibration in presence of edfa total power monitors. *Optical Fiber Communication Conference (OFC)*, pages 1–3, 2024.

[16] C. A. Brackett, A. S. Acampora, J. Sweitzer, G. Tangonan, M. T. Smith, W. Lennon, K.-C. Wang, and R. H. Hobbs. A scalable multiwavelength multihop optical network: A proposal for research on all-optical networks. *Journal of lightwave technology*, 11(5/6):736–753, 1993.

[17] A. Caballero, J. C. Aguado, R. Borkowski, S. Saldaña, T. Jiménez, I. de Miguel, V. Arlunno, R. J. Durán, D. Zibar, J. B. Jensen, R. M. Lorenzo, E. J. Abril, and I. T. Monroy. Experimental demonstration of a cognitive quality of transmission estimator for optical communication systems. *European Conference on Optical Communication (ECOC)*, pages 1–3, 2012.

[18] A. Campanella, H. Okui, A. Mayoral, D. Kashiwa, O. G. de Dios, D. Verchere, Q. Pham Van, A. Giorgetti, R. Casellas, R. Morro, and L. Ong. Odtn: Open

disaggregated transport network. discovery and control of a disaggregated optical network through open source software and open apis. *Optical Fiber Communication Conference (OFC)*, pages 1–3, 2019.

[19] M. Cantono, R. Schmogrow, M. Newland, V. Vusirikala, and T. Hofmeister. Opportunities and challenges of c+l transmission systems. *J. Light. Technol.*, 38: 1050–1060, 2020.

[20] A. Carena, G. Bosco, V. Curri, Y. Jiang, P. Poggiolini, and F. Forghieri. Egn model of non-linear fiber propagation. *Opt. Express*, 13:16335–16362, 2014.

[21] S.-C. Chan and J.-M. Liu. Tunable narrow-linewidth photonic microwave generation using semiconductor laser dynamics. *IEEE Journal of Selected Topics in Quantum Electronics*, 10(5):1025–1032, 2004.

[22] J. Chang, C. Hahn, X. Tang, T. Zhao, W. C. Ng, and Z. Jiang. Demonstration of longitudinal power profile estimation using commercial transceivers and its practical consid-eration. *European Conference on Optical Communication (ECOC)*, pages 1–3, 2023.

[23] M. Z. Chowdhury, M. Shahjalal, M. K. Hasan, and Y. M. Jang. The role of optical wireless communication technologies in 5g/6g and iot solutions: Prospects, directions, and challenges. *Applied Sciences*, 9(20):4367, 2019.

[24] K. Christodoulopoulos, C. Delezoide, N. Sambo, A. Kretsis, I. Sartzetakis, A. Sgambelluri, N. Argyris, G. Kanakis, P. Giardina, G. Bernini, D. Roccato, A. Percelsi, R. Morro, H. Avramopoulos, P. Castoldi, P. Layec, and S. Bigo. Toward efficient, reliable, and autonomous optical networks: the orchestra solution [invited]. *J. Opt. Commun. Netw.*, 11:C10–C24, 2019.

[25] Z. Cui, Y. Song, X. Luo, S. Li, J. Li, M. Fu, C. Ju, J. Li, M. Zhang, and D. Wang. Optical fiber anomaly detection through srs-induced spectral tilt in c+l-band transmission systems. *J. Opt. Commun. Netw.*, 17:616–630, 2025.

[26] V. Curri. Gnpy model of the physical layer for open and disaggregated optical networking [invited]. *J. Opt. Commun. Netw.*, 14:C92–C104, 2022.

[27] M. Dallaglio, N. Sambo, F. Cugini, and P. Castoldi. Control and management of transponders with netconf and yang. *J. Opt. Commun. Netw.*, 7:B43–B52, 2017.

[28] A. D'Amico, B. Correia, and V. Curri. Extension of the local-optimization global-optimization (logo) launch power strategy to multi-band optical networks. *European Conference on Optical Communication (ECOC)*, pages 1–3, 2024.

[29] I. F. de Jauregui Ruiz, A. Ghazisaeidi, T. Zami, S. Louis, and B. Lavigne. An accurate model for system performance analysis of optical fibre networks with in-line filtering. *European Conference on Optical Communication (ECOC)*, pages 1–3, 2019.

[30] B. Debord, F. Amrani, L. Vincetti, F. Gérôme, and F. Benabid. Hollow-core fiber technology: The rising of "gas photonics". *Fibers*, 34:321–326, 2016.

[31] E. Desurvire, J. Zyskind, and C. Giles. Design optimization for efficient erbium-doped fiber amplifiers. *J. Lightwave Technol.*, 8(11):1730–1741, 1990.

[32] V. Dukic, G. Khanna, C. Gkantsidis, T. Karagiannis, F. Parmigiani, S. A, M. Filer, J. L. Cox, A. Ptasznik, N. Harland, W. Saunders, and C. Belady. Beyond the mega-data center: networking multi-data center regions. *Special Interest Group on Data Communication on the applications, technologies, architectures, and protocols for computer communication (SIGCOMM)*, 2020.

[33] N. Ellsworth, T. Zhang, S. Troia, G. Maier, and A. Fumagalli. Enhancing cross layer monitoring on open optical transport networks. *Optical Fiber Communication Conference (OFC)*, pages 1–3, 2023.

[34] Q. Fan, J. Lu, G. Zhou, D. Zeng, C. Guo, and L. Lu. Experimental comparisons between machine learning and analytical models for qot estimations in wdm systems. *Optical Fiber Communication Conference (OFC)*, pages 1–3, 2020.

[35] M. S. Faruk and S. J. Savory. Measurement informed models and digital twins for optical fiber communication systems. *J. Light. Technol.*, 42:1016–1030, 2024.

[36] I. Fatadin, D. Ives, and S. J. Savory. Blind equalization and carrier phase recovery in a 16-qam optical coherent system. *J. Lightwave Technol.*, 27(15):3042–3049, 2009.

[37] Y. Feng, B. Li, and B. Li. Jetway: minimizing costs on inter-datacenter video traffic. In *Proceedings of the 20th ACM International Conference on Multimedia*, page 259–268, New York, NY, USA, 2012. Association for Computing Machinery. ISBN 9781450310895. doi: 10.1145/2393347.2393388. URL `https://doi.org/10.1145/2393347.2393388`.

[38] Y. Feng, B. Li, and B. Li. Bargaining towards maximized resource utilization in video streaming datacenters. In *2012 Proceedings IEEE INFOCOM*, pages 1134–1142, 2012.

[39] A. Ferrari, D. Pilori, E. Virgillito, and V. Curri. Power control strategies in c+l

optical line systems. *Optical Fiber Communication Conference (OFC)*, pages 1–3, 2019.

[40] A. Ferrari, M. Filer, K. Balasubramanian, Y. Yin, E. L. Rouzic, J. Kundrát, G. Grammel, G. Galimberti, and V. Curri. Gnpy: an open source application for physical layer aware open optical networks. *J. Opt. Commun. Netw.*, 12:C31–C40, 2020.

[41] A. Ferrari, K. Balasubramanian, M. Filer, Y. Yin, E. L. Rouzic, J. Kundrat, G. Grammel, G. Galimberti, and V. Curri. Assessment on the in-field lightpath qot computation including connector loss uncertainties. *J. Opt. Commun. Netw.*, 13:A156–A164, 2021.

[42] A. Ferrari, V. V. Garbhapu, D. L. Gac, I. F. de Jauregui Ruiz, G. Charlet, and Y. Pointurier. Demonstration of ai-light: an automation framework to optimize the channel powers leveraging a digital twin. *Optical Fiber Communication Conference (OFC)*, pages 1–3, 2022.

[43] M. Filer, G. G. G. G. M. Cantono, A. Ferrari, and V. Curri. Multi-vendor experimental validation of an open source qot estimator for optical networks. *J. Light. Technol.*, 36:3073–3082, 2018.

[44] M. Filer, J. Gaudette, Y. Yin, D. Billor, Z. Bakhtiari, and J. L. Cox. Low-margin optical networking at cloud scale [invited]. *J. Opt. Commun. Netw.*, 11:C94–C108, 2019.

[45] M. Filer, J. Gaudette, Y. Yin, D. Billor, Z. Bakhtiari, and J. L. Cox. Low-margin optical networking at cloud scale [invited]. *J. Opt. Commun. Netw.*, 11:C94–C108, 2019.

[46] S. Frisken, G. Baxter, D. Abakoumov, H. Zhou, I. Clarke, and S. Poole. Flexible and grid-less wavelength selective switch using lcos technology. In *Optical Fiber Communication Conference (OFC)*, pages 1–3, 2011.

[47] H. Gao, X. Chen, L. Sun, and Z. Li. Compqote: Generalizing qot estimation with composable ml and end-to-end learning. *Optical Fiber Communication Conference (OFC)*, pages 1–3, 2023.

[48] V. V. Garbhapu, A. Ferrari, I. F. de Jauregui Ruiz, D. L. Gac, G. Charlet, and Y. Pointurier. Network-wide snr-based channel power optimization. *European Conference on Optical Communication (ECOC)*, pages 1–3, 2021.

[49] O. Ghandour, S. E. Kafhali, and M. Hanini. Computing resources scalability per-

formance analysis in cloud computing data center. *Journal of Grid Computing*, 26: 61, 2023.

[50] K. Ghodsifar, F. Arpanaei, H. Beyranvand, M. R. Zefreh, C. Natalino, and P. Monti. Ml-assisted optimal power and gsnr estimation in multi-band elastic optical networks. *International Conference on Transparent Optical Networks (ICTON)*, pages 1–4, 2024.

[51] C. R. Giles and E. Desurvire. Modeling erbium-doped fiber amplifiers. *J. Lightwave Technol.*, 9(2):271–283, 2002.

[52] E. Hartling, A. Pilipetskii, D. Evans, E. Mateo, M. Salsi, P. Pecci, and P. Mehta. Design, acceptance and capacity of subsea open cables. *J. Light. Technol.*, 39(3): 742–756, 2021.

[53] J. R. Hayes, S. R. Sandoghchi, T. D. Bradley, Z. Liu, R. Slavík, M. A. Gouveia, N. V. Wheeler, G. Jasion, Y. Chen, E. N.Fokoua, M. N. Petrovich, D. J. Richardson, and F. Poletti. Antiresonant hollow core fiber with an octave spanning bandwidth for short haul data communications. *J. Lightwave Technol.*, 35:437–442, 2017.

[54] K. Hazelwood, S. Bird, D. Brooks, S. Chintala, U. Diril, D. Dzhulgakov, M. Fawzy, B. Jia, Y. Jia, A. Kalro, J. Law, K. Lee, J. Lu, P. Noordhuis, M. Smelyanskiy, L. Xiong, and X. Wang. Applied machine learning at facebook: A datacenter infrastructure perspective. In *IEEE International Symposium on High Performance Computer Architecture (HPCA)*, pages 620–629, 2018.

[55] J. He, A. Chaintreau, and C. Diot. A performance evaluation of scalable live video streaming with nano data centers. *Computer Networks*, 53:153–167, 2009.

[56] Y. He, Z. Zhai, L. Dou, L. Wang, Y. Yan, C. Xie, C. Lu, , and A. P. T. Lau. Improved qot estimations through refined signal power measurements and data-driven parameter optimizations in a disaggregated and partially loaded live production network. *J. Opt. Commun. Netw.*, 15:638–648, 2023.

[57] L. Hollberg and M. Ohtsu. Modulatable narrow-linewidth semiconductor lasers. *Appl. Phys. Lett.*, 53:944–946, 1988.

[58] M. Ibrahimi, H. Abdollahi, C. Rottondi, A. Giusti, A. Ferrari, and V. Curri. Machine learning regression for qot estimation of unestablished lightpaths. *J. Opt. Commun. Netw.*, 13:B92–B101, 2021.

[59] M. N. Islam. Raman amplifiers for telecommunications. *Journal of selected topics in Quantum Electronics*, 8(3):548–559, 2002.

[60] G. J and J. R. Machine learning applications for data center optimiza-tion. Technical report, Google, 2014. Available: `https://static.googleusercontent.com/media/research.google.com/en//pubs/archive/42542.pdf`.

[61] M. K. Jackson Ramphela, P. A. Owolawi, T. Mapayi, and G. Aiyetoro. Internet of things (iot) integrated data center infrastructure monitoring system. In *2020 International Conference on Artificial Intelligence, Big Data, Computing and Data Communication Systems (icABCD)*, pages 1–6, 2020.

[62] H. Kanamori, H. Yokota, G. Tanaka, M. Watanabe, Y. Ishiguro, I. Yoshida, T. Kakii, S. Itoh, Y. Asano, and S. Tanaka. Transmission characteristics and reliability of pure-silica-core single-mode fibers. *J. Light. Technol.*, 4:1144–1150, 1986.

[63] O. Karandin, A. Ferrari, F. Musumeci, Y. Pointurier, and M. Tornatore. Probabilistic low-margin optical-network design with multiple physical-layer parameter uncertainties. *J. Opt. Commun. Netw.*, 15:C129–C137, 2023.

[64] A. Katal, S. Dahiya, and T. Choudhury. Energy efficiency in cloud computing data centers: a survey on software technologies. *Cluster Computing*, 26:1845–1875, 2023.

[65] H. Kidorf, K. Rottwitt, M. Nissov, M. Ma, and E. Rabarijaona. Pump interactions in a 100-nm bandwidth raman amplifier. *Technology Letters*, 11(5):530–532, 1999.

[66] J. Konečný, B. McMahan, and D. Ramage. Federated optimization:distributed optimization beyond the datacenter. *arXiv*, 2015.

[67] R. Kraemer, F. Nakamura, M. Van Den Hout, S. Van Der Heide, C. Okonkwo, H. Tsuda, A. Napoli, and N. Calabretta. Multi-band photonic integrated wavelength selective switch. *J. Lightwave Technol.*, 39(19):6023–6032, 2021.

[68] J. Kundrát, J. Vojtěch, P. Škoda, R. Vohnout, J. Radil, and O. Havliš. Yang/netconf roadm: Evolving open dwdm toward sdn applications. *J. Light. Technol.*, 36:3105–3114, 2018.

[69] Y. l. Bogomolov and A. D. Yunakovsky. Split-step fourier method for nonlinear schrodinger equation. *DAYS on DIFFRACTION*, pages 34–42, 2006.

[70] S. E. Landero, I. F. de Jauregui Ruiz, A. Ferrari, D. L. Gac, Y. Frignac, and G. Charlet. Link power optimization for s+c+l multi-band wdm coherent transmission systems. *Optical Fiber Communication Conference (OFC)*, pages 1–3, 2022.

[71] P. Layec, A. Dupas, D. Verchère, K. Sparks, and S. Bigo. Will metro networks

be the playground for (true) elastic optical networks? *J. Light. Technol.*, 35(6): 1260–1266, 2017.

[72] Y. Li, J. Lin, L. Zong, S. K. Bose, B. Mukherjee, and G. Shen. Colorless, partially directionless, and contentionless architecture for high-degree roadms. *Journal of Optical Communications and Networking*, 14(6):481–492, 2022.

[73] Y. Lin, S. Han, H. Mao, Y. Wang, and W. Dally. Deep gradient compression: Reducing the communication bandwidth for distributed training. In *arXiv*, 2018.

[74] Q. Liu, Y. Ma, M. Alhussein, Y. Zhang, and L. Peng. Green data center with iot sensing and cloud-assisted smart temperature control system. *Future Generation Computer Systems*, 20(4):1408–1416, 2013.

[75] X. Liu. Enabling optical network technologies for 5g and beyond. *J. Light. Technol.*, 40(2):358–367, 2022.

[76] X. Liu, Y. Wang, X. Wang, H. Xu, C. Li, and X. Xin. Bi-directional gated recurrent unit neural network based nonlinear equalizer for coherent optical communication system. *Optics Express*, 29(4):5923–5933, 2021.

[77] X. Liu, Q. Qiu, Y. Zhang, M. Cai, Y. Liu, L. Yi, W. Hu, and Q. Zhuge. Auto-dtwave: Digital twin-aided autonomous optical network operation with continuous wavelength loading. *Optical Fiber Communication Conference (OFC)*, pages 1–3, 2024.

[78] X. Liu, Q. Qiu, Y. Zhang, Y. Cheng, L. Yi, W. Hu, and Q. Zhuge. First field trial of llm-powered ai agent for lifecycle management of autonomous driving optical networks. *Optical Fiber Communication Conference (OFC)*, pages 1–3, 2025.

[79] J. Lu, G. Zhou, Q. Fan, D. Zeng, C. Guo, L. Lu, J. Li, C. Xie, C. Lu, F. N. Khan, and A. P. T. Lau. Performance comparisons between machine learning and analytical models for quality of transmission estimation in wavelength-division-multiplexed systems [invited]. *J. Opt. Commun. Netw.*, 13:B35–B44, 2021.

[80] A. Marathe, R. Harris, D. K. Lowenthal, B. R. de Supinski, B. Rountree, M. Schulz, and X. Yuan. A comparative study of high-performance computing on the cloud. In *22nd international symposium on High-performance parallel and distributed computin*, page 239–250. Association for Computing Machinery, 2013. ISBN 9781450319102.

[81] V. Mauch, M. Kunze, and M. Hillenbrand. High performance cloud computing. *Future Generation Computer Systems*, 20(4):1408–1416, 2013.

[82] A. May, F. Boitier, A. Courilleau, B. A. Ayoubi, and P. Layec. Demonstration of enhanced power losses characteri-zation in optical networks. *Optical Fiber Communication Conference (OFC)*, pages 1–3, 2022.

[83] G. Mehta, G. Mittra, and V. K. Yadav. Application of iot to optimize data center operations. In *2018 International Conference on Computing, Power and Communication Technologies (GUCON)*, pages 738–742, 2018. doi: 10.1109/GUCON.2018.8674939.

[84] R. M. Morais and J. Pedro. Machine learning models for estimating quality of transmission in dwdm networks. *J. Opt. Commun. Netw.*, 10:D84–D99, 2018.

[85] N. Morette, I. F. de Jauregui Ruiz, and Y. Pointurier. Leveraging ml-based qot tool parameter feeding for accurate wdm network performance prediction. *Optical Fiber Communication Conference (OFC)*, pages 1–3, 2021.

[86] N. Morette, I. F. de Jauregui Ruiz, H. Hafermann, and Y. Pointurier. On the robustness of a ml-based method for qot tool parameter refinement in partially loaded networks. *Optical Fiber Communication Conference (OFC)*, pages 1–3, 2022.

[87] N. Morette, H. Hafermann, Y. Frignac, and Y. Pointurier. Machine learning enhancement of a digital twin for wavelength division multiplexing network performance prediction leveraging quality of transmission parameter refinement. *J. Opt. Commun. Netw.*, 15:333–343, 2023.

[88] J. Müller, T. Fehenberger, S. K. Patri, K. Kaeval, H. Griesser, and M. Tikas. Estimating quality of transmission in a live production network using machine learning. *Optical Fiber Communication Conference (OFC)*, pages 1–3, 2021.

[89] L. Nadal, J. M. Fabrega, M. S. Moreolo, F. J. Vilchez, R. Casellas, R. Munoz, R. Vilalta, and R. Martinez. Programmable disaggregated multi-dimensional s-bvt as an enabler for high capacity optical metro networks. *J. Opt. Commun. Netw.*, 13(6):C31–C40, 2021.

[90] S. Namiki and Y. Emori. Ultrabroad-band raman amplifiers pumped and gain-equalized by wavelength-division-multiplexed high-power laser diodes. *Journal of Selected Topics in Quantum Electronics*, 7(1):3–16, 2002.

[91] A. Napoli, N. Costa, J. K. Fischer, J. Pedro, S. Abrate, N. Calabretta, W. Forysiak, E. Pincemin, J. P.-P. Gimenez, C. Matrakidis, et al. Towards multiband optical systems. In *Photonic Networks and Devices*, pages NeTu3E–1. Optica Publishing Group, 2018.

[92] K. N. Oh and Y. O. Chin. Modified constant modulus algorithm: blind equalization and carrier phase recovery algorithm. In *Proceedings IEEE International Conference on Communications ICC'95*, volume 1, pages 498–502. IEEE, 1995.

[93] OIF. Implementation agreement 400zr. Technical report, Optical Internetworking Forum, Nov. 2022. Available: `https://www.oiforum.com/wp-content/uploads/OIF-400ZR-01.0_reduced2.pdf`.

[94] OIF. Implementation agreement for 800zr coherent interfaces. Technical report, Optical Internetworking Forum, Oct. 2024. Available: `https://www.oiforum.com/oif-releases-800zr-coherent-interface-implementation-agreement-ia-and-key-400zr-ia`

[95] T. Panayiotou, G. Savva, B. Shariati, I. Tomkos, and G. Ellinas. Machine learning for qot estimation of unseen optical network states. *Optical Fiber Communication Conference (OFC)*, pages 1–3, 2019.

[96] Y. X. Pang, Y. Song, Y. Wang, Y. Zhou, H. Zhu, L. Zhang, Y. Fan, Z. Guo, S. Huang, M. Zhang, and D. Wang. Optical power control for gsnr optimization based on c+l-band digital twin systems. *J. Light. Technol.*, 42:95–105, 2025.

[97] F. Paolucci, A. Sgambelluri, F. Cugini, and P. Castoldi. Network telemetry streaming services in sdn-based disaggregated optical networks. *J. Light. Technol.*, 36(15): 3142–3149, 2018.

[98] Y. Pei, A. W. Mackay, M. Boroojerdi, J. Archambault, and D. W. Boertjes. Characterizing fiber nonlinearity with deployed equip-ment in optical line systems. *Optical Fiber Communication Conference (OFC)*, pages 1–3, 2024.

[99] J. Pesic, T. Zami, and N. Rossi. Cost savings for low design margins in wdm elastic networks. *Advanced Photonics*, 2018.

[100] J. Pesic, M. Lonardi, E. Seve, N. Rossi, and T. Zami. Transfer learning from unbiased training data sets for qot estimation in wdm networks. *European Conference on Optical Communication (ECOC)*, pages 1–4, 2020.

[101] P. Poggiolini, G. Bosco, A. Carena, V. Curri, Y. Jiang, and F. Forghieri. The gn-model of fiber non-linear propagation and its applications. *J. Light. Technol.*, 32 (4):694–721, 2014.

[102] Y. Pointurier. Design of low-margin optical networks. *J. Opt. Commun. Netw.*, 9: A9–A17, 2017.

[103] Y. Pointurier. Machine learning techniques for quality of transmission estimation in optical networks. *J. Opt. Commun. Netw.*, 13:B60–B71, 2021.

[104] Q. Qiu, X. Liu, Y. Zhang, L. Yi, W. Hu, and Q. Zhuge. Heuristic optimization strategies for reliable amplifier reconfiguration in autonomous optical networks with field-trial validation. *J. Light. Technol.*, pages 1–12, 2025.

[105] A. Raj, Z. Wang, F. Slyne, T. Chen, D. Kilper, and M. Ruffini. Self-normalizing neural network, enabling one shot transfer learning for modeling edfa wavelength dependent gain. *European Conference on Optical Communication (ECOC)*, pages 1–3, 2023.

[106] G. Rizzelli, G. Maier, M. Quagliotti, M. Schiano, and A. Pattavina. Assessing the scalability of next-generation wavelength switched optical networks. *Journal of lightwave technology*, 32(12):2263–2270, 2014.

[107] I. Roberts, J. M. Kahn, and D. Boertjes. Convex channel power optimization in nonlinear wdm systems using gaussian noise model. *J. Light. Technol.*, 34(13): 3212–3222, 2016.

[108] C. Rottondi, L. Barletta, A. Giusti, and M. Tornatore. Machine-learning method for quality of transmission prediction of unestablished lightpaths. *J. Opt. Commun. Netw.*, 10:A286–A297, 2018.

[109] C. Rottondi, R. di Marino, M. Nava, A. Giusti, and A. Bianco. On the benefits of domain adaptation techniques for quality of transmission estimation in optical networks. *J. Opt. Commun. Netw.*, 13:A34–A43, 2021.

[110] N. Sambo, K. Christodoulopoulos, N. Argyris, P. Giardina, C. Delezoide, and D. Roccato. Field trial: Demonstrating automatic reconfiguration of optical networks based on finite state machine. *J. Light. Technol.*, 37:4090–4097, 2019.

[111] N. Sambo, A. Ferrari, A. Napoli, N. Costa, J. Pedro, B. Sommerkorn-Krombholz, P. Castoldi, and V. Curri. Provisioning in multi-band optical networks. *Journal of Lightwave Technology*, 38(9):2598–2605, 2020.

[112] T. Sasai, M. Nakamura, E. Yamazaki, S. Yamamoto, H. Nishizawa, and Y. Kisaka. Digital longitudinal monitoring of optical fiber communication link. *J. Light. Technol.*, 40:2390–2408, 2022.

[113] T. Sasai, M. Nakamura, E. Yamazaki, S. Yamamoto, H. Nishizawa, and Y. Kisaka. Performance limit of fiber-longitudinal power profile estimation methods. *J. Light. Technol.*, 41:3278–3289, 2023.

[114] T. Sasai, G. Borraccini, Y. K. Huang, H. Nishizawa, Z. Wang, T. Chen, Y. Sone, T. Matsumura, M. Nakamura, E. Yamazaki, and Y. Kisaka. 4d optical link tomography: First field demonstration of autonomous transponder capable of distance, time, frequency, and polarization resolved monitoring. *Optical Fiber Communication Conference (OFC)*, pages 1–3, 2024.

[115] T. Sasai, M. Nakamura, E. Yamazaki, S. Yamamoto, H. Nishizawa, and Y. Kisaka. S+c+l high-capacity transmission systems: Chal-lenges and opportunities. *J. Light. Technol.*, 42:4260–4270, 2024.

[116] S. J. Savory, G. Gavioli, R. I. Killey, and P. Bayvel. Electronic compensation of chromatic dispersion using a digital coherent receiver. *Optics express*, 15(5):2120–2126, 2007.

[117] D. Semrau, R. I. Killey, and P. Bayvel. The gaussian noise model in the presence of inter-channel stimulated raman scattering. *J. Light. Technol.*, 34(13):3212–3222, 2016.

[118] D. Sequeira, M. Ruiz, N. Costa, A. Napoli, J. Pedro, and L. Velasco. Machine-learning method for quality of transmission prediction of unestablished lightpaths. *J. Opt. Commun. Netw.*, 15:87–97, 2023.

[119] E. Seve, J. Pesic, and Y. Pointurier. Associating machine-learning and analytical models for quality of transmission estimation: combining the best of both worlds. *J. Opt. Commun. Netw.*, 13:C21–C30, 2021.

[120] A. Sgambelluri, A. Giorgetti, D. Scano, F. Cugini, and F. Paolucci. Openconfig and openroadm automation of operational modes in disaggregated optical networks. *EEE Access*, 8:190094–190107, 2020.

[121] T. Sharma, A. Chehri, and P. Fortier. Review of optical and wireless backhaul networks and emerging trends of next generation 5g and 6g technologies. *Transactions on Emerging Telecommunications Technologies*, 32:2161–3915, 2021.

[122] Y. Song, Q. Fan, C. Lu, D. Wang, and A. P. Tao. Efficient three-step amplifier configuration algorithm for dynamic c+l-band links in presence of stimulated raman scattering. *J. Light. Technol.*, 41:1445–1453, 2023.

[123] C. Sun, X. Yang, G. Charlet, P. A. Stavrou, and Y. Pointurier. Digital twin-enabled optical network automation: Power re-optimization. *Optical Fiber Communication Conference (OFC)*, pages 1–3, 2024.

[124] C. Sun, X. Yang, N. D. Cicco, R. Ayassi, V. Garbhapu, P. A. Stavrou, M. Tornatore,

G. Charlet, and Y. Pointurier. First experimental demonstration of full lifecycle auto-mation of optical network through fine-tuned llm and digital twin. *European Conference on Optical Communication (ECOC)*, pages 1–3, 2024.

[125] C. Sun, X. Yang, G. Charlet, P. A. Stavrou, and Y. Pointurier. Digital twin-enabled multi-step strategies for autonomous power equalization in optical networks. *J. Opt. Commun. Netw.*, 17:C41–C50, 2025.

[126] C. Sun, X. Yang, N. D. Cicco, R. Ayassi, V. V. Garbhapu, P. A. Stavrou, M. Tornatore, G. Charlet, , and Y. Pointurier. Experimental demonstration of local ai-agents for lifecycle management and control automation of optical networks. *J. Opt. Commun. Netw.*, 17:C82–C92, 2025.

[127] T. Tanimura, K. Tajima, S. Yoshida, S. Oda, and T. Hoshida. Experimental demonstration of a coherent receiver that visualizes longitudinal signal power profile over multiple spans out of its incoming signal. *European Conference on Optical Communication (ECOC)*, pages 1–3, 2019.

[128] F. Tavernier and M. S. Steyaert. High-speed optical receivers with integrated photodiode in 130 nm cmos. *IEEE Journal of Solid-State Circuits*, 44(10):2856–2867, 2009.

[129] C. A. Thraskias, E. N. Lallas, N. Neumann, L. Schares, B. J. Offrein, R. Henker, D. Plettemeier, F. Ellinger, J. Leuthold, and I. Tomkos. Survey of photonic and plasmonic interconnect technologies for intra-datacenter and high-performance computing communications. *IEEE Communications Surveys Tutorials*, 20(4):2758–2783, 2018.

[130] S. Tibuleac and M. Filer. Transmission impairments in dwdm networks with reconfigurable optical add-drop multiplexers. *J. Lightwave Technol.*, 28(4):557–568, 2010.

[131] M. A. Tran, D. H., and J. E. Bowers. Tutorial on narrow linewidth tunable semiconductor lasers using si/iii-v heterogeneous integration. *Appl. Phys. Lett.*, 4:111101, 2019.

[132] F. Usmani, I. Khan, M. U. Masood, A. Ahmad, M. Shahzad, and V. Curri. Convolutional neural network for quality of transmission prediction of unestablished lightpaths. *Microwave and Optical Technology Letters*, 63:2461–2469, 2021.

[133] L. Velasco, A. Sgambelluri, R. Casellas, L. Gifre, J. Izquierdo-Zaragoza, and F. Fresi.

Building autonomic optical whitebox-based networks. *J. Light. Technol.*, 36:3097–3104, 2018.

[134] R. Vilalta, L. Gifre, R. Casellas, R. Muñoz, R. Martínez, and A. Mozo. Applying digital twins to optical networks with cloud-native sdn controllers. *IEEE Communications Magazine*, 61(12):128–134, 2023.

[135] E. Virgillito, R.-P. Braun, D. Breuer, A. Gladisch, V. Curri, and G. Grammel. Testing tip open source solutions in deployed optical networks. In *Optical Fiber Communication Conference (OFC)*, pages 1–3, 2021.

[136] B. Wang, Z. Qi, R. Ma, H. Guan, and A. V. Vasilakos. A survey on data center networking for cloud computing. *Computer Networks*, 91:528–547, 2015.

[137] D. Wang, Z. Zhang, M. Zhang, M. Fu, J. Li, and S. Cai. The role of digital twin in optical communication: Fault management, hardware configuration, and transmission simulation. *IEEE Communications Magazine*, 59:133–139, 2021.

[138] D. Wang, Y. Song, Y. Zhang, X. Jiang, J. Dong, F. Khan, T. Sasai, S. Huang, A. P. T. Lau, M. Tornatore, and M. Zhang. Digital twin of optical networks: A review of recent advances and future trends. *J. Light. Technol.*, 42:4233–4259, 2024.

[139] M. Wang, L. Zong, L. Mao, A. Marquez, Y. Ye, H. Zhao, and F. J. Vaquero Caballero. Lcos slm study and its application in wavelength selective switch. In *Photonics*, volume 4, page 22. MDPI, 2017.

[140] R. Wang, J. Zhang, Z. Gu, M. Ibrahimi, B. Zhang, F. Musumeci, M. Tornatore, and Y. Ji. Digital-twin-assisted meta learning for soft-failure localization in roadm-based optical networks. *J. Opt. Commun. Netw.*, 16(3):C11–C19, 2024.

[141] Z. Wang, Y. K. Huang, S. Han, T. Wang, D. Kilper, and T. Chen. Multi-span optical power spectrum prediction using ml-based edfa models and cascaded learning. *Optical Fiber Communication Conference (OFC)*, pages 1–3, 2024.

[142] J. Wass, J. Thrane, M. Piels, R. Jones, and D. Zibar. Gaussian process regression for wdm system performance prediction. *Optical Fiber Communication Conference (OFC)*, pages 1–3, 2017.

[143] A. E. Willner, Z. Pan, and C. Yu. Optical performance monitoring. In *Optical fiber telecommunications VB*, pages 233–292. Elsevier, 2008.

[144] L. Xia, J. Zhang, S. Hu, M. Zhu, Y. Song, and K. Qiu. Transfer learning assisted deep neural network for osnr estimation. *Opt. Express*, 27:19398–19406, 2019.

[145] C. Xie and B. Zhang. Scaling optical interconnects for hyperscale data center networks. *Proceedings of the IEEE*, 110:1699–1713, 2022.

[146] T. Xu, G. Jacobsen, S. Popov, J. Li, E. Vanin, K. Wang, A. T. Friberg, and Y. Zhang. Chromatic dispersion compensation in coherent transmission system using digital filters. *Optics express*, 18:16243–16257, 2010.

[147] Y. Yamamoto, Y. Kawaguchi, and M. Hirano. Low-loss and low-nonlinearity pure-silica-core fiber for c- and l-band broadband transmission. *J. Light. Technol.*, 34: 321–326, 2016.

[148] R. Yang, S. Shen, H. Li, Z. Shi, R. Wang, R. Nejabati, S. Yan, and D. Simeonidou. 986 km field trial of cascaded ann-based link penalty models for qot prediction. *Optical Fiber Communication Conference (OFC)*, pages 1–3, 2023.

[149] X. Yang, A. Ferrari, N. Morette, D. L. Gac, S. E. Landero, G. Charlet, and Y. Pointurier. Experimental impact of power re-optimization in a mesh network. *European Conference on Optical Communication (ECOC)*, pages 1–3, 2022.

[150] X. Yang, A. Ferrari, D. L. Gac, G. Charlet, M. Tornatore, and Y. Pointurier. Experimental impact of power re-optimization in a mesh network. *J. Opt. Commun. Netw.*, 15:C20–C28, 2023.

[151] X. Yang, A. Ferrari, N. Morette, and Y. Pointurier. Qot estimation improvement with inputs refinement tool for c+ l networks. *Optical Fiber Communication Conference (OFC)*, pages 1–3, 2023.

[152] X. Yang, T. Eldahrawy, C. Sun, A. Lorences-Riesgo, M. Tornatore, G. Charlet, and Y. Pointurier. Integrating ppe and inputs refinement for enhanced qot estimation and optimization in an optical mesh network. *European Conference on Optical Communication (ECOC)*, pages 1–3, 2024.

[153] X. Yang, C. Sun, G. Charlet, M. Tornatore, and Y. Pointurier. Digital-twin-based active input refinement for insertion loss estimation and qot optimization in c and c + l networks. *J. Opt. Commun. Netw.*, 16:1261–1274, 2024.

[154] X. Yang, C. Sun, G. Charlet, M. Tornatore, and Y. Pointurier. Digital twin-based insertion loss estimator for anomalous loss localization and network equalization enhancement. *Optical Fiber Communication Conference (OFC)*, pages 1–3, 2024.

[155] X. Yang, A. Lorences-Riesgo, S. Escobar-Landero, M. Tornatore, G. Charlet, and Y. Pointurier. Capacity scaling limits of dci networks: A comparative study of zr,

zr+, and high-performance transponders. *European Conference on Optical Communication (ECOC)*, pages 1–3, 2025.

[156] X. Yang, C. Sun, R. Ayassi, G. Charlet, M. Tornatore, and Y. Pointurier. Inputs refinement with incremental learning for accurate digital twin of optical networks. *Optical Fiber Communication Conference (OFC)*, pages 1–3, 2025.

[157] S. Yao, C. Hsu, L. Kong, Q. Zhou, S. Shen, and R. Zhang. Data efficient estimation for quality of transmission through active learning in fiber-wireless integrated network. *J. Light. Technol.*, 39:5691–5698, 2021.

[158] F. Yu, M. Xu, and J. C. Knight. Experimental study of low-loss single-mode performance in anti-resonant hollow-core fibers. *Opt. Express*, 24:12969–12975, 2016.

[159] F. Zeng, W. Gan, Y. Wang, and P. S. Yu. Distributed training of large language models. *International Conference on Parallel and Distributed Systems (ICPADS)*, pages 840–847, 2023.

[160] Y. Zhang, M. Zhang, Y. Song, Y. Shi, C. Zhang, C. Ju, B. Guo, S. Huang, and D. Wang. Building a digital twin for large-scale and dynamic c+l-band optical networks. *J. Opt. Commun. Netw.*, 15:985–998, 2023.

[161] Y. Zhang, X. Liu, Q. Qiu, Y. Liu, L. Yi, W. Hu, and Q. Zhuge. Mapping-finding input-parameter refinement paradigm for a dynamic multiband optical network digital twin: the raman amplifier modeling case. *J. Opt. Commun. Netw.*, 16:1059–1069, 2024.

[162] Z. Zhong, M. Ghobadi, M. Balandat, S. Katti, A. Kazerouni, J. Leach, M. McKillop, and Y. Zhang. Bow: First real-world demonstration of a bayesian optimization system for wavelength reconfiguration. *Optical Fiber Communication Conference (OFC)*, pages 1–3, 2021.

[163] J. Zhou, J. Lu, and C. Yu. Improving the accuracy of qot estimation with insertion loss distribution evaluation for c+l band transmission systems. *J. Opt. Commun. Netw.*, 16:12–20, 2024.

[164] Y. Zhou, K. Smith, J. Weatherhead, P. Weir, A. Lord, J. Chen, W. Pan, D. Tanasoiu, and S. Wu. Demonstration of a novel technique for non-intrusive in-band osnr derivation using flexible rate optical transponders over a live 727 km flexible grid optical link. *J. Light. Technol.*, 35(20):4399–4405, 2017.

[165] C. Zhu, R. H. Byrd, P. Lu, and J. Nocedal. Algorithm 778: L-bfgs-b, fortran routines

for large scale bound constrained optimization. *ACM Transactions on Mathematical Software.*, 23:550–560, 1997.

List of Figures

1.1 Example of service j transmitted from the transceiver to the receiver, traversing one optical multiplex section (OMS) i, and service $j+1$ propagating across OMS i and OMS $i+1$, passing through multiple optical amplifiers, fiber spans, and reconfigurable WSSes. 5
1.2 Proposed DT framework. 7
1.3 Hardware-based monitoring techniques. 21
1.4 AI-Light SDN framework. 27
1.5 Topology of DCI networks. 28

2.1 Flowchart of the experiment. 41
2.2 (a) Topology of the experimental mesh network; (b) AI-Light SDN framework. 42
2.3 (a) Number of services transported by each OMS after loading each batch; (b) Full-load normalized power spectrum at the output of the first EDFA of OMS1 with the "set and forget" operation mode, static strategy, and dynamic strategy. 44
2.4 Experimental testbed with details about service loading by ASE source, SNR measurement by transponder, and output power monitoring by OPM (OSA is for results analysis). 45
2.5 (a) Output power spectrum at the booster amplifier of OMS1 after loading batch 2/4/6; (b) Power decrease at the booster amplifier on each OMS of previously existing channels (batch N) due to loading new batch of services (batch $N+1$); (c) SNR decrease of existing services (batch N) due to loading new services (batch $N+1$). 48
2.6 (a) SNR variation of Service #1 with different number of established services; (b) Gain of Service #1 at each traversed EDFA; (c) Power of Service #1 after each traversed EDFA. 50
2.7 (a) SNR of services with power re-optimization strategies vs. "set and forget"; (b) PDF of SNR margins; (c) PDF of SNR gain per length (1, 2, 3 OMS) and per power re-optimization strategy. 53

2.8 Predicted SNR margin vs. measured SNR margin with (a) static strategy; (b) dynamic strategy. 56

3.1 Generic N-span OMS C+L system. 60
3.2 (a) OSNR, (b) Nonlinear SNR, (c) GSNR estimation in scenario 1 (3-span single OMS). 62
3.3 (a) Lumped loss estimation in scenario 1 (3-span single OMS); (b) SNR estimation after 10 OMSes in scenario 2 (10 OMSes with 3 spans); (c) GSNR estimation with aging in scenario 3 (aging). 62

4.1 Generic N-span OMS topology in a) C and b) C+L networks. 71
4.2 DT-enabled QoT optimization Framework. 74
4.3 a) Histogram of number of spans per OMS, b) histogram of fiber lengths in the considered network, and c) amplitude (i.e., range width) and standard deviation of the gain ripple of each amplifier. 76
4.4 Insertion loss estimation in a C network. 77
4.5 GSNR margin improvement in a C network. 78
4.6 GSNR prediction in a C network. 79
4.7 (a) GSNR variation in a C network; (b) GSNR variation prediction error in a C network. 81
4.8 Insertion loss estimation in a C+L network. 83
4.9 Insertion loss estimation in a C+L network. 84
4.10 Insertion loss estimation in a C+L network. 85
4.11 (a) GSNR variation in a C+L network; (b) GSNR variation prediction error in a C+L network. 86
4.12 Insertion loss estimation error with (a) channel power uncertainty, and (b) fiber attenuation coefficient uncertainty. 88
4.13 Tandem network testbed with 80 point-to-point services crossing 4 heterogeneous OMSs. 89
4.14 Insertion loss estimation (red dashed circle: anomaly detection and localization). 90
4.15 SNR estimation accuracy. 91
4.16 SNR optimization with predicted SNR and monitored SNR. 92
4.17 Monitored and predicted varied SNR after gain change of each amplifier pair during AIR process. 93

5.1 (a) Topology of OMS-based optical network and its parameters; (b) Transponder back-to-back limit; (c) Three-step IIR method. 103

5.2 (a) 5-OMS ring-topology network; (b) Average booster power variation across snapshots; (c) Histogram of total uncertain insertion loss across all spans; (d) Data usage assumption for simulation validation. 108
5.3 (a) Per-span insertion loss estimation accuracy; (b) Correlation between insertion loss estimation accuracy and power variation. 110
5.4 (a) SNR estimation with IIR; (b) SNR prediction with IIR. 111
5.5 Optimized network margin (top) and one-shot optimized SNR (bottom). . 112
5.6 (a) 5-OMS mesh network; (b) Average booster power variation; (c) Histogram of total uncertain insertion losses. 113
5.7 Flow chart of the IIR-enabled closed-loop multi-step power optimization. . 115
5.8 (a) Per-span insertion loss estimation accuracy; (b) Average absolute error of OMS-level insertion loss estimation; (c) Correlation between OMS-level insertion loss estimation accuracy and power variation. 116
5.9 (a) SNR estimation with IIR; (b) SNR prediction with IIR; (c) SNR prediction accuracy with/without IIR step 3 at Snapshot #15. 118
5.10 Optimized network margin enabled by IIR-refined/GT parameters (top), and optimized SNR at snapshot #15 (bottom). 120

6.1 5-OMS mesh network testbed. 126
6.2 PPE performance with different spatial resolutions. 127
6.3 Power profile estimation by PPE and by IR+PPE; plain markers are the estimated LPs. 127
6.4 (a) Insertion losses estimation; (b) QoT estimation; (c) QoT optimization. 128

7.1 1-span short-reach DCI network. 133
7.2 (a) NF look up table; (b) GSNR modelling validation. 134
7.3 (a) PDF of booster amplifier gain/NF variation; (b) Network margin variation (ZR); (c) Total capacity variation (ZR). 135
7.4 Capacity analysis. 137

List of Tables

1.1 Input parameter refinement techniques. 25

2.1 Required parameters for power re-optimization. 40
2.2 Routing table. 43
2.3 OMS per span information and corresponding P_{LOGO}. 43

4.1 Input parameters refinement techniques. 68

5.1 Input parameter refinement techniques. 100
5.2 OMS info. 106
5.3 Routing table. 107
5.4 OMS info. 114
5.5 Routing table. 114

6.1 Input and output parameters of IR and PPE. 124

Acknowledgements

I have been a PhD student at Politecnico di Milano for three years, while also doing periodic internships at the Huawei Paris Research Center. These three years spent between Milan and Paris have been among the most memorable of my life.

I want to thank Prof. Massimo Tornatore, my PhD advisor, for his constant support and guidance. The round-table meetings he organized in the lab gave me the chance to learn so much from other excellent researchers. He taught me how to write annual reports, conference papers, and journal articles with his amazing writing skills, and I also learned from his great presentation style. He supported me in contacting my defense committee and was always there for me during yearly evaluations and all kinds of administrative processes.

I am especially grateful to Dr. Yvan Pointurier, my supervisor at Huawei Paris Research Center, who has been supporting me since the very beginning of my research career—starting with my first internship with him in 2021, even before my PhD. He was always there to help me, whether with academic issues or with complicated tasks like internship and PhD contracts that required endless back-and-forth. From him, I learned how to manage projects and turn ideas into academic and industrial results, from proposal all the way to publication. Many of my ideas and inspirations came from our discussions. I also improved my spoken English (sometimes with a French accent) thanks to his excellent english skills.

I would like to thank Dr. Gabriel Charlet, director of the optical lab at Huawei Paris Research Center, for the many inspiring discussions we had. His knowledge and experience gave me a broader view of optical communications. And beyond work, I even learned to enjoy playing frisbee thanks to his great skills.

I am very thankful to Dr. Nathalie Morette for guiding me at the very beginning of my research path, introducing me to input refinement techniques, and showing me how to use the QoT estimator developed by Dr. Ivan Fernandez de Jauregui Ruiz and Dr. Salma Escobar-Landero. This tool became central to my PhD. I would also like to thank Dr. Alessio Ferrari, whose strong expertise in physical-layer topics helped me a lot at the start

of my journey.

I want to thank my colleagues at Polimi for the good times we shared in the PhD office, our discussions, our lunches (especially pizza), and our countless coffee breaks.

I am also grateful to my colleagues at the Huawei Paris Research Center optical lab for their help with experiments.

In particular, I want to thank my close friends Tarek Eldahrawy, Flávio Sampaio, Salma Escobar-Landero, Abel Lorences-Riesgo, Venkata Virajit Garbhapu, Chenyu Sun, Reda Ayassi, Trung-Hien Nguyen, Shuqi Yu and Abir Hraghi. Our ping-pong matches and lunches together in Paris are among my happiest memories.

My deepest gratitude goes to my wife, Lu Liu, and our two dogs, Guaishou and Boniu, for their unconditional love, companionship, and support throughout this whole journey. I also thank my parents and grandparents for always standing by me and supporting me in every step of my life.

Finally, I am grateful to everyone I have met along the way—each of you has, in your own way, contributed to the person I am today.